Overflows and Upper Ocean Interaction: A mechanism for the Azores Current

by

Shinichiro Kida

B.S. The University of Tokyo, 2000
M.S. MIT/WHOI Joint Program, 2003

Submitted in partial fulfillment of the requirements for the degree of

Doctor of Philosophy

at the

MASSACHUSETTS INSTITUTE OF TECHNOLOGY

and the

WOODS HOLE OCEANOGRAPHIC INSTITUTION

September 2006

Author .....
Joint Program in Oceanography/Applied Ocean Science and Engineering
Massachusetts Institute of Technology
and Woods Hole Oceanographic Institution
September 2006

Certified by .....
Jiayan Yang
Associate Scientist
Thesis Supervisor

Certified by .....
James F. Price
Senior Scientist
Thesis Supervisor

Accepted by .....
Joe Pedlosky
Chair, Joint Committee for Physical Oceanography
Massachusetts Institute of Technology/
Woods Hole Oceanographic Institution

Overflows and Upper Ocean Interaction:

A mechanism for the Azores Current

by

Shinichiro Kida

Submitted to the Massachusetts Institute of Technology
and the Woods Hole Oceanographic Institution
in partial fulfillment of the requirements for the degree of
Doctor of Philosophy

Abstract

The oceanic response to overflows is explored using a two-layer isopycnal model. Overflows are a major source of the dense water of the global deep ocean, originating from only a few marginal seas. They enter the open ocean as dense gravity currents down a continental slope and play a crucial role in the deep ocean circulation. To understand the dynamics of these overflows, previous studies simplified their dynamics by treating the overlying ocean as inactive. This simplification may be a first approximation for the overflow but not for the overlying ocean. The Mediterranean overflow, for example, entrains about 2 Sv of overlying Atlantic water when it enters the Atlantic through Gibraltar Strait. The upper ocean must balance the mass loss and vortex stretching associated with entrainment. Thus for the upper ocean, overflows represent a localized region of intense mass and PV forcing.

The simulations in this study show that in the upper layer, entrainment forces a cyclonic circulation along bathymetric contours. This is a topographic β-plume and its transport depends on the entrainment region size and the topographic slope. Baroclinic instability also develops and creates eddy thickness flux to the in-shore direction, forcing a double gyre topographic β-plume near the strait due to eddy PV flux convergence on the in-shore side of the continental slope and divergence on the off-shore side. When the upper oceanic response to overflows is examined specifically for the Mediterranean overflow, the upper ocean is found to establish two trans-Atlantic zonal jets, analogous to the Azores current and the Azores Counter current. These two zonal jets are an extension of the topographic β-plume driven by the overflow. Because the eddies in the steep slope region near Cape St. Vincent drive a mean flow across the slope, the topographic β-plume connects to the Atlantic Ocean to become a basin scale flow.

This thesis shows that overflows can induce a significant circulation in the upper ocean, and for the Mediterranean overflow, this circulation is a basin scale flow.

Thesis Supervisor: Jiayan Yang
Title: Associate Scientist

Thesis Supervisor: James F. Price
Title: Senior Scientist

Acknowledgments

I would first like to thank my co-advisers Jiayan Yang and Jim Price. Having Jiayan and Jim as my advisers was the best thing that happened to me in the program. I cannot thank them enough for their support and guidance. Coming straight from undergraduate school, there were many adjustments and new things to learn, and they taught me all of these things. Being a very slow learner who uses ten times more time to let things sink in, it must have been extremely frustrating for them to see me go through the process. I appreciate their endless patience, and their approach to science has been a great influence on me.

I would also like to thank my committee members, Karl Helfrich, Amy Bower, Sonya Legg and Raf Ferrari. Karl is always straight about teaching me where I'm wrong and guided me to where I might have answers. It was also Karl who taught me about β-plumes in his Ocean Circulation course, which turned out to be the central concept used throughout this thesis. Sonya's thorough approach to problems made me polish many aspects of my results and she also introduced me to a whole field of scientists by encouraging me to attend a workshop on deep-ocean overflows. Amy always brought me back to observations, the real ocean. Without her advice, I fear I might have drifted away from the actual ocean into the numerical ocean, which should always be avoided. Raf gave me insights to the eddy dynamics. His instant understanding of the problem and his continuous questions and interests made me learn a great deal. I would also like to thank Jack Whitehead, who kindly accepted to chair my defense, Bob Hallberg at GFDL for helping me use his model, John Marshall for guiding me when I first came to MIT, and the Education office for their extensive support.

I was very fortunate to have great colleagues: Tom Farrar, Jason Hyatt, and Mitch Ohiwa. Discussing homeworks, research, etc. together taught me variety of approaches to things. The presence of Fabio Dallan and Valerio Lucharini, the Italian duo, always lightened up the classroom and I enjoyed being invited for dinner. Jake Gebbie was always there for senior student's advice and helped me get out of

holes many times. I have had many officemates, Juli Atherton, Juan Botella, Max Nikourashin, David Stuebe, Claude Abiven, and Jessica Benthuysen at MIT and Greg Gerbi at WHOI. They all saw my ups and downs and I enjoyed their presence in the office during the weekend and late at night. Taka Ito and Masa Sugiyama, my two Japanese friends in the department, were always there for beer.

Last, I would like to thank my family, Hideji, Yasuko, and Ryoko Kida for their love and support from Japan.

This work was supported by the National Science Foundation Grant OCE-0424741.

Contents

Chapter 1

Introduction

1.1 Marginal sea overflows and the global ocean

The majority of the global deep ocean is filled with dense water that originates from only a few marginal seas around the world (Warren, 1981). Since these marginal seas are separated topographically from the open ocean by sills and straits, they are a convenient place to form and trap a pool of dense water (Bryden and Stommel, 1984). A portion of this dense water is known to spill over the sill from the marginal sea into the open sea through narrow straits as gravity currents called 'overflows' and they are the main pathway for the dense water formed in the marginal seas to reach the global ocean (Figure 1-1). A cross section of temperature, salinity and density shows the large contribution of the overflows in the Atlantic Ocean (Figure 1-2 a, b and c). The Denmark Strait and the Faroe Bank Channel overflows are known to contribute significantly to the mode water known as the North Atlantic Deep Water (NADW). The Mediterranean overflow and the Filchner Bank overflow contribute to the intermediate and bottom mode waters in the Atlantic known as the Salt tongue and the Antarctic Bottom Water (AABW) respectively.

The importance of overflows in determining the deep ocean properties has been acknowledged for some time and this has motivated efforts to understand their dynamics (e.g. Whitehead 1974; Candela 2001). But overflows also affect their overlying oceanic layer. The Mediterranean overflow, for example, is known to entrain about

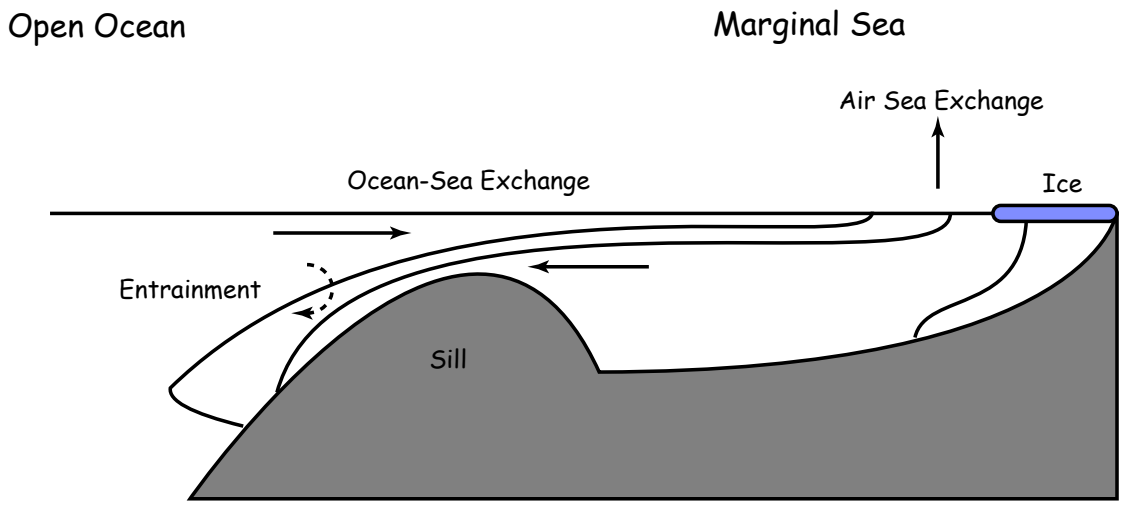

Figure 1-1: A schematic of the overflow and dense water formation in the marginal sea. Dense water is formed in the marginal sea due to either air sea exchange (heat loss, E-P) or ice formation. Most of the dense water is blocked topographically from flowing into the open ocean by a sill but a portion of it spills over the sill as an overflow. The overflow will then flow down the slope as it entrains the ambient water mass until it reaches its neutral buoyancy level or the bottom. There is a return flux from the open ocean to the marginal sea that has roughly the same amount of transport as the overflow at the sill to balance mass (Bryden et al., 1994). Figure adapted from Price and Baringer (1994).

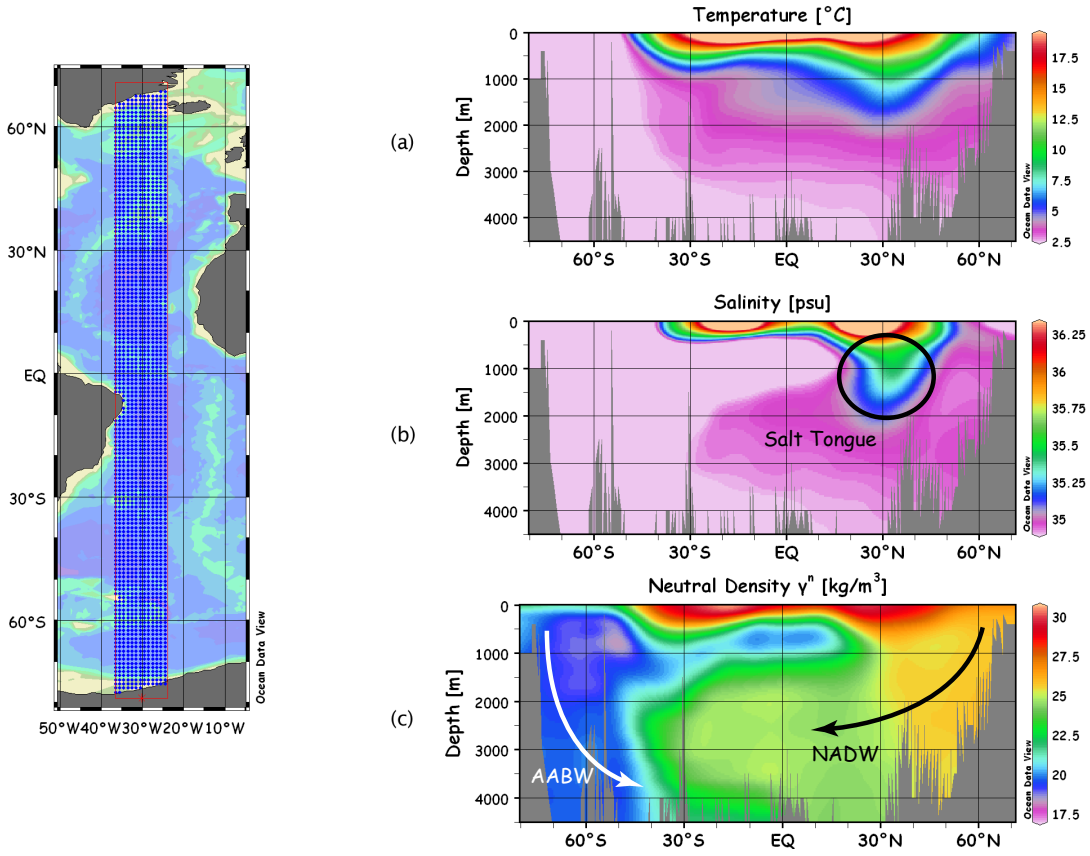

Figure 1-2: A cross section of the Atlantic Ocean between 35-25^{o}W showing the NADW, the AABW and the Mediterranean Salt tongue from WOCE database (WOCE Global Dataset Version 3.0) using Ocean Data View (Schlitzer, 2006). The Denmark Strait overflow and the Faroe Bank Channel overflow contribute to the deeper portion of the NADW (the Labrador Sea-formed dense water occupies the upper portion of the NADW) (Schmitz, 1996). The Filchner Bank and Ross Sea overflow contributes to the AABW (Orsi et al., 2000). The Mediterranean overflow is thought to contribute to the Salt Tongue in the mid-depth near 40^{o}N through Meddies (Richardson et al., 2000).

2 Sv of overlying Atlantic water while descending the continental slope (Price et al., 1993). So the upper oceanic layer must balance the mass loss forced by entrainment. This aspect of overflow-upper ocean interaction has not been investigated much in the past.

1.2 Motivations and questions

The dynamics of overflows are complex, involving scales from tens of kilometers to a few meters, which makes theoretical, observational, and numerical examination difficult. But since the properties (density, temperature, salinity) of product water of the overflows play an important role in setting the deep ocean properties, studies of overflows have been primarily focused on understanding the marginal sea - deep ocean pathway and density modification process (Ambar and Howe, 1979a). Process models have often assumed the ambient ocean as an inactive background field to simplify the problem (Smith, 1975). This assumption has been used successfully to gain an understanding of overflows such as off-shore descent by bottom friction and localization of entrainment at shelf breaks (Baringer and Price, 1997). These process studies indicated high sensitivity of the product water on the density of the ambient ocean (Price and Baringer, 1994).

While the assumption of an inactive upper layer led to many advances in the understandings of overflow dynamics, the assumption may not have been valid especially with regards to the upper ocean water. Recent work by Jia (2000) suggested that the overflow may have a basin scale influence on the upper ocean. Using a Global Circulation Model(GCM), the formation of the Azores Current was shown to depend on whether or not the GCM includes the Mediterranean overflow. The Azores Current is a zonal flow of 7–13 Sv (Stramma, 1984; Klein and Siedler, 1989; Alves and Colin De Verdiere, 1999) in the upper ocean between 32–35^{o}N that branches from the Gulf Stream and flows across the Atlantic Ocean reaching as far as the Gulf of Cadiz (Figure 1-3). A narrow and strong eastward current, analogous to the Azores Current, formed in the GCM when the Mediterranean overflow was included but only a broad

and weak eastward current formed when the overflow was not included. The dynamical reason for this sensitivity of the eastward zonal jet to the Mediterranean overflow was not clear in Jia's study but nonetheless the study illustrated the potential impact that the overflow has on the large scale upper ocean circulation.

Other studies on the interaction between the overflow and its overlying ocean progressed mostly through laboratory and numerical experiments and these studies focused on the interaction on the scale of the continental slope. Laboratory experiments showed that dense plumes down a slope induce a strong upper layer motion adjacent to the plumes which in turn influences the propagation speed of the dense plume (Whitehead et al., 1990; Etling et al., 2000). In a three dimensional primitive equation model, baroclinic instability was found to occur (Jiang and Garwood, 1996) and in some cases a strong barotropic cyclone formed (Spall and Price, 1998).

Past studies indicate a strong interaction between the overflow and the overlying ocean. Yet, we do not fully know how the two layer interaction affects the upper-layer in the time average sense and what the spatial scale of influence is. Although the results of Jia (2000) suggest a basin scale influence of overflows on the upper ocean, the Mediterranean overflow was merely a restoring boundary condition of density in her calculation. The resolution was too low to include any detailed overflow dynamics so important dynamical processes may have been poorly represented. Whether or not the overflow can induce a large scale circulation in the overlying ocean is still an open question.

How does the upper ocean respond to the overflow below and vice versa? This is the main question investigated in this thesis. There are two ways of answering this question. The first way is to determine whether the overflow-upper ocean interaction can significantly influence the two layers in the continental slope region, which is a view focusing the interaction on a regional scale. The second way is to determine whether the overflow-upper ocean interaction can influence the basin scale provided that the overflow-upper ocean interaction is significant in the slope region. These two different views will be investigated separately in this thesis.

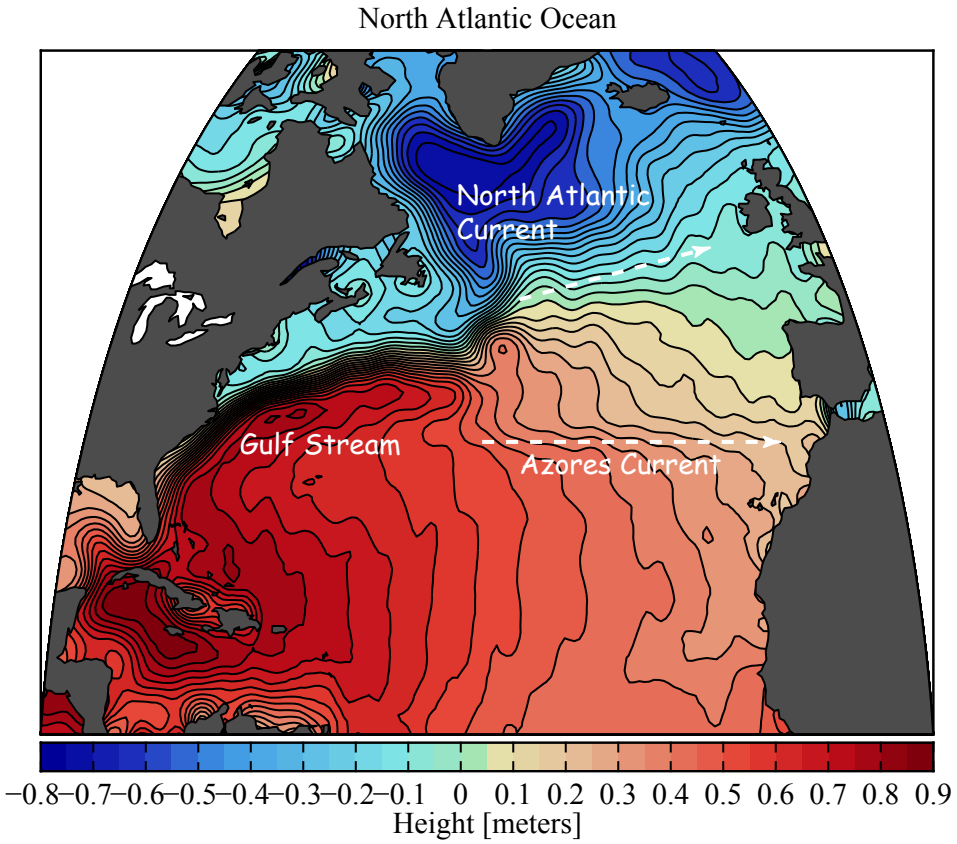

Figure 1-3: Sea surface height of the North Atlantic Ocean obtained from Satellite Altimetry (Jayne, 2006). The figure shows the subtropical and sub-polar gyre of the Atlantic Ocean. The region where contours are confined are where strong horizontal flows exist which highlights the Gulf Stream, the western boundary current of the subtropical gyre. The figure also shows the Gulf stream bifurcating at the tail of the Grand Banks into the North Atlantic Current (NAC) and the Azores Current. The NAC flows into the Nordic Seas and also becomes part of the sub-polar gyre. The Azores Current flows zonally across the Atlantic as a zonal jet. Figure reproduced by courtesy of Dr. Steve Jayne.

1.3 The hypothesis

A large scale circulation, known as a β-plume, can be induced by a small scale forcing. Our hypothesis is that the upper ocean, on both the continental slope and basin scales, is influenced by the overflow through the β-plume mechanism which, for the Mediterranean overflow, leads to the formation of the Azores Current.

The dynamical concept of β-plumes was introduced by Stommel as a mechanism of deep ocean circulation driven by hydrothermal plumes (Stommel, 1982). The way a β-plume forms in the ocean can be shown from the linear vorticity equation on a β-plane with a flat bottom:

$$\beta v = \frac{f_o w^*}{h} + A_H \nabla^2 \zeta, \tag{1.1}$$

where β, v, f_o, w^*, h, A_H and ζ are planetary vorticity gradient, meridional velocity, Coriolis parameter, diapycnal velocity, layer thickness, lateral viscosity coefficient and relative vorticity respectively. Imagine that a local mass sink exists in the interior of a rectangular basin on a β-plane (Figure 1-4). Assuming that friction is negligible in the interior, Eq 1.1 shows that in the Northern Hemisphere, a northward flow that crosses the planetary vorticity contours will balance the vortex stretching created by the mass sink ($w^* > 0$):

$$\beta v = \frac{f_o w^*}{h}. \tag{1.2}$$

In a steady state, this northward flow must be balanced by a southward flow somewhere on the same latitude to conserve mass. According to the linear vorticity equation, a meridional flow can not form in the interior where friction is considered negligible and diapycnal mass flux does not exist. So this southward flow must take place in the viscous western boundary layer where friction can support a meridional flow:

$$\beta v = A_H \nabla^2 \zeta. \tag{1.3}$$

Connecting the two meridional flows are two zonal jets along the background planetary vorticity contours that close the cyclonic circulation (Figure 1-4). This horizontal

circulation, called a 'β-plume', is a circulation caused by the presence of planetary vorticity gradient β.

There are at least two things that characterize this planetary β-plume.

First, a planetary β-plume is a basin scale circulation. Assuming that the vertical diffusion is weak in the interior, a small region of mass sink/source in the interior of the open ocean can drive two strong zonal flows that extend west to the western boundary layer.

Second, a planetary β-plume has much larger transport than the mass sink/source Spall (2000). The ratio of the diapycnal mass flux to horizontal circulation is

$$\frac{V}{W} = \frac{vhL_x}{w^* L_x L_y}, \tag{1.4}$$

where V and W are the total horizontal (along isopycnal) and diapycnal transport, L_x and L_y are the length of the mass sink zonally and meridionally. By substituting Eq 1.2 for v,

$$\begin{aligned} \frac{V}{W} &= \frac{\frac{f_o w^*}{\beta h} h}{w^* L_y} \\ \therefore \frac{V}{W} &= \frac{f_o}{\beta L_y}. \end{aligned} \tag{1.5}$$

Reasonable parameter values are $f_o = 1 \times 10^{-4}$ s^{-1}, $\beta = 2 \times 10^{-11}$ m^{-1}s^{-1}, and L_y =50 km for entrainment by overflows which then estimates $\frac{V}{W}$ as 100. So 2 Sv of entrainment will establish a β-plume with a transport of 200 Sv, a transport that is two orders of magnitude larger than the forcing.

Eq 1.5 shows that the transport of the β-plume depends on the PV difference between the two zonal jets, βL_y. The reason why the β-plume transport depends on βL_y can by described by examining the PV balance in the forcing region (Figure 1-5). The mass sink region corresponds to a region of PV increase (PV forcing) so in a steady state, this PV increase in the interior of a basin must be balanced by a PV divergent flow. This is what the two zonal jets do. Depending on βL_y, the PV difference due to the latitudinal location of the two jets, the two jets will change

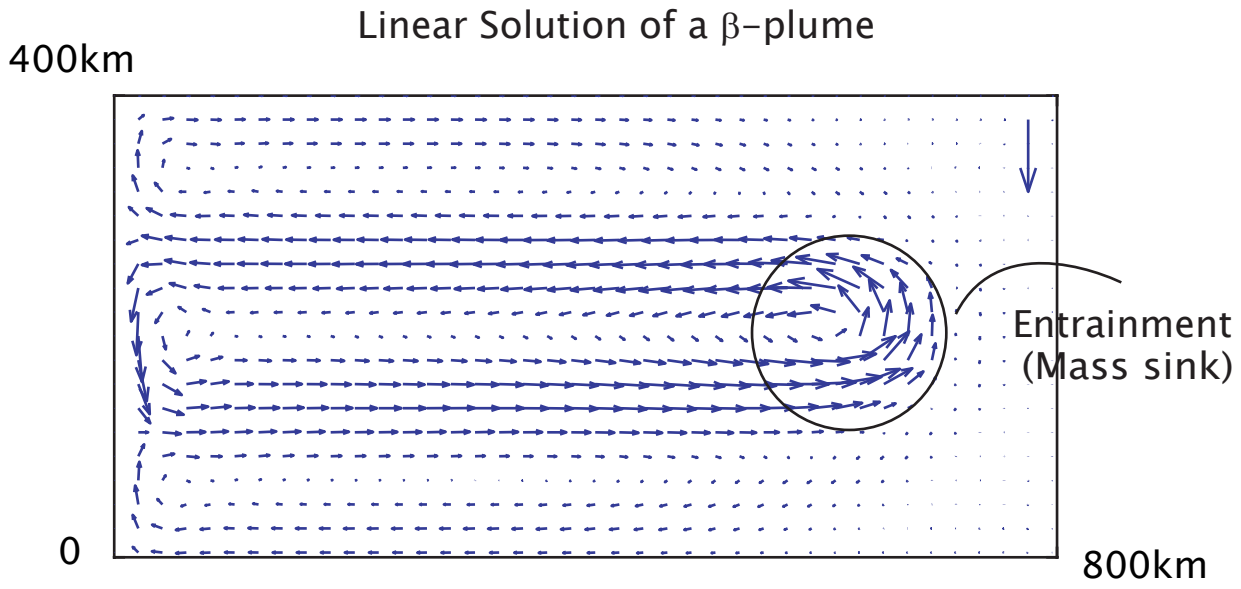

Figure 1-4: Velocity field of a β-plume using a linear one-layer reduced gravity model. The domain is 800 km (zonally) $\times$ 400 km (meridionally) and is on a β-plane. A localized mass sink is located in the middle of a basin. This mass sink drives a northward flow which is balanced by a southward flow in the western boundary layer with two zonal jets connecting the two meridional flows. This circulation is called a β-plume. A weak mass source is distributed uniformly across the basin to balance mass in the model and this mass source forced a weak northward flow in the western boundary layer and the weak southward flow in the interior, noticeable in the background of the topographic β-plume driven by the mass sink.

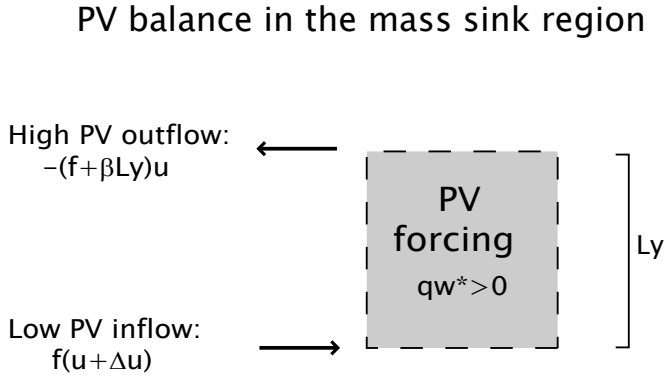

Figure 1-5: A schematic of the PV balance in the entrainment region. The entrainment region in the interior of a basin corresponds to a region of PV increase (PV forcing). The two zonal jets located on different latitudes will balance this PV increase by creating a PV divergence flow using their background PV difference βL_y. If βL_y decreases, the jets will balance the PV increase by a flow with smaller velocities. If βL_y increases, the jets will balance the PV increase by a flow with larger velocities.

their transports so that its PV divergence will balance the PV increase created by the mass sink. If the background PV gradient decreases, βL_y will decrease so the two jets are required to increase the magnitude of their transports to maintain the same PV divergence. Conversely, if the background PV gradient decreases, βL_y will increase so the two jets are required to decrease the magnitude of their transports to maintain the same strength of PV divergence.

The Azores Current as a branch of the β-plume

The Mediterranean overflow entrains about 2 Sv of upper oceanic mass (Ambar and Howe, 1979b) so the β-plume transport in the upper layer is estimated to be about 200 Sv, according to Eq 1.5. This estimate is too large compared to 7–13 Sv, which is what is observed for the Azores Current (Alves and Colin De Verdiere, 1999). Therefore the hypothesis of the Azores Current as an eastward branch of a β-plume seems implausible. However, this is an estimate of the β-plume based on the planetary β-plane. If PV forcing exists in a region where a topographic slope influences the dynamics, the topographic β would be the relevant background PV gradient not the

planetary β. For example, if we assume entrainment occurs in a region about 50 km in length-scale ($=L_x, L_y$), slope of 0.01, and a basic layer thickness of 1000 m, topographic β would be 1×10^{-9} m^{-1}s^{-1} and substituting this value for the planetary β in Eq 1.5, the estimate of the topographic β-plume transport will be about 4 Sv for the eastward branch and 2 Sv for the westward branch. These transport estimates are smaller but on the order of what is observed for the transport of the Azores Current (7–13 Sv) and also for the Azores Countercurrent (about 2 Sv), which is an westward zonal flow observed to the north of the Azores Current (Alves and Colin De Verdiere, 1999). The presence of steep topography can dramatically increase the magnitude of the background PV gradient and thus decrease the strength of the β-plume (Figure 1-6). Then the hypothesis that the Azores Current is a branch of the topographic β-plume driven by the Mediterranean overflow becomes reasonable from scaling.

We have described our hypothesis that overflow-upper ocean interaction may result in a β-plume formation in the upper layer. But what is known about the overflows and their regional circulation from observations? This aspect will be described next.

1.4 What do we know now?

Past studies on the Faroe Bank Channel and Mediterranean overflows are described in this section. These two overflows were chosen because they are well-observed (Price et al., 1993; Mauritzen et al., 2005). The Mediterranean overflow is known to be fairly steady and its mass balance between the marginal sea and the open ocean is well-defined. We are also interested in investigating whether the Mediterranean overflow is capable of driving the Azores Current. Other major overflows are either data scarce (Filchner Bank overflow) or likely overwhelmed by the vigorous western boundary current (Denmark Strait) such that the overflow-upper ocean interaction is hard to observe. Past studies on the Azores Current are also described in this section along with the hypotheses for its driving mechanism other than that described above.

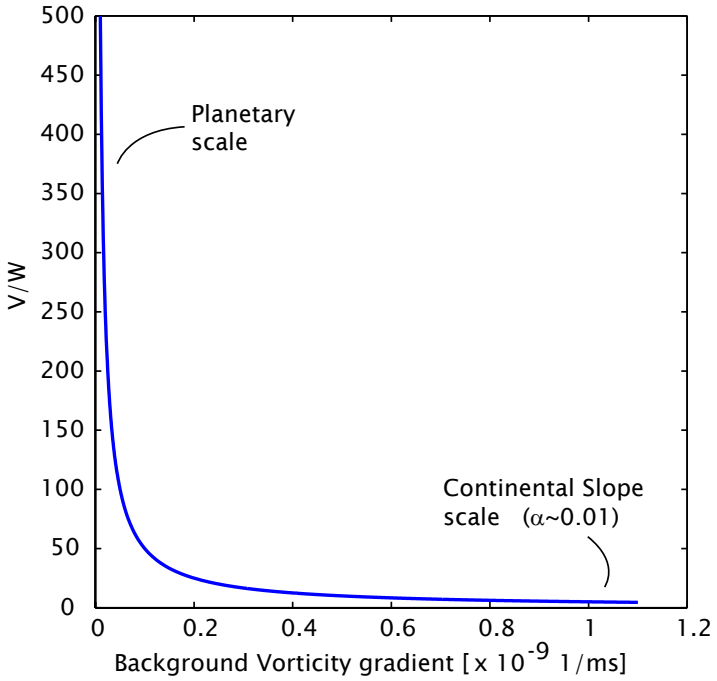

Figure 1-6: The transport of the β-plume as a function of the background vorticity gradient using Equation 1.5. The transport of the β-plume is scaled by the entrainment assuming that entrainment occurs with a length-scale of L_y =50 km. The planetary β is about 2×10^{-11} $\mathrm{m}^{-1}\mathrm{s}^{-1}$ so V/W is large (left side). The topographic β is about 1×10^{-9} $\mathrm{m}^{-1}\mathrm{s}^{-1}$ in the continental slope region so V/W is of order one (right side). Because of the significant difference in the background vorticity gradient between the two cases, the difference in the transport of the β-plume is also significant.

1.4.1 The Faroe Bank Channel overflow

The Faroe Bank Channel overflow is one of the prime sources for the NADW and occupies the deeper portion of this water mass (referred to as lower or eastern NADW). Its cold and salty character originates from the dense water formation occurring in the Nordic Sea and resembles that of the Denmark Strait overflow since both overflows have the same Nordic Sea origin (Schmitz, 1996).

The Faroe Bank Channel, where the Faroe Bank Channel overflow enters the Atlantic, is located at the eastern end of the Greenland-Iceland-Scotland Ridge that separates the Nordic Sea from the Atlantic Ocean (Figure 1-7a). Denmark Strait is located at the western end of this ridge. The Faroe Bank Channel is about 800 m deep and 20 km wide at the sill (Figure 1-7b) and the transport of the Faroe Bank Channel overflow is about 1.5–2.0Sv with typical properties of (T,S)=(0^oC, 34.9) at the channel (Mauritzen et al., 2005). After entrainment of the Atlantic water, the transport increases to 2.5–3.0 Sv with the properties modified to (T,S)=(3^oC, 35.0), indicating that the overflow entrains about 0.5–1.5Sv Sv of North Atlantic water.

The temperature of the Faroe Bank Channel overflow was observed to fluctuate with about a 3.5 day frequency at about 140km downstream from the sill. This fluctuation is likely the result of eddies of 20km radius passing by with a speed of 0.5m/s (Høyer and Quadfasel, 2001). These eddies have a thickness of roughly 150m and their center cores remain unmixed with the Atlantic water, retaining their properties relatively unmixed with the environment. They also have a substantial barotropic component (few centimeters of sea surface height) which are thought to be the cause for the high eddy kinetic energy in the region detected from satellite altimetry (Høyer et al., 2002).

The circulation in the upper layer

A cyclonic circulation exists at about 400–700 m depth in the Iceland Basin (Lavender et al., 2005) and this circulation may balance the 1.0–2.0 Sv of upper oceanic water that is entrained to the overflow. The forcing mechanism of this cyclonic circulation

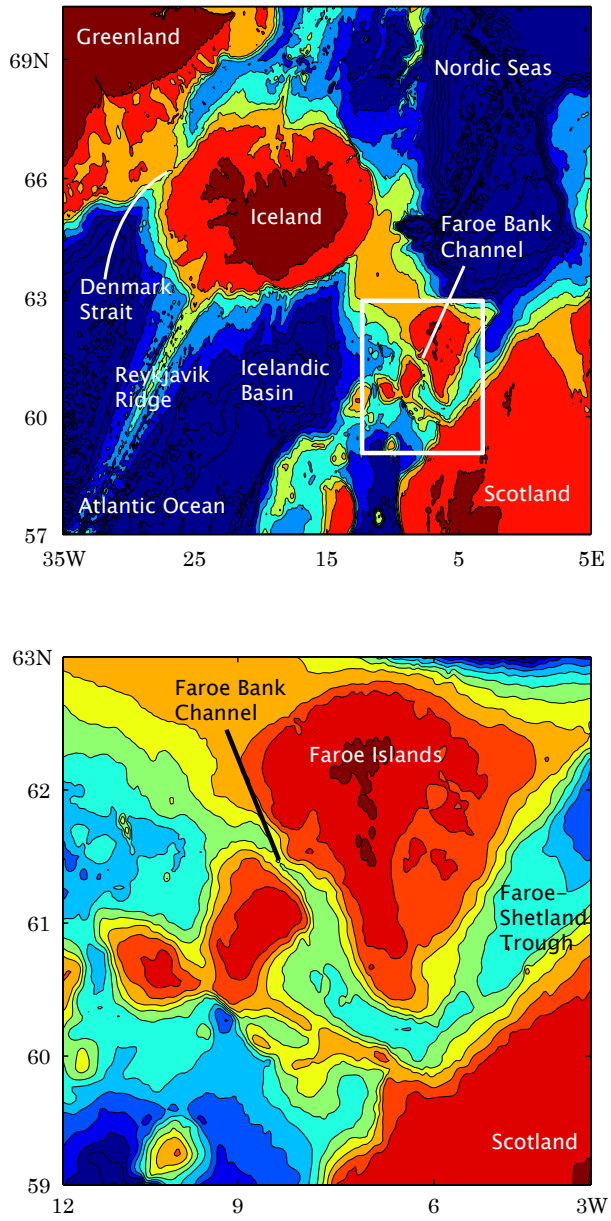

Figure 1-7: Map of Northern Atlantic (above) based on Smith and Sandwell's bottom bathymetry (Smith and Sandwell, 1997). The bathymetric contours are shown from 0 to 2000 m every 500 m. The Denmark Strait (west) and the Faroe Bank Channel (east) are the two deep straits known to connect the Nordic Seas and the North Atlantic. The Denmark Strait is located between Greenland and Iceland. The Faroe Bank Channel is located between Iceland and Scotland. Figure below shows a closer look of the region near the Faroe Bank Channel. The bathymetric contours are from 0 to 1000 m every 200 m. The upstream basin of the Faroe Bank Channel overflow is the Faroe-Shetland Trough and the overflow flows into the Atlantic through the Faroe Bank Channel which is about 800 m deep.

is unclear and may well be part of the rim current of the large scale sub-polar gyre. The Norwegian Atlantic Current (NwAC) is known to flow northeast in this part of the North Atlantic near the sea surface (Fratantoni, 2001; Orvik and Niiler, 2002). The NwAC originates from the North Atlantic Current (NAC) that is thought to transport the warm and salty Atlantic water into the Nordic Seas. However, the core of the NwAC exists far west (about 400–500 km) from the Faroe Bank Channel and it appears that this current is unrelated to the Faroe Bank Channel overflow. For the regions directly above the Faroe Bank Channel overflow, the time-mean circulation near the sea surface remains unclear.

1.4.2 The Mediterranean overflow

The Mediterranean overflow is the source of the Salt tongue in the Atlantic Ocean (Figure 1-2) and its high salinity character is a result of excess evaporation in the Mediterranean Sea (Candela, 2001). This character is unique compared to the other three major overflows of the Atlantic Ocean (Denmark Strait, Faroe Bank Channel, and Filchner Bank overflows) where dense water forms primarily due to thermal convection. Despite the fact that the source water of the Mediterranean overflow is extremely dense, its density is vigorously modified through entrainment of lighter Atlantic Ocean water as it descends the slope. It becomes neutrally buoyant at about 900m depth rather than reaching the sea floor (Ambar and Howe, 1979b). The resulting Mediterranean overflow water, however, keeps its high salinity anomaly and thus leaves a strong salinity signature along its flow path forming the salt-tongue near mid-depth (about 1000 m) of the Atlantic Ocean (Richardson et al., 2000).

The bottom bathymetry of the region near the Mediterranean overflow and the Gulf of Cadiz is shown in Figure 1-8 along with the location of topographic features referenced many times in this thesis. The transport of the overflow is about 1 Sv at the Strait of Gibraltar (Camarinal Sill) with typical temperature and salinity of 13.0^{o}C and 38.4 respectively (Figure 1-9) (Bryden and Kinder, 1991). Slightly more Atlantic water enters the Mediterranean Sea at the sill to balance the mass loss due to excess evaporation over the Mediterranean Sea. The transport of the overflow

increases to about 2–4 Sv by the time the outflow reaches Cape St. Vincent by entraining approximately 1–3 Sv of North Atlantic Central Water (NACW). This mass balance indicates that a total of 2–4 Sv must flow into the Gulf of Cadiz from the Atlantic Ocean to balance mass. However, how the upper oceanic layer brings this 2–4Sv of transport in to the Gulf of Cadiz is not well known.

The Mediterranean overflow entrains the upper Atlantic water well before it reaches Cape St. Vincent (Baringer and Price, 1997). Entrainment is localized and abrupt rather than gradual and diffusive. The mechanisms of this entrainment have been investigated mostly through a stream-tube model, which is a two dimensional, steady, and bulk property model useful for diagnosing the basic dynamical balance of the overflow as it flows down the continental slope (Smith, 1975). By incorporating a Kraus-Turner mixing parameterization into this stream-tube model, entrainment was found to occur vigorously at the shelf break where the Froude number becomes large enough for occurrence of Kelvin-Helmholtz instability (Price and Baringer, 1994). After the vigorous mixing near the shelf break, the density of the Mediterranean overflow becomes close to NACW such that Kelvin-Helmholtz instability will not likely to happen again, thus no entrainment. The majority of entrainment occurs roughly within 60km from where the overflow enters the Gulf of Cadiz, which is only 15% of the path between Gibraltar Strait and Cape St. Vincent.

The Mediterranean overflow was observed to fluctuate with a frequency of about 3 days near Portimão Canyon, about 150 km downstream from the sill. This time variability is uncorrelated with the time variability at the strait (Stanton, 1983) and is thought to be a result of baroclinic instability downstream of the strait (Chérubin et al., 2003). Eddies of both signs have been observed in the Mediterranean overflow (Serra and Ambar, 2002; Carton et al., 2002) which may have formed through baroclinic instability (Chérubin et al., 2000; Aiki and Yamagata, 2004). The canyons in the continental slope of the Gulf of Cadiz may also trigger the instability. Note that Meddies, known to advect the salty Mediterranean overflow water into the interior of the Atlantic, are mostly generated near Cape St. Vincent which is further downstream from the sill (Bower et al., 1997).

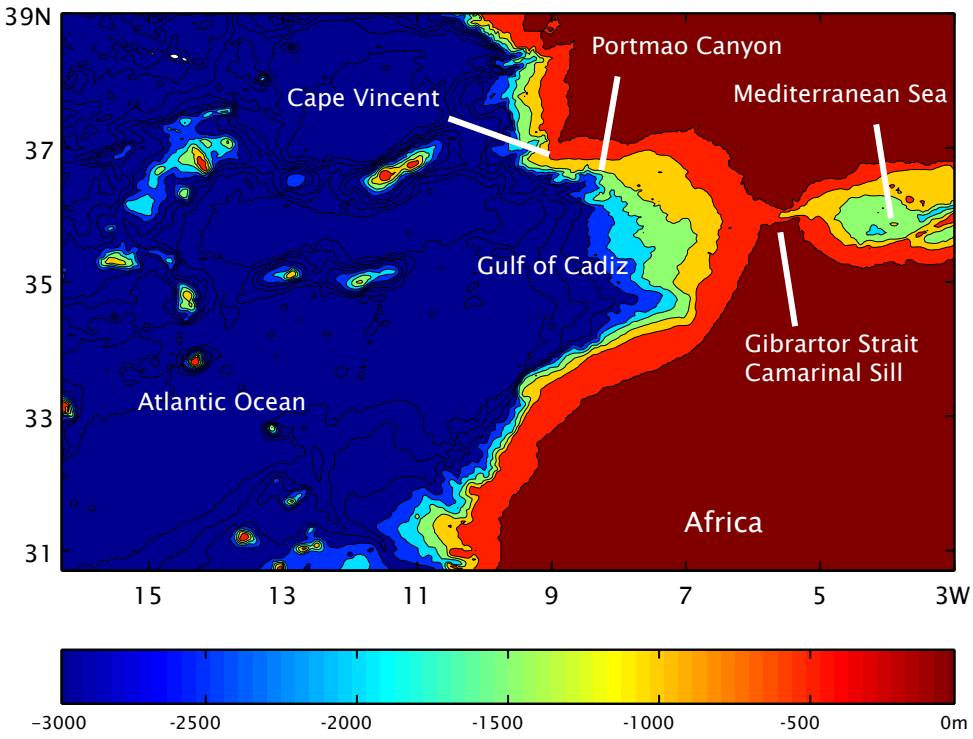

Figure 1-8: Map of the Mediterranean Sea, Gulf of Cadiz and Atlantic Ocean. The Mediterranean overflow enters the Atlantic from the Mediterranean Sea through Gibraltar Strait (Camarinal Sill), which is about 300 m deep. It flows along the continental slope of the northern side of the Gulf of Cadiz through Portimão Canyon reaches Cape St. Vincent. The overflow then turns north at Cape St. Vincent while also forming anticyclonic eddies known as Meddies. Meddies will travel westward into the interior of the Atlantic.

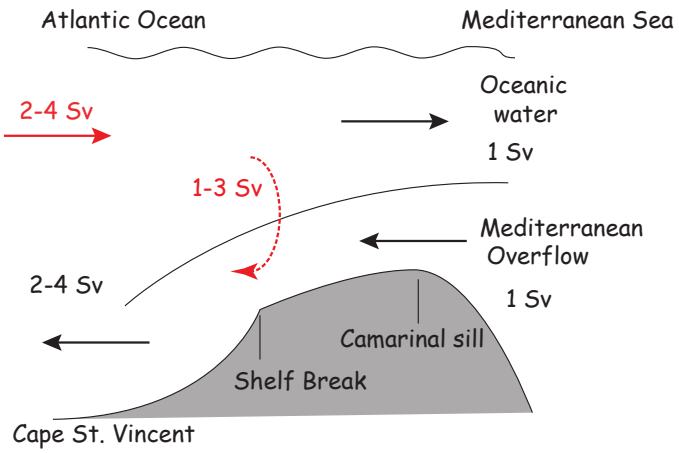

Figure 1-9: A schematic of the mass balance of the Mediterranean overflow(right) and the Atlantic Ocean(left). Camarinal sill separates the two regions. Overflows spills into the open ocean from the marginal sea with a transport of 1 Sv at the Camarinal sill. An equivalent amount of mass returns to the marginal sea in the upper layer. The overflow transport increases to 2–4 Sv by Cape St. Vincent. This increase of overflow water indicates entrainment of 1–3 Sv which is know to occur near the shelf break. The mass balance, therefore, indicates that the upper layer must flux 2–4 Sv into Gulf of Cadiz. Black arrows indicate directly observed estimates whereas red arrows indicate indirect estimates.

The circulation in the Gulf of Cadiz

Observations of the upper ocean circulation in the Gulf of Cadiz are mostly limited to the northern half of the Gulf since most observations have focused on the Mediterranean overflow that exists on this side of the Gulf. Mauritzen et al. (2001) estimated from a hydrographic section that within the Gulf, a cyclonic recirculation is likely to exist above the Mediterranean overflow layer with 4.6 Sv of westward transport along the northern boundary and 7.7 Sv of eastward transport in the remaining southern half of the Gulf, supporting 3.1 Sv of mass lost to the Mediterranean overflow layer. The absolute velocity field along the northern boundary of Gulf of Cadiz taken in the Sortie des Eaux Mediterranean en Atlantique Nord-East (SEMANE) experiment was shown to be dominantly in the westward direction above the Mediterranean overflow between 100–180 m depth, in agreement with this cyclonic circulation. Ochoa and Bray (1991) also estimated that the total eastward transport across 8^o W is about 6–7 Sv in the upper oceanic layer, which is 3–5 Sv excess to what is required from

mass balance. These transport estimates are quasi-synoptic and the time average circulation remains unclear. None of the past observational studies have shown a clear picture of what the basic time average circulation looks like in the Gulf of Cadiz. However, the quasi-synoptic transport estimates do indicate that a recirculation gyre exists in the Gulf of Cadiz which brings more mass into the gulf than what is required by mass balance (about 2–4 Sv, Figure 1-9).

Observations of the Faroe Bank Channel overflow, the Mediterranean overflow, and the Gulf of Cadiz show time variability and eddy formations near the continental slope. These observations indicate a strong interaction between the overflow and the upper ocean at least on the regional scale.

1.4.3 The Azores Current

The Azores Current is a zonal current that crosses the eastern half of the North Atlantic between 32–35^{o}N (Figure 1-3). It bifurcates southward from the Gulf stream around 40^{o}W and then turns eastward near 35^{o}N reaching as far as the Gulf of Cadiz (Klein and Siedler, 1989; Lozier et al., 1995). The position of the current is also an area of high eddy kinetic energy (Traon and Mey, 1994). Between 20–35^{o}W, the Azores Current is about 150 km wide, 1000 m deep, has a transport of roughly 7–13 Sv (Alves and Colin De Verdiere, 1999) and has a surface speed over 10 cm/s (Figure 1-10b). The current has a stronger signal near the surface with eddies and meanders of 100 km and a phase speed of 5cm/s close to that of a planetary Rossby wave, which are thought to be a result of baroclinic instability (Kielmann and Käse, 1987). Near the eastern boundary of the Atlantic, the Azores Current bifurcates into a southward branch and an eastward branch. Paillet and Mercier (1997) estimated using an inverse model that the southward branch has about 6 Sv and joins the Canary current while the eastward branch has about 4 Sv and flows into the Gulf of Cadiz. The existence of a westward current, to the north of the Azores Current (about 38^{o}N) and termed the Azores Countercurrent, was suggested by Onken (1993). Alves and Colin De Verdiere (1999) estimated 2.0 Sv of annual mean transport for this current from National Oceanic Data Center hydrological data, which is less than

that of the Azores Current, and roughly ± 1 Sv of seasonal fluctuation.

The Azores Current is also know as the Azores Front, which is a sharp temperature front. The temperature and velocity fields from high-resolution data assimilation (Figure 1-10a) as well as direct observations (Rudnick and Luyten, 1996) show a sharp frontal structure associated with the Azores Current. This front plays an important role in the subduction process in the eastern North Atlantic and its subtropical gyre (New et al., 2001). However, the main forcing agent for the Azores Current is still unresolved and GCMs have often failed to reproduce this feature. Two hypotheses have been proposed (see Käse and Siedler 1996 for review). The first hypothesis is that the Azores Current is an inertial jet flowing along the line of zero wind-stress curl, which would be the boundary of the subtropical gyre and sub-polar gyre. However, this hypothesis is insufficient to explain the steady latitude positioning of the current ($\pm\ 2^o$) compared to the large seasonal change of the wind field ($\pm\ 10^o$). The wind stress as a driving mechanism of the Azores Current is therefore unlikely.

The second hypothesis proposed that the Azores Current is part of a planetary β-plume driven by the entrainment caused by the Mediterranean overflow (Özgökmen et al., 2001). The 1.5 layer reduced gravity model showed a formation of the Azores Current with 10 Sv and the Azores Countercurrent of 8 Sv. Although these transport estimates from the model were somewhat on the same scale as observations, the match may have been a consequence of the low resolution and high viscosity used in their model. As shown in the previous section, Eq 1.5 estimates the strength of the planetary β-plume (driven by entrainment by Mediterranean overflow) two orders of magnitude too large for it to be the main mechanism for driving the Azores Current. If a higher resolution were used, the model would likely create a vigorous Azores Current that has much larger transport than the low resolution model. The hypothesis that the Azores Current is a planetary β-plume is not plausible.

Past hypotheses appear insufficient to explain the observed features of Azores Current correctly. Our hypothesis that the Azores Current is a branch of the topographic β-plume seems plausible at least on matching the order of transport from the linear vorticity estimate, but whether such β-plume can actually establish in the

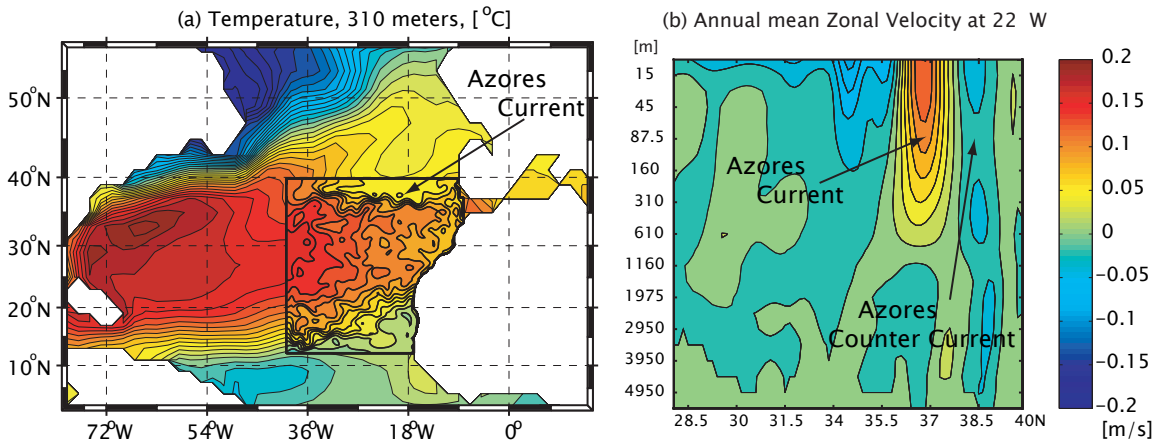

Figure 1-10: The Azores Current in the $1/6^o$ resolution ocean model produced from data assimilation (Gebbie, 2004). Figures reproduced by courtesy of Geoffrey Gebbie. **(a)** The temperature field at 400m depth contoured from 3 to 18^{o}C every 1^{o}C. The basic background flow show the subtropical gyre and a temperature front near 35–37^o N. This is where the Azores Current exists. **(b)** The zonal velocity at 22^o W. The Azores Current is the strong eastward (positive) flow near 35–37^o N. The rough estimate of the transport from this cross section is about 15 Sv, assuming the main core of the current is about 150 km wide and 1000 m deep with an average speed of 10 cm/s. The Azores Countercurrent is the westward (negative) flow near 39^o N. The rough estimate of the transport is about 5 Sv, assuming the main core of the current is about 100 km wide and 1000 m deep, with an average speed of 5 cm/s.

open ocean needs further investigation.

1.5 The goal and the outline of the thesis

The goal of this thesis is to understand how the dynamics of the overflow and its overlying ocean are coupled. Outstanding questions are

1. How does the upper ocean layer balance the mass loss caused by entrainment?
2. Do eddies created by baroclinic instability or other adiabatic layer interactions significantly affect the overflow and upper ocean dynamics?
3. Does the overflow have any basin scale impact on the upper ocean?

The first two questions are examined in Chapter 2 within the continental slope region. The approach is to do a process modeling study using a simple model (compared

to a GCM) and the Faroe Bank Channel and Mediterranean overflows were chosen as ideal places to examine these questions. We will be focusing on the overflow-upper ocean interaction from the Potential Vorticity (PV) balance point of view, based on the concept of a β-plume. The dynamics of a β-plume can be much richer with the presence of eddies and instabilities compared to a linear and steady β-plume (Figure 1-4).

The third question is examined in Chapter 3 by using process models with an open ocean region. We will test the hypothesis of the Azores Current as a branch of the topographic β-plume driven by the Mediterranean overflow and explain why this hypothesis is plausible.

Discussions and the conclusions drawn from investigating the three questions will be presented in Chapter 4.

Chapter 2

Overflow and upper ocean interaction on the continental slope

When an overflow descends the continental slope, it interacts with its overlying ocean through two mechanisms: entrainment and baroclinic instability. Entrainment is a diabatic process whereas baroclinic instability is an adiabatic process. Both processes happen abruptly and locally near the strait rather than gradually along the path of the overflow on the continental slope. However, a local interaction (forcing) does not necessarily mean that its dynamical influence is also trapped locally. As shown in the previous chapter, a local forcing is capable of inducing a circulation of larger scale than its own forcing size, known as a "β-plume " (Stommel, 1982). Can the overflow-upper ocean interaction result in such a circulation? We will first examine the effects of the overflow-upper ocean interaction on the scale of the continental slope before discussing its effect on the basin scale.

When a two-layer isopycnal model (details described below), representing the overflow and its upper layer with prescribed entrainment, was solved in the continental slope region, the upper layer was found to form a strong eddy field over most of the continental slope region (Figure 2-1a). The sea surface height shows eddies that were energetic and had a sea surface height of about $\pm$15 cm, radius of 50 km, and an azimuthal velocity as large as 40 cm s^{-1}. The overflow layer also formed a time-varying flow field with strong anticyclonic eddies flowing along the bathymetric

contours (Figure 2-1b). The experiment, hereafter Case 1, shows that the interaction between the overflow and the upper ocean is strong and results in complicated flow field in both layers.

In this chapter, we will investigate the dynamics of the highly time-varying flow field due to overflow-upper ocean interaction (Figure 2-1). The chapter is organized in four sections. First, the full model used for the study is described. Second, the diabatic and adiabatic overflow-upper ocean interaction are examined separately. Third, the full (diabatic and adiabatic) overflow-upper ocean interaction is examined. Last, the numerical results are compared to field observations.

2.1 The Model Setup

The numerical model used for examining the overflow-upper ocean interaction in the continental slope region is described in this section. The model is a two-layer isopycnal model with the two isopycnal layers representing the overflow and its overlying upper oceanic layer. The Hallberg Isopycnal Model (HIM) is used (Hallberg, 1997). The overflow layer in the model must deal with the problem of vanishing layer thickness and HIM is known to handle this problem well. The amount of entrainment can also be prescribed in the model. (see http://www.gfdl.noaa.gov/$\simeq$rwh/HIM/HIM.html for details)

The model is kept simple with its externally determined parameters set close to the parameter space of the Faroe Bank Channel overflow (Figure 2-2a) (Borenäs and Lundberg, 2004). A setup close to the Faroe Bank Channel overflow is used because this overflow is one of the better-observed major overflows. The Coriolis parameter, f, is set to a constant, 1.4×10^{-4} s^{-1}, and the model domain is a rectangle (800 km $\times$ 400 km) that is separated into two basins. The smaller (southern) basin represents the marginal sea where dense water formation occurs and the overflow will originate from this small basin. The larger (northern) basin represents the continental slope region and the overflow will flow along the bathymetric contours in this region. We will examine the flow field that results through overflow-upper ocean interaction in

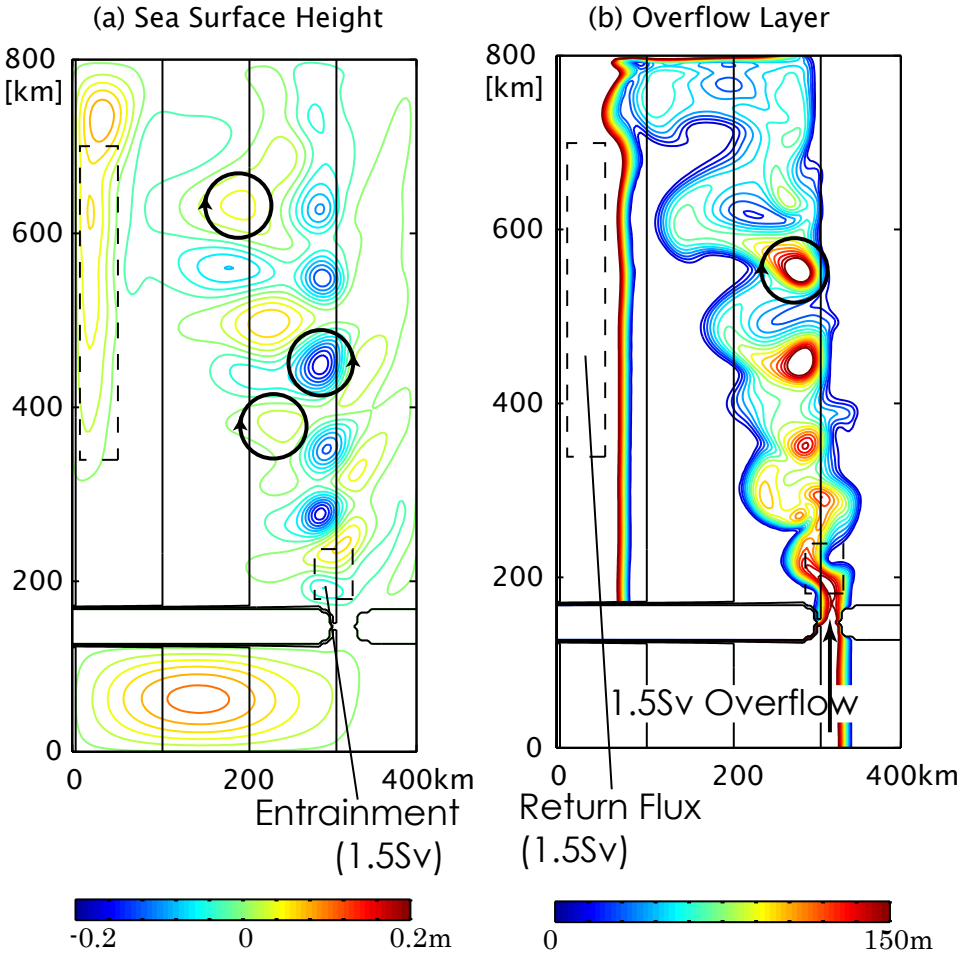

Figure 2-1: A snapshot of the two-layer model in a rectangular basin (Case 1). The small southern basin is the marginal sea and the large northern basin is the continental slope region. The black solid lines are the bathymetric contours representing -3000 m, -2000 m, and -1000 m depths with the shallower region to the right. The dotted square region is where entrainment from the upper layer to the overflow layer occurs. **(a)** Sea surface height contoured from -0.2 to 0.2 m with an interval of 0.02 m. Strong cyclonic and anticyclonic eddies are observed although the cyclonic eddies seem to outnumber the anticyclonic eddies. The eddies have a sea surface height of $\pm$ 15 cm, radius of 50 km and an azimuthal velocity of 40 cm s^{-1}. **(b)** Overflow layer thickness contoured from 0 to 150 m with an interval of 10 m. The overflow comes out of the small basin and flows onto the continental slope but it splits into an eddy immediately after exiting the strait. The overflow layer increases its width while descending down the continental slope. Anticyclonic eddies are observed to propagate roughly along the bathymetric contours but they also slowly descend the slope.

this large basin. The bottom topography in both basins has a slope of 0.01 with a shallower region to the right (east). The strait connecting the two basins is 16 km wide and 1000 m deep at the narrowest point of the strait. This strait topography has a slope of 0.01, the same as the two basins, so the bathymetric contours across the strait, from the marginal sea to the continental slope region, are straight. Therefore, the geostrophic contours run through the strait.

The interface between the upper ocean layer and the overflow layer will be initially set to 1000 m in the marginal sea and 3000 m in the continental slope region (Figure 2-2c). The reduced gravity, g', between the two-layers is set constant to 5×10^{-3} m s^{-2}, which is a density difference of 0.5 kg m^{-3}. The baroclinic deformation radius is about 16 km ($L_D = \sqrt{g'H}/f$), so the horizontal resolution of 4 km used in the model will just resolve this scale.

An overflow is created by pumping 1.5 Sv of mass into the overflow layer in the marginal sea and pumping an equal amount of mass out of the overflow layer in the off shore part of the continental slope region. Note that this forcing is applied only to the overflow layer and not to the upper layer, so there is no upper layer flow coming from the continental slope region to the marginal sea through the strait. The location of the entrainment is fixed between 20–80km from the strait and 900–1200 m depth (the squared region in Figure 2-2a). The magnitude of the entrainment is also fixed with a diapycnal velocity of 7.8×10^{-4} m s^{-1}, which makes the total entrainment 1.5 Sv. In order to conserve mass in each layer, the same amount of water that the overflow layer entrains from the upper layer near the strait will return to the upper layer in the off-shore region with its location and strength also fixed. The circulation forced by this return flux is trapped within the deep region and thus did not appear to disturb the circulation forced near the entrainment region and the on-shore region of the basin.

The momentum equations and the continuity equations solved in the numerical

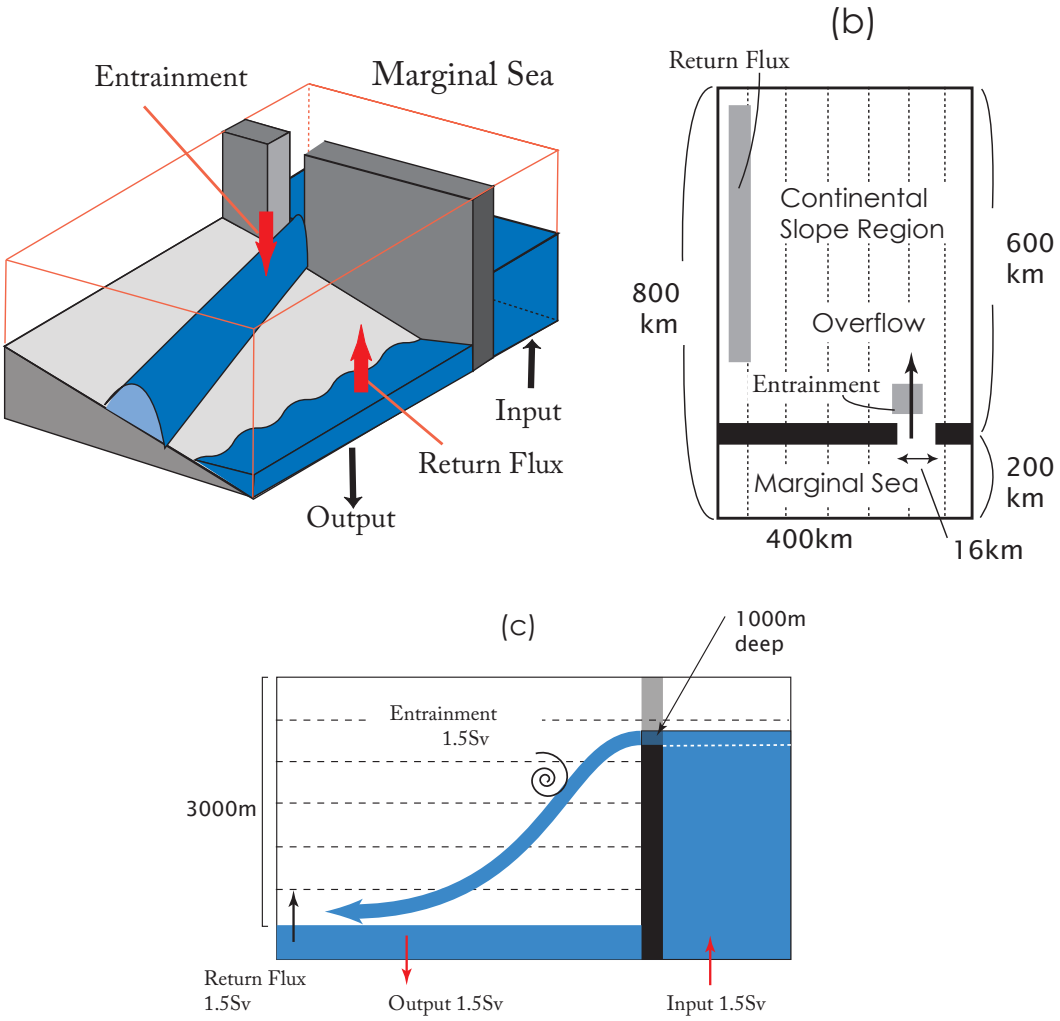

Figure 2-2: A schematic of the model configuration for investigating the overflow-upper ocean interaction in the continental slope region. **(a)** 3-D view **(b)** Birds Eye view: The domain is a rectangle, 800 km × 400 km, with two basins connected by a narrow strait 16 km wide and 1000 m deep. The smaller basin represents the marginal sea and the larger basin represents the continental slope region. The bottom topography in both basins has a slope of 0.01. The strait also has a slope of 0.01 so the bathymetric contours run across the strait. **(c)** A schematic view from the side. In order to create an overflow at the strait, mass is pumped into the overflow layer in the marginal sea and pumped out in the slope region. Note that this forcing is applied only to the overflow layer. Entrainment occurs soon after the overflow exits the strait. To balance mass, return flux is forced from the overflow to the upper layer.

model are

$$\frac{\partial u_1}{\partial t} + u_1\frac{\partial u_1}{\partial x} + u_1\frac{\partial v_1}{\partial y} - fv = -\frac{1}{\rho_o}\frac{\partial p_1}{\partial x} - K_4\nabla^4 u_1 - \nu_1 u_1, \tag{2.1}$$

$$\frac{\partial v_1}{\partial t} + v_1\frac{\partial u_1}{\partial x} + v_1\frac{\partial v_1}{\partial y} + fu = -\frac{1}{\rho_o}\frac{\partial p_2}{\partial y} - K_4\nabla^4 v_1 - \nu_1 v_1, \quad \text{and} \tag{2.2}$$

$$\frac{\partial h_1}{\partial t} + \nabla(u_1 h_1) = w^* \tag{2.3}$$

for the upper layer and

$$\frac{\partial u_2}{\partial t} + u_2\frac{\partial u_2}{\partial x} + u_2\frac{\partial v_2}{\partial y} - fv = -\frac{1}{\rho_o}\frac{\partial p_2}{\partial x} - K_4\nabla^4 u_2 - \nu_2 u_2, \tag{2.4}$$

$$\frac{\partial v_2}{\partial t} + v_2\frac{\partial u_2}{\partial x} + v_2\frac{\partial v_2}{\partial y} + fu = -\frac{1}{\rho_o}\frac{\partial p_2}{\partial y} - K_4\nabla^4 v_2 - \nu_2 v_2, \quad \text{and} \tag{2.5}$$

$$\frac{\partial h_2}{\partial t} + \nabla(u_2 h_2) = -w^* \tag{2.6}$$

for the overflow layer, where u, v, w^*, p, and h are the across slope velocity, along slope velocity, diapycnal velocity, pressure, and layer thickness. f, K_4 and ν are the Coriolis parameter, biharmonic viscosity coefficient, and the linear drag coefficient. Subscripts 1 and 2 represent the upper layer and the overflow layer. Biharmonic viscosity ($K_4 = 3 \times 10^9$ m^4 s^{-2}) is used for friction but a linear drag is also added to include the effect of the frictional bottom boundary layer. The coefficient ν is set to

$$\nu_1 = \begin{cases} \nu_o exp(-\frac{h_2-1}{10}) & h_2 > 1 \text{ m} \\ \nu_o & h_2 \leq 1 \text{ m} \end{cases} \quad \text{and} \tag{2.7}$$

$$\nu_2 = \nu_o \tag{2.8}$$

in each layers where $\nu_o = 1.50 \times 10^{-5} s^{-1}$. The upper layer will experience the bottom stress only when the interface is close to or directly in contact with the bottom topography. Hence the overflow layer will always experience the full bottom stress ($\nu_o \vec{u}$) while the upper layer will experience the full bottom stress only when the interface is within a meter from the bottom. If the interface is more than a meter away from the bottom, the effect of bottom stress on the upper layer will decay

Case	1	2	3
Number of Layers	2	1	2
Entrainment	1.5 Sv	1.5 Sv	Off
Overflow	1.5 Sv	Off	1.5 Sv
Maximum slope	0.01	0.01	0.01
Topographic Character	Straight	Straight	Straight
Planetary β (Open Ocean)	No	No	No
Region of primary focus	Faroe Bank Channel	Faroe Bank Channel	Faroe Bank Channel

Table 2.1: Comparison of the model: Case 1 to 3

exponentially as the interface becomes further away from the bottom topography. Note that this linear drag does not represent the vertical viscosity between the layers (the inter-facial friction) so it is not a function of shear stress between the layers.

In the following sections, we will investigate the overflow-upper ocean interaction using the model described above. The diabatic and adiabatic interaction will be examined separately before the full interaction is examined. The next section will examine the diabatic interaction.

2.2 Entrainment Driven Topographic β-plumes (Case 2)

To separate the diabatic interaction from the adiabatic interaction completely, the whole overflow layer is excluded from the model, reducing the model to a one-layer

system, consisting only of the upper layer.

The upper layer is forced by entrainment and a return flux. The basic equation for this model is

$$\frac{\partial u_1}{\partial t} + u_1\frac{\partial u_1}{\partial x} + u_1\frac{\partial v_1}{\partial y} - fv = -\frac{1}{\rho_o}\frac{\partial p}{\partial x} - K_4\nabla^4 u_1, \tag{2.9}$$

$$\frac{\partial v_1}{\partial t} + v_1\frac{\partial u_1}{\partial x} + v_1\frac{\partial v_1}{\partial y} + fu = -\frac{1}{\rho_o}\frac{\partial p}{\partial y} - K_4\nabla^4 v_1, \text{ and} \tag{2.10}$$

$$\frac{\partial h_1}{\partial t} + \nabla(u_1 h_1) = w^*. \tag{2.11}$$

These equations are basically the same as Eq 2.1 - 2.3 but the bottom friction by linear drag is neglected. This is because the upper oceanic layer, which we are focusing on here, would normally not be influenced by bottom friction significantly because the overflow layer will exist underneath.

The model is spun up from rest. After the barotropic topographic Rossby waves cross the basin, the model reaches a steady state. The sea surface height of the final steady state shows the formation of a cyclonic circulation by the mass sink aligned to the bathymetric contours (Figure 2-3), which are also the background PV contours of the model. This cyclonic circulation is the entrainment-driven topographic β-plume. A flow up the PV gradient (on-shore direction) is forced at the mass sink (1.5 Sv) and a down PV gradient flow (off-shore direction) is created at the northern boundary where the long topographic Rossby waves are dissipated. The northern boundary plays a role similar to that played by the viscous planetary western boundary layer for the planetary β-plume (Figure 1-4). Two jets along the PV contours have transports of 5.4 Sv (off-shore jet) and 3.9 Sv (in-shore jet). The anticyclonic gyre in the off-shore region is driven by the mass source (return flux).

There are two points that distinguish the topographic β-plume (Figure 2-3) from the planetary β-plume (Figure 1-4). Linear dynamics describes these two points sufficiently.

First, the transport in either branch of the topographic β-plume is on the order of the mass sink. We will mainly focus on the incoming (southward) branch of the

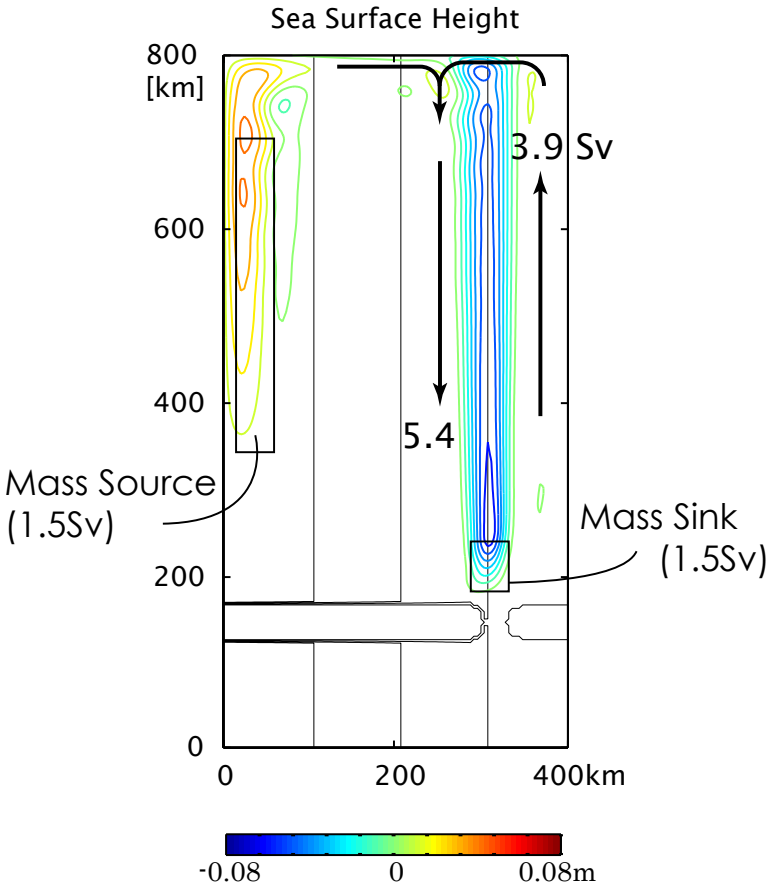

Figure 2-3: The sea surface height responding to the mass sink (entrainment) located in the square boxed region near the strait. The diapycnal velocity of the mass sink is $w^* = 7.8 \times 10^{-4}$ m s^{-1}. The flow field shows the cyclonic circulation along the constant bathymetric contours (background PV contours) which is the entrainment-driven topographic β-plume. A flow up the PV gradient is forced at the mass sink and a flow down the PV gradient is created at the northern boundary. The inflow to the mass sink has a transport of 5.4 Sv and the outflow has a transport of 3.9 Sv, close to the estimate from Eq 2.12. A mass source (Return mass flux) is located in the off shore location with $w^* = 1.2 \times 10^{-4}$ m s^{-1} to conserve mass in the upper layer and this mass source creates the anticyclonic gyre off-shore.

topographic β-plume in this thesis and will define the transport of this branch as the topographic β-plume transport. As mentioned in the previous chapter (Section 1.3), the topographic β-plume transport can be estimated from Eq 1.5 as

$$\frac{V}{W} = \frac{\frac{fw^*}{h}h}{\beta^* L_x} = \frac{f}{\beta^* L_x}. \tag{2.12}$$

Substituting $f = 1.4 \times 10^{-4}$ s^{-1}, $L_x = 32$ km, and $\beta^* = 1.2 \times 10^{-9}$ m^{-1}s^{-1}, the parameters used in Case 2, Eq 2.12 estimates $V/W = 3.7$ thus a topographic β-plume transport of 5.6 Sv. This estimate is close to what is observed in the model (5.4 Sv) (Figure 2-3).

Second, there is a noticeable difference between the transport in (5.4 Sv) and out (3.9 Sv) of the mass sink region. If V/W were large like the planetary β-plume for example ($V/W \simeq 100$), the difference between the transport of the inflow (V) and the outflow ($V - W$) would be negligible ($(V - W)/V = 1 - W/V = \simeq 1$). But when the background PV gradient is large because of the sloping topography, V/W is close to one so the difference between in and outflow transport is significant. This effect is the same as changing the entrainment size but fixing the background PV gradient as described in the previous chapter (Spall, 2000).

Barotropic Instability

So far, we have investigated the entrainment-driven topographic β-plume using only linear dynamics, which was sufficient to explain the model result of Case 2. But how valid is the linear assumption? Is the flow stable within the parameter space of our interest or is the cyclonic circulation of Case 2 a case that just happens to be barely stable?

Barotropic instability is the only mechanism that can make the entrainment-driven topographic β-plume become unstable in the one-layer model. The stability of the flow to barotropic instability can be tested by comparing the vorticity gradient of the two jets against the background vorticity gradient β^* (Pedlosky, 1987). Here we use scaling to examine whether the topographic β-plume may become barotropically

unstable. The jets are primarily in the along slope direction so the vorticity gradient of the two jets can be estimated as

$$\frac{\partial \zeta}{\partial x} \simeq \frac{|v_{jet} - (-v_{jet})|}{L_x^2} = \frac{2|v_{jet}|}{L_x^2}. \tag{2.13}$$

where v_{jet} is the velocity of the jet and L_x is the size of the mass sink in the across slope (+y) direction. The transport of the incoming branch of the topographic β-plume is estimated from the linear vorticity equation (Eq 1.2) as

$$V = uhL_y = \frac{fw^*}{\beta^* h} hL_y = \frac{fw^* L_y}{\beta^*}. \tag{2.14}$$

By taking the width of the incoming jet as half of the mass sink size ($L_x/2$), the transport of the incoming jet (V) can also be estimated as

$$V = v_{jet} h \frac{L_x}{2}. \tag{2.15}$$

Solving this equation for v_{jet},

$$v_{jet} = \frac{2V}{hL_x} \tag{2.16}$$

and substituting Eq 2.14, v_{jet} can be expressed as

$$v_{jet} = \frac{2\frac{fw^* L_y}{\beta^*}}{hL_x} = \frac{2fw^* L_y}{\beta^* hL_x}. \tag{2.17}$$

Now substituting this expression for v_{jet} to Eq 2.13, the vorticity gradient of the jet can be expressed using diapycnal velocity w^*:

$$\frac{\partial \zeta}{\partial x} \simeq \frac{2}{L_x^2} \frac{2fw^* L_y}{\beta^* hL_x} = \frac{4fw^* L_y}{\beta^* hL_x^3}. \tag{2.18}$$

The necessary condition for instability is when the vorticity gradient exceeds the

background vorticity gradient:

$$\beta^* \leq \frac{\partial \zeta}{\partial x} \simeq \frac{4 f w^* L_y}{\beta^* h L_x^3}. \tag{2.19}$$

So solving Eq 2.19 for w^*, the critical diapycnal velocity w_c^* that would satisfy this condition can be estimated as

$$w_c^* = \frac{\beta^{*2} L_x^3 h}{4 f L_y} = \frac{f \alpha^2 L_x^3}{4 h L_y}. \tag{2.20}$$

When an entrainment-driven topographic β-plume is forced with a mass sink that has a larger diapycnal velocity than w_c^*, the entrainment-driven topographic β-plume will be likely to satisfy the necessary condition for barotropic instability and may become unstable.

Substituting the parameter used in the model for f, α, L_y, and h, the critical diapycnal velocity w_c is estimated as 1.9×10^{-3} m s^{-1}, which is a large value for diapycnal velocity. The diapycnal velocity used in the model (7.8×10^{-4} m s^{-1}) was half the size of w_c, thus we expect that within the parameter space close to Case 2 (Figure 2-3) the entrainment-driven topographic β-plume is likely to be stable.

The strength of the diapycnal velocity (entrainment) is varied to test whether w_c is a good measure for the occurrence of barotropic instability. When w^* is larger than w_c, the model shows the entrainment-driven topographic β-plume becomes unstable and eddies form near the mass sink (Figure 2-4). The mean transport of the topographic β-plume is also less than the linear estimate when $w^* > w_c^*$ (Figure 2-5). The experiments find that the time-mean topographic β-plume transport starts to differ from the linear solution when the diapycnal velocity exceeds w_c. But within the range of our interest ($w^* = 10^{-4} - 10^{-3}$ m s^{-1}), the topographic β-plume was stable, and the linear solution gave a reasonable estimate of the topographic β-plume transport.

The response of the upper layer to the entrainment in the continental slope region was examined in this section by neglecting the active overflow layer. We have learned that a topographic β-plume forced by a local entrainment will form along the bathymetric contours with a transport on the same order as the mass sink. The

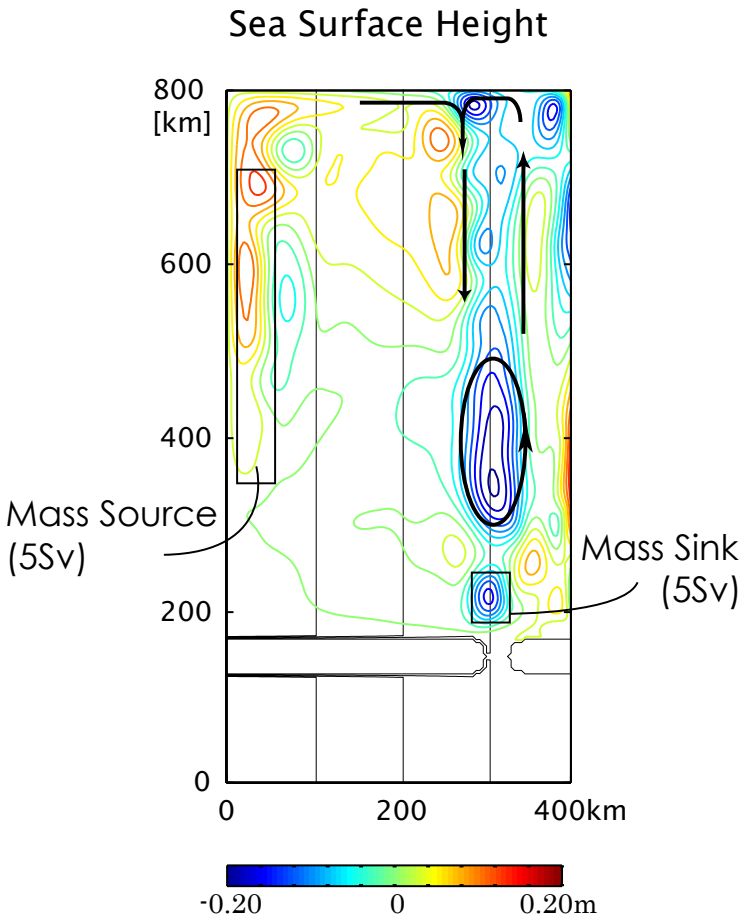

Figure 2-4: The sea surface height of the topographic β-plume when $w^* = 2.5 \times 10^{-3}$ m $^{-1} \gg w_c$. The model setup is exactly the same as the case shown in Figure 2-3 except for this diapycnal velocity strength. Contours are drawn from -0.2 to 0.2 m with an interval of 2.5 cm. The eddies form near the forcing region and the main structure of the topographic β-plume is broken into cyclonic eddies. The eddies have a velocity as large as 40 cm s^{-1}.

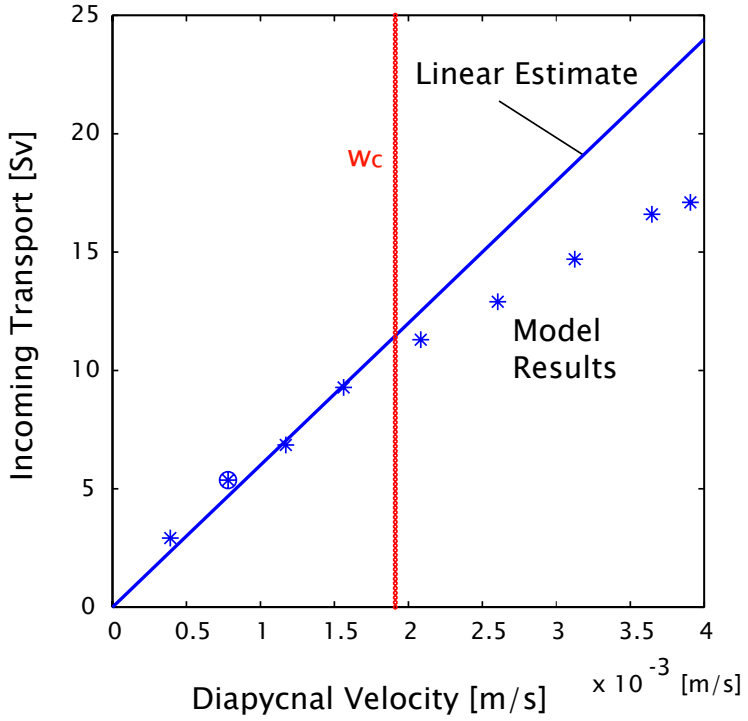

Figure 2-5: The topographic β-plume transport as a function of diapycnal velocity at the mass sink region. The blue solid line is the linear solution of the incoming transport of the topographic β-plume . The model calculation results are shown in asterisks and Case 2 is shown with a circle. The mean incoming transport shows a departure from the linear solution when w^* exceeds w_c, which is an scale estimate of the critical value of diapycnal velocity when the topographic β-plume is likely to satisfy the necessary condition of barotropic instability. Since w_c is relatively large for a diapycnal velocity, the figures also confirms that the linear solution estimates the topographic β-plume transport well within the physical space of our interest.

difference of transport between the inflow and the outflow from the mass sink region was also noticeable. Barotropic instability was found unlikely to occur within the parameter space of our interest so the linear vorticity balance gives a good estimate of the topographic β-plume transport.

In the next section, the adiabatic part of the overflow-upper ocean interaction will be investigated.

2.3 Eddy-Driven Topographic β-plumes (Case 3)

In this section, the adiabatic overflow-upper ocean interaction is investigated. A two-layer model is used with an overflow (1.5Sv) coming out of the strait from the marginal sea into the continental slope. But the entrainment from the upper layer to the overflow layer near the strait is shut off in order to separate the adiabatic interaction from diabatic effects. Thus, the only external forcing in the model is the mass input and output that creates the overflow coming out of the strait.

Strong eddies develop in both upper and overflow layers, which indicate that there is a strong adiabatic interaction between the two layers (Figure 2-6a and b). The focus of this section is to understand the role of these eddies and how they can affect the time-mean flow in the upper and overflow layer. First, the snapshot and time-mean flow field of the overflow layer and the upper layer are described in more detail. Second, the mechanism for the eddy formation is discussed. Third, the role of eddies in the upper layer is examined through PV and momentum balance. Last, the effect of eddies on the overflow layer is examined through energy balance.

2.3.1 The formation of an eddy-driven topographic β-plume

The model is spun up from rest and a statistically steady state is reached after 200 days. The snapshot of the sea surface height shows the formation of eddies with vorticity of both signs, a radius of 30 km, sea surface height of $\pm$10 cm, and an azimuthal velocity of 30 cm s^{-1} (Figure 2-6a). The snapshot of the overflow layer thickness shows the overflow splitting into anticyclonic eddies rather than a stream-

tube (Figure 2-6b). These eddies form roughly every 5 days and have a radius of 50 km. They also gradually dissipate and become a thin wavy layer as they travel further away from the strait.

In the interior of the basin, the overflow velocity fluctuated with a 4–6 day period. This period matches the formation rate of the anticyclonic eddies observed in the overflow layer (Figure 2-6b). The overflow is as fast as 50 cm s^{-1} and flows dominantly in the northward (+y) direction (Figure 2-7). The velocity within the overflow also never reverses, even in the presence of eddies, since the background velocity is much larger than the fluctuations. The velocity in the upper layer also shows a fluctuation with a 4–6 day period. But unlike the overflow, there is no significant background mean flow so it shows the velocities turning anticyclonically as anticyclones pass by.

A vertical section through one of the overflow eddies shows that these eddies are quite thin, about 100 m, compared to the upper layer thickness which is about 1000 m (Figure 2-8). The overflow velocity is as large as 50 cm s^{-1} and shows larger values of velocity on the off-shore side of the layer because the overflow eddies are anticyclonic. The upper layer velocity is about 10 cm s^{-1}. It also shows the presence of an anticyclone which is also observed from the snapshot of the sea surface height. Although the magnitude of the upper layer velocity is small compared to the overflow, the transport of these eddies becomes of the same order or sometimes larger than the overflow transport because the upper layer is so thick.

The time-mean sea surface height shows the formation of a time-mean circulation, which we will call "the eddy-driven" topographic β-plume (Figure 2-9a). The off-shore cyclonic gyre and the on-shore anticyclonic gyre have a transport of roughly 1.2 Sv and 0.8 Sv, respectively, and are as large as that of the overflow. The big difference between the eddy-driven topographic β-plume and the entrainment-driven topographic β-plume (Case 2, Table 2.1) is its structure. The eddy-driven topographic β-plume has two gyres rotating in opposite directions unlike the entrainment-driven topographic β-plume which is a single gyre. The dynamical reason for the eddy-driven topographic β-plume being a double gyre and not a single gyre is given later in Section 2.3.3.

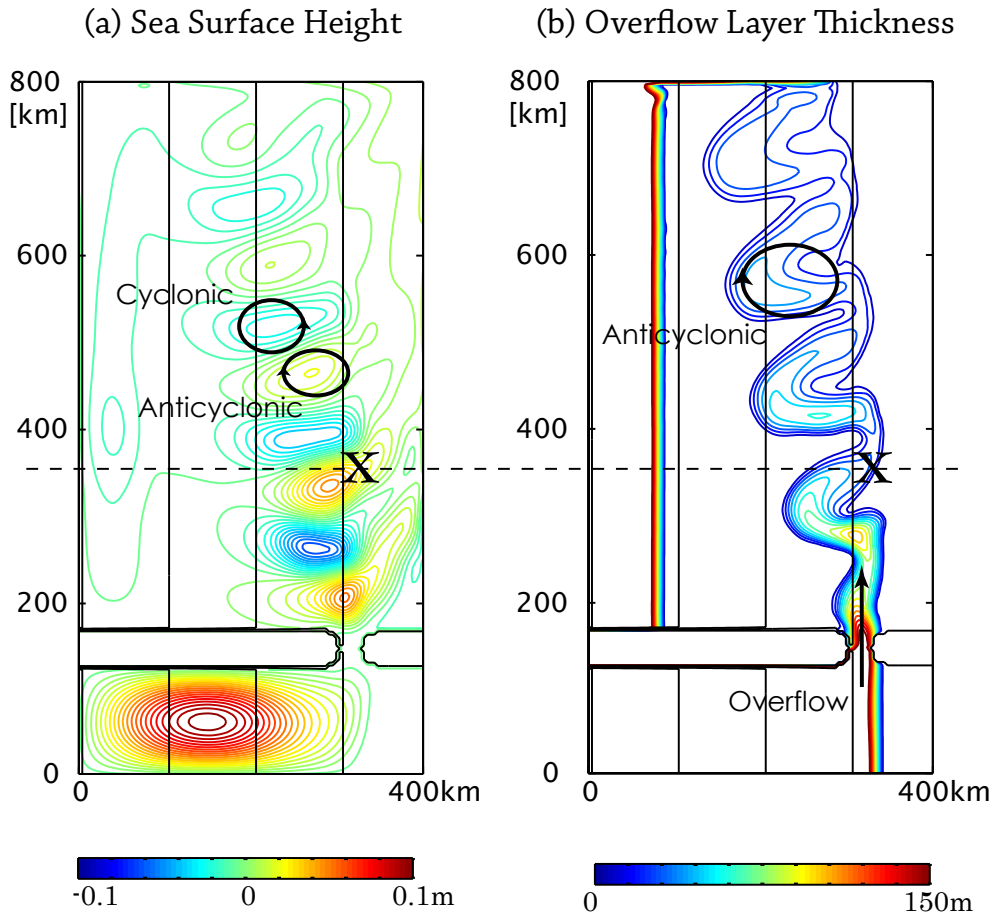

Figure 2-6: A snapshot of Case 3. A two-layer model with an overflow coming out of the strait but without entrainment. **(a)** The sea surface height contoured from -10 to 10 cm with an interval of .5 cm. Eddies are observed with a vorticity of both signs, a radius of 30 km, sea surface height of ± 10 cm, and an azimuthal velocity of 30 cm s^{-1}. **(b)** The overflow layer thickness contoured from 0 to 150 m with an interval of 10 m. The overflow comes out of the strait and then splits into anticyclonic eddies. These eddies form roughly every 5 days, have a radius of 50 km, and flow roughly along the continental slope. The eddies gradually become a thin wavy layer as they travel further away from the strait.

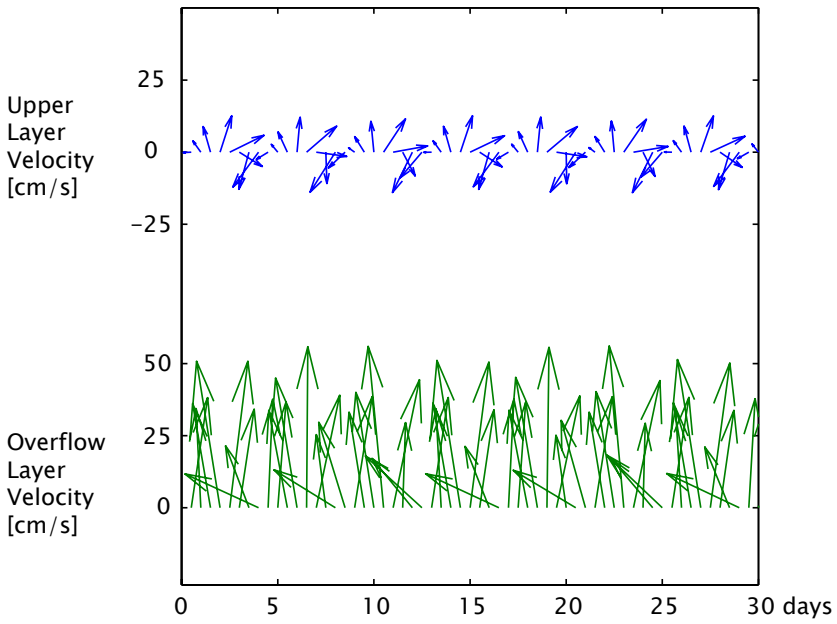

Figure 2-7: A time series of the velocity at point X in Figure 2-6. The overflow velocity always shows a northward (+y) flow and because the background flow is overwhelmingly large, the direction of the velocity does not change even in the presence of eddies. The time series also shows a 4–6 day signal which roughly corresponds to the eddy formation rate. The upper layer velocity also shows a 4–6 day signal. The velocity is turning primarily in an anticyclonic sense reflecting the anticyclones passing by. This, in the time-mean, results in a time-mean anticyclonic circulation in the region (Figure 2-9a).

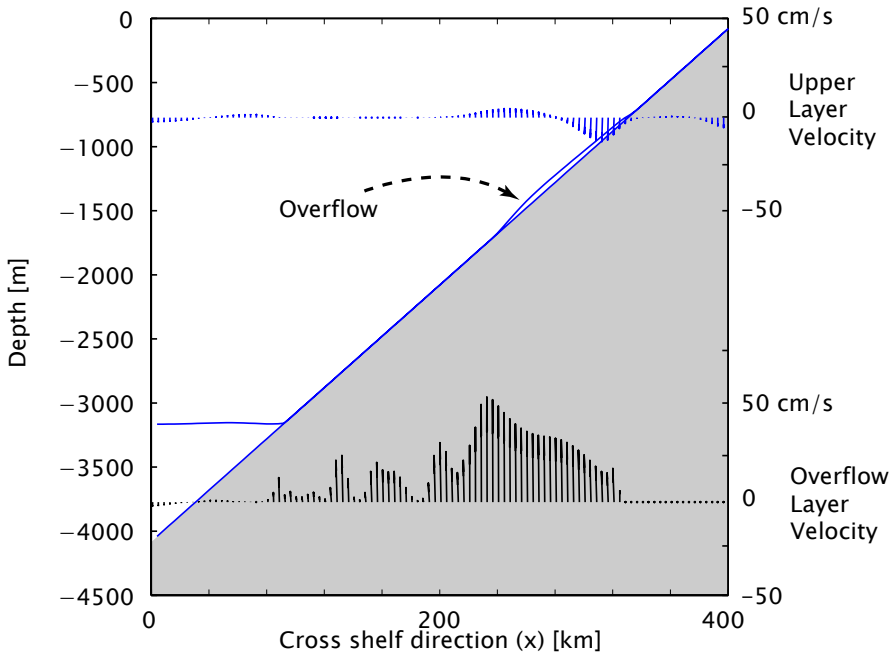

Figure 2-8: A vertical section at 200 km downstream from the strait. This cross section is shown as the dotted line in Figure 2-6. The velocity in the overflow layer is as large as 50 cm s^{-1} and is much larger than the upper layer (10 cm s^{-1}). The overflow velocity also shows larger values on the off-shore side which reflects the anticyclonic eddies in the overflow layer on top of the strong northward background flow.

The time-mean overflow layer thickness shows that while the overflow flows along the bathymetric contours, it also descends the slope at the ratio of 0.2 near the strait (Figure 2-9). This rate exceeds that of the frictional Ekman number ν/f, 0.1, and indicates that the overflow lost its momentum to something other than bottom friction, which is likely to be the upper layer. However, this increase of the rate of descent is observed only near the strait. Farther from the strait, the mean flow is basically descending at the rate of the frictional Ekman number.

Thus, an adiabatic interaction between the overflow and the upper ocean layer was shown to force eddies in both layers. The eddies forced an eddy-driven topographic β-plume in the upper layer with a transport comparable to the overflow. The eddies also affected the overflow layer by making it descend at a steeper angle than the frictional Ekman number. In the next subsection, the mechanism for the eddy formation is examined.

2.3.2 The mechanism for the eddy formation

In this subsection, we will discuss the mechanism for creating the eddies observed in the overflow and the upper layer in Case 3. The external parameters in the model are varied to determine the parameter dependence of the eddy formation.

The behavior of eddies, such as the location of eddy formation or the intensity of eddies observed at the surface, changes when the external parameters of the model change. When the upper layer thickness (H) increases from 1000 m to 3000 m from the model used in Case 3 eddies did not develop; thus, the eddy-driven topographic β-plume do not form (Figure 2-10a). A thicker upper layer leads to smaller upper layer motion, so this example implies that the upper layer motion is important for the eddy formation. The sensitivity of eddy behavior to other external parameters such as α, g', and f are also observed (Figure 2-10b-d).

What is the controlling parameter for the formation of eddies? A plausible mechanism for the eddy formation is baroclinic instability (Swaters, 1991). The thickness of overflows typically has a parabolic-like cross-section (Figure 2-11), thus when the Rossby number is small, the PV gradient of the overflow is negative on the off-shore

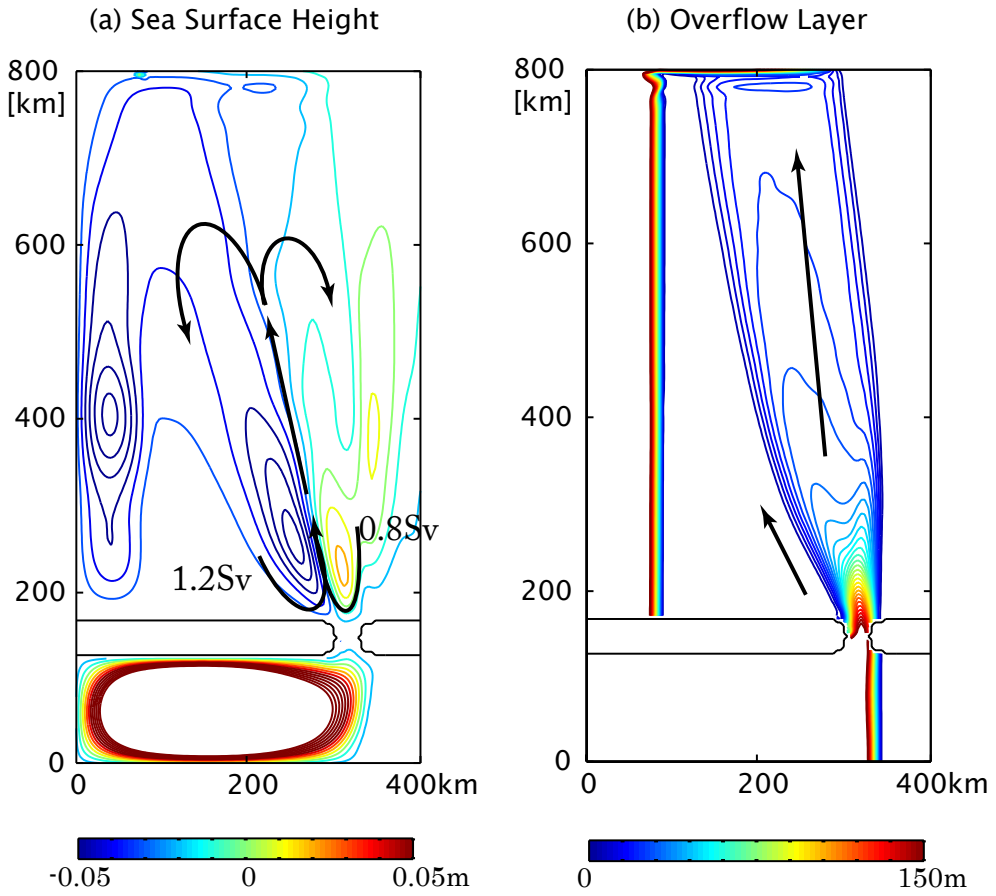

Figure 2-9: Time-mean flow field for Case 3 (Table 2.1). **(a)** Sea surface height contoured between -5 cm to 5 cm with an interval of 0.2 cm. Notice that this contour interval is much smaller than what was used for the snapshot (Figure 2-6a). An eddy-driven β-plume forms with two gyres rotating in opposite directions. The off-shore cyclonic gyre and the on-shore anticyclonic gyre have a transport of roughly 1.2 Sv and 0.8 Sv respectively and are comparable to that of the overflow. (The jet in the center has 2.0 Sv.) **(b)** The overflow layer thickness contoured from 0 to 150 m with an interval of 10 m. The layer shows steeper descent than the frictional Ekman number near the strait, but further downstream, it descends at the rate of the frictional Ekman number.

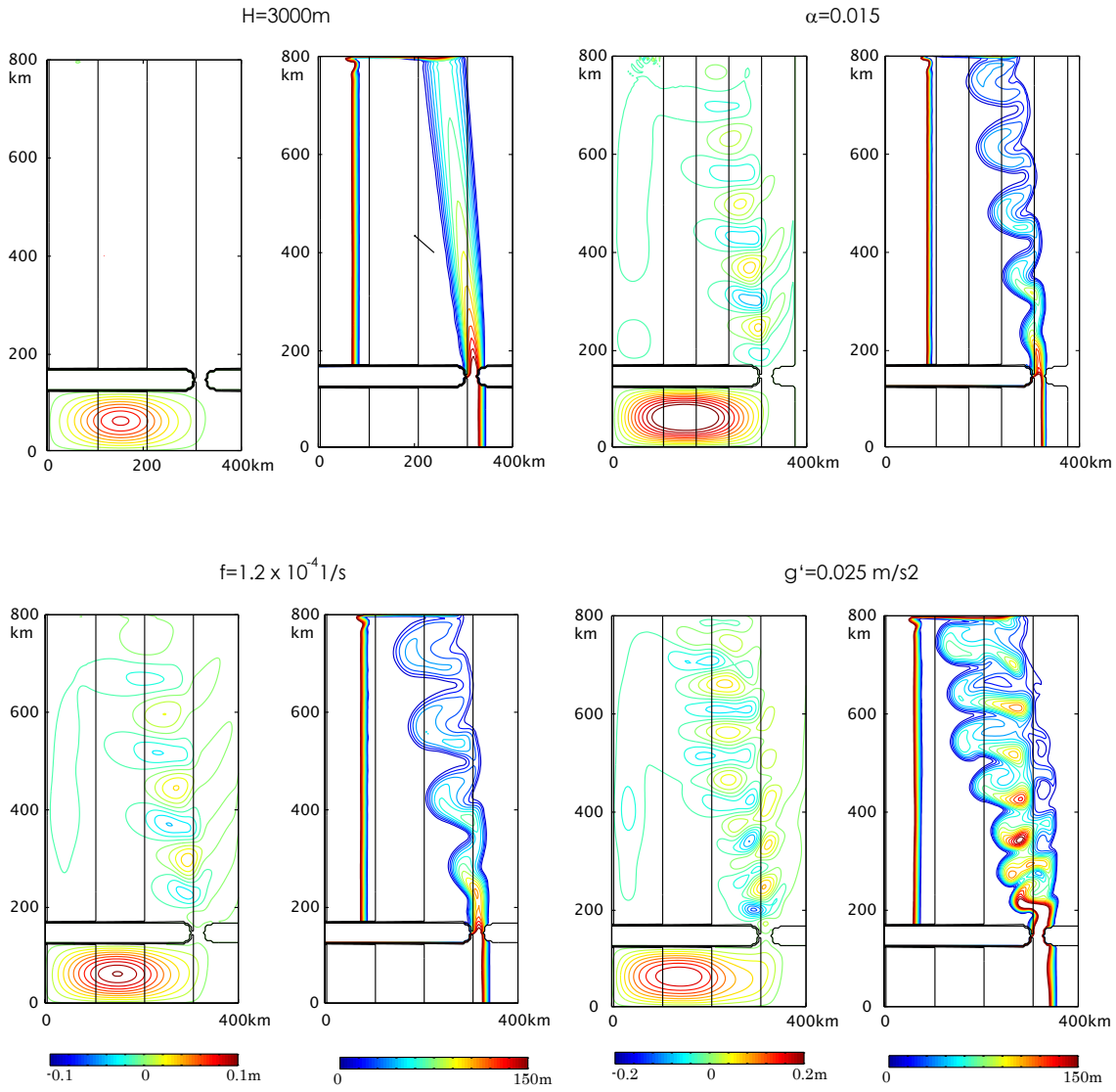

Figure 2-10: A snapshot view of four model results when parameters are varied from Case 2. The title shows which of the parameters were changed compared to Case 2. All other parameters remain fixed. The left of each case is the sea surface height contoured from -10 to 10 cm every 1 cm. The right is the overflow layer thickness contoured from 0 to 150 m every 10 m. All figures are contoured with this contour lines. Black solid lines show the bathymetric contours every 1000 m with shallower side to the right. **(a)** H=3000 m: No eddies form. Thus there is no flow in the upper layer. **(b)** $\alpha = 0.015$: The overflow becomes unstable at a distance slightly farther from the strait than Case 2. The radius of the eddies is similar to those in Case 2 but each eddy is spatially farther apart. **(c)** $f = 1.2 \times 10^{-4}$ s^{-1}: The overflow becomes unstable at a distance slightly farther than Case 2 like (b). The eddies are also larger and spatially farther apart than Case 2. **(d)** g'=0.025 m s^{-2}: The overflow becomes unstable immediately after exiting the strait. The eddies are smaller and are spatially closer to each other than Case 2.

side but is positive on the on-shore side. The PV gradient of the upper layer remains positive through out the region since its layer thickness change is mostly controlled by the slope. The existence of opposite signs of PV gradient satisfies the necessary condition for baroclinic instability and therefore, overflows are likely to become baroclinically unstable. The analytical solution of the growth-rate for baroclinic instability between the parabolic shaped overflow and the upper layer is derived by Swaters (1991) and this solution gives a reasonable estimate for when instability occurs in the model. First, this analytical solution is described briefly (see Swaters (1991) for details). Then the analytical solution is compared with the numerical model results.

The solutions for the growth-rate and the phase velocity of the instability are derived by first non-dimensionalizing the momentum and continuity equations. Velocity is scaled by the topographic Rossby wave speed (Nof, 1983)

$$u = \frac{\alpha g'}{f} \tag{2.21}$$

and the length scale in x and y are scaled by the deformation radius

$$L = L_D = \frac{\sqrt{g'H}}{f}, \tag{2.22}$$

where H is the basic thickness of the upper layer (Figure 2-11). The order $O(g'\eta_1/g)$ terms are neglected because the focus is on the baroclinic behavior of the two layers. Further assumptions are that the order one balance of the flow is geostrophy, the overflow layer thickness is parabolic, and that the frictional Ekman number is much less than one.

The solution for the non-dimensional growth-rate depends on two non-dimensional parameters, a and μ:

$$a = \frac{A}{L_D} \tag{2.23}$$

$$\mu = \frac{h_2/L_D}{\alpha}, \tag{2.24}$$

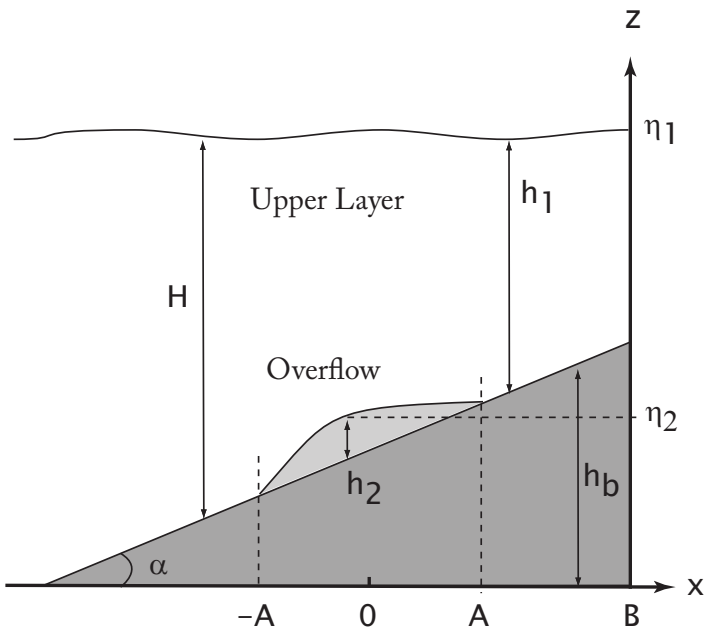

Figure 2-11: Schematic of the parameters used for solving the growth-rate, adapted from Swaters (1991). The overflow layer is assumed parabolic $h_2 = 1 - (x/A)^2$ and x axis is taken from the center of the overflow. The coast is located at $x = B$ and H is the basic thickness of the upper layer. Other parameters are the same as other equations used in this chapter.

where a is the overflow half-width (A) scaled by the deformation radius and μ is the thickness gradient of the overflow layer compared to the slope. For Case 3 ($a = 1.3$ and $\mu = 0.94$), the growth rate has a maximum (σ_{max}) at $k = 1.1$, which is roughly the wavenumber for the deformation radius scale (Figure 2-12). The maximum growth-rate increases with μ and is more sensitive to this parameter than a (Figure 2-13). In other words, the instability is more sensitive to the slope and overflow thickness than the overflow width.

The analytical solution of Swaters (1991) gives a reasonable estimates of when instability occurs in the model (Figure 2-14). The estimate of the distance required for full growth of instability is $l = \sigma_{max}^{-1} \cdot c$, where c is the phase velocity. Assuming that the instability starts to grow immediately after the overflow exits the strait, l will give an estimate of where the flow might become unstable. This non-dimensional parameter l appears to capture the dependence of where instability occurs in the model (L) reasonably well, where L is the distance between the strait and the location of negative maximum eddy PV flux (the reason why this shows where instability occurs will be described in the next section). Note that the values of l and L/L_D do not exactly match likely because l is the estimate based on linear perturbations where as L/L_D is a results of finite amplitude instability and is only one way of measuring where the instability occurs. Although there are some differences with each parameter (f, a, g' and H), instability occurs close to the strait when l is small and instability occurs far from the strait when l is large. The distance required for full growth of eddies is also sensitive to the linear drag coefficient ν_o used in the model. Larger ν_o leads to longer distance and smaller ν_o leads to shorter distance. Larger ν_o also appears to damp instabilities although l would still capture the dependence of when instability occurs in the model reasonably well. The size of the eddies observed in the model also matches with the wavelength that estimates maximum growth-rate of the instability, consistent with the results of Helfrich (2006).

Thus, baroclinic instability is a plausible mechanism for creating the eddies observed in Case 3. The analytical solution for the distance required for the baroclinic instability to grow (Swaters, 1991) gives a reasonable estimate for when the insta-

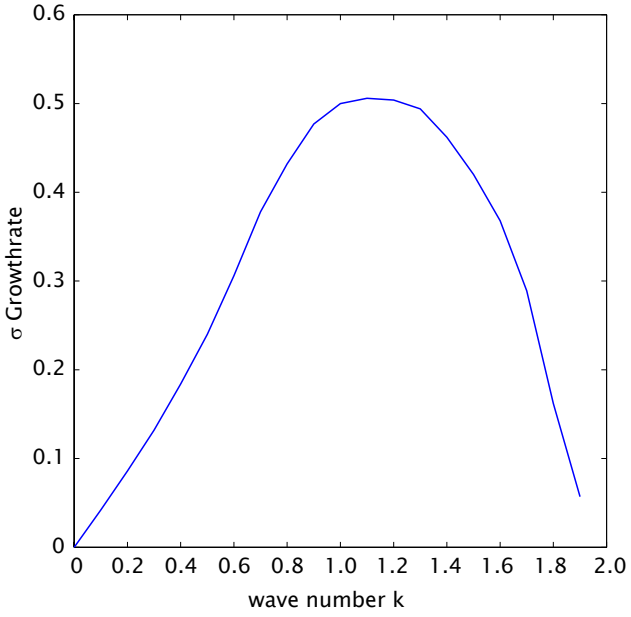

Figure 2-12: The non-dimensional maximum growth-rate against k for $\mu = 0.94$ and $a = 1.3$ based on Swaters (1991) (Case 3). The growth rate shows a maximum when $k \simeq 1.1$ roughly near the wavenumber that corresponds to the deformation radius scale.

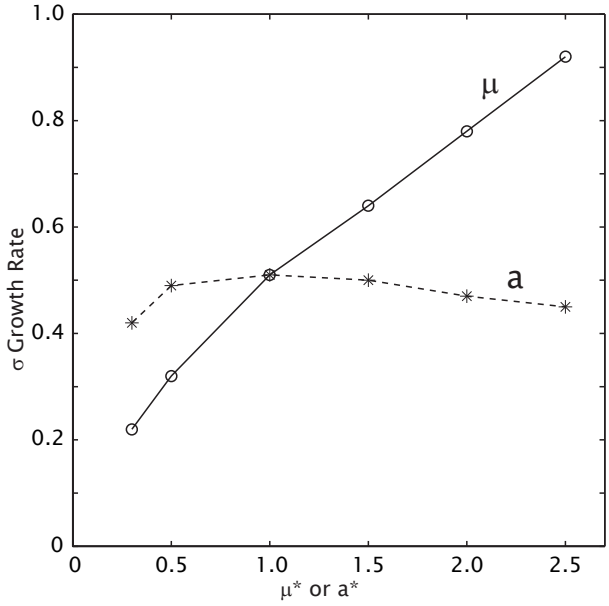

Figure 2-13: The change in non dimensional maximum growth-rate when μ and a are varied based on Swaters (1991). μ and a are normalized: $\mu^* = \mu/\mu_o$ and $a^* = a/a_o$, using $\mu_o = 0.94$ and $a_o = 1.3$, the values in Case 3. The solid line with circles represents the maximum growth-rate when μ^* is varied. The dashed line with asterisks represents the maximum growth-rate when a^* is varied. The plot shows that the maximum growth-rate is more sensitive to changes in μ rather than a.

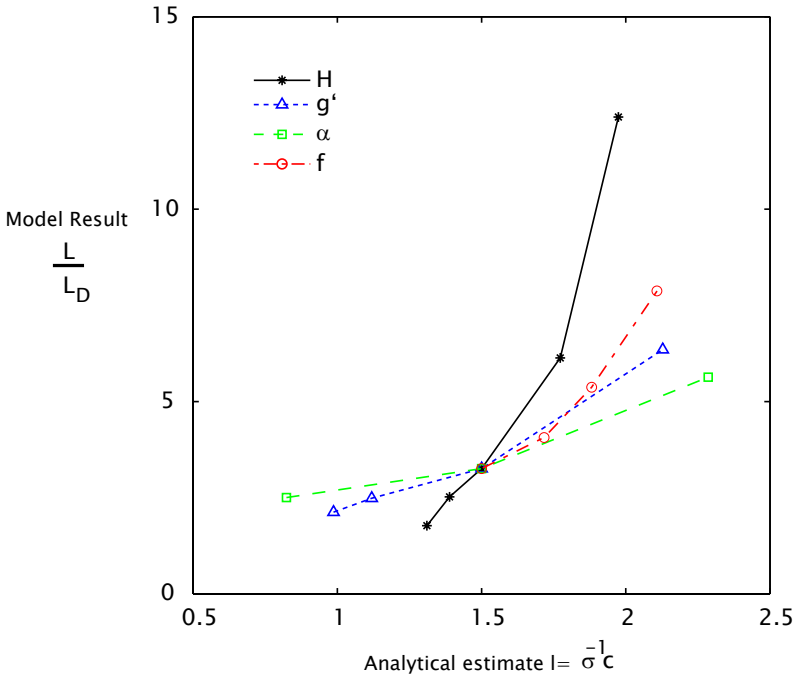

Figure 2-14: The analytical estimate for the distance required for full growth of instability $l = \sigma_{max}^{-1} \cdot c$ (Swaters, 1991) is compared against the distance estimated from model calculations. The distance where the eddy reaches full growth (L) in the model is non-dimensionalised by the deformation radius L_D, where L is estimated by the distance between the strait and the location of negative maximum eddy PV flux (see next section for why this is a reasonable choice here). l captures the increase of $\frac{L}{L_D}$ reasonably well, although there are some differences in the rate of increase depending on what external parameter is varied (f, a, g' and H). The external parameters are varied near the parameter space of Case 2, which is located at the center of each line. Black solid line with an asterisk is when H was varied. Blue dotted line with a triangle is when g' was varied. Green dashed line with a rectangle is when α was varied. Red dot-dash line with a circle is when f was varied.

bility occur and eddies form. Note that the eddies in the overflow layer observed in the model experiments are anticyclones and are associated with cyclones in the upper layer, unlike the barotropic cyclones observed by Spall and Price (1998). From laboratory experiments, Etling et al. (2000) suggested that the two cases are dynamically different regimes and that μ is smaller when the barotropic cyclones form. However, our model experiments do not form barotropic cyclones when μ is small thus μ may not be the appropriate parameter that distinguish the two regimes. The Denmark Strait overflow, which Spall and Price (1998) focused on, is a two-layer overflow (strong stratification within the overflow layer) and is quite different from a single layer overflow like the Faroe Bank Channel overflow and the model used in this chapter. The strong stretching of the upper overflow layer present in the Denmark Strait overflow does not exist for a single layer overflow and therefore, the PV dynamics of the water column is likely to be quite different between the two cases.

2.3.3 The role of eddies

The eddies created by baroclinic instability are the main driving force for establishing the time-mean circulation in the upper layer (Figure 2-9). But why do these eddies establish a topographic β-plume with two gyres rotating in opposite directions? In this section, we will examine the role of eddies in establishing the double gyre topographic β-plume by examining the PV and momentum balance of the upper layer.

The PV Balance

We will first derive the Reynolds averaged vorticity equation that shows the PV balance of the flow field and how eddies are capable of driving a time-mean circulation.

The full vorticity equation is

$$\frac{\partial \zeta}{\partial t} + \nabla \cdot (\mathbf{U}q) = \hat{k} \cdot \nabla \times \mathcal{F}, \tag{2.25}$$

where $\mathcal{F}$ is friction

$$\mathcal{F} = -K_4 \nabla^4 \mathbf{u} - \nu \mathbf{u} \tag{2.26}$$

and $\mathbf{U}$ is the layer integrated velocity $\mathbf{u}h$. By taking a time-mean of Eq 2.25 and separating variables into their time-mean and perturbation, the Reynolds averaged vorticity equation is

$$\overline{\mathbf{U}} \cdot \nabla \overline{q} = \overline{q} w^* - \nabla \cdot (\overline{\mathbf{U}' q'}) + \hat{k} \cdot \nabla \times \overline{\mathcal{F}}. \tag{2.27}$$

$-$ and $'$ represent the time-mean and perturbation respectively. Eq 2.27 is the balance equation at a point where the PV advection term ($\overline{U} \cdot \nabla \overline{q}$) on the LHS is balanced by the diabatic PV forcing ($\overline{q} w^*$), eddy PV flux divergence ($\nabla \cdot \overline{\mathbf{U}' q'}$), and friction terms on the RHS.

The PV balance equation (Eq 2.27) shows that there are two ways for an external forcing to drive a mean flow across the PV gradient. One is through diabatic PV forcing and the other is through eddy PV flux divergence. If a diabatic PV forcing exists in the interior of a basin, an entrainment-driven topographic β-plume will form, which is the circulation described in the previous section (Figure 2-3). If an eddy PV flux divergence is forced in the interior of a basin, a time-mean circulation, which we will refer to as "the eddy-driven" topographic β-plume, will form. The balance between the PV advection term and the eddy PV flux divergence term has been termed the "Turbulent Sverdrup Balance" (Haidvogel and Rhines, 1983) and has been shown to be a leading PV balance for an eddy-induced mean flow in a closed basin.

In Case 3, where no diapycnal forcing exists, the main PV balance near the strait is the turbulent Sverdrup balance (Figure 2-15). The eddies created by baroclinic instability (see previous section) force two regions of eddy PV flux divergence with opposite sign near the strait(Figure 2-15b). Since the mean PV gradient of the upper layer is positive throughout the continental slope region, the two regions of eddy PV flux divergence will force a bi-directional time-mean flow across the PV gradient

(Figure 2-15a). These bi-directional time-mean flows near the strait give rise to the double gyre structure of the eddy-driven topographic β-plume.

The eddy PV flux and the momentum balance

The eddy-driven topographic β-plume has two gyres because the eddy PV flux divergence has two regions of opposite sign near the strait. Why does the eddy PV flux divergence have two regions of opposite sign? It is because the eddy PV flux has a negative maximum. This explanation is the simple straightforward explanation, however, it does not fully answer the question. We are still left with the question why a negative maximum eddy PV flux exists in the first place. Why not a positive maximum? for example. Here, we will show that a negative maximum eddy PV flux is created by the momentum transfer from the overflow to the upper layer. We will first explain what eddy PV flux represents dynamically. Then the connection of the eddy PV flux to the momentum balance and baroclinic instability between the two layers is discussed.

The Quasi-Geostrophic (QG) Equations are used to explain what eddy PV flux is. (The upper layer in the model does satisfy the assumptions for QG.) The equivalent of eddy PV flux for a QG system is the eddy QGPV flux. The Reynold's averaged QGPV equation is

$$\overline{\mathbf{u}} \cdot \nabla \overline{Q} = -\nabla \cdot \overline{(\mathbf{u}' Q')} + \hat{k} \cdot \nabla \times \overline{\mathcal{F}} \tag{2.28}$$

where Q is the QGPV

$$Q = f + \zeta - \frac{f_o h}{H}. \tag{2.29}$$

f_o, h, and H are the Coriolis parameter, the upper layer thickness fluctuation and the basic upper layer thickness, respectively. The diabatic term is not included in Eq 2.28 because our focus is on the adiabatic eddy-driven topographic β-plume.

The eddy QGPV flux divergence term can be split into a divergence of along

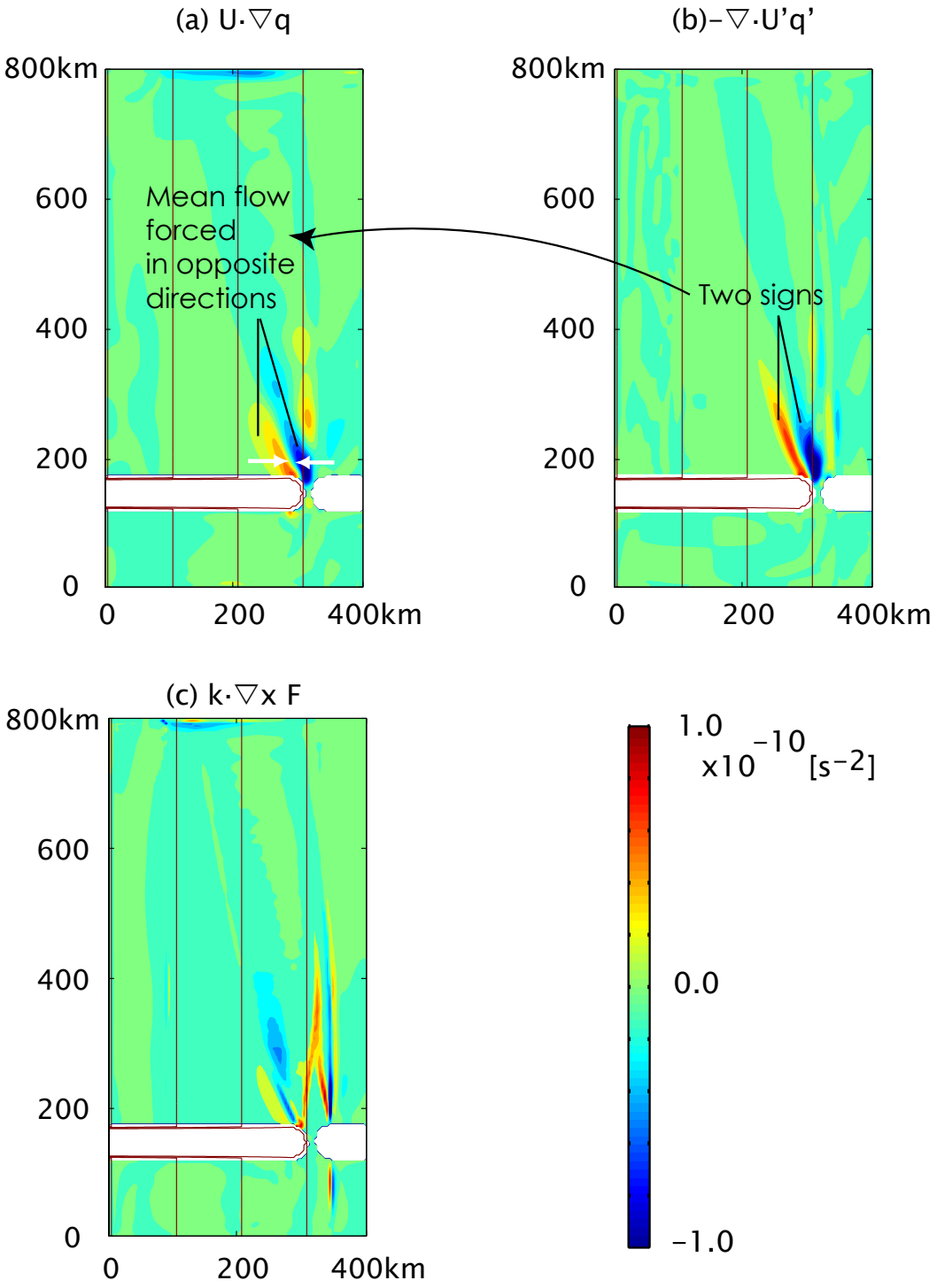

Figure 2-15: Each of the terms in Vorticity equation: Eq 2.27. **(a)** PV advection term ($\mathbf{U} \cdot \nabla q$) **(b)** Eddy PV flux divergence term ($-\nabla(\mathbf{U}'q')$) and **(c)** Dissipation term ($\hat{k} \cdot \nabla \times F$). The above balance shows (a) and (b) having two signs and balancing each other near the strait. This is the main balance of the eddy-driven topographic β-plume. The two signs show that the mean flow is bi-directional, making the time-mean circulation double gyre structure. The dissipation term shows large values where the interface intersects the bottom topography.

isopycnal and across isopycnal eddy stresses:

$$
\begin{aligned}
-\nabla \cdot \overline{\mathbf{u}'Q'} &= -\frac{\partial}{\partial x}\left(\overline{u'\zeta'} - \frac{f_o\overline{u'h'}}{H}\right) - \frac{\partial}{\partial y}\left(\overline{v'\zeta'} - \frac{f_o\overline{v'h'}}{H}\right) && (2.30)\\
&= -\nabla \cdot \left(\overline{u'\zeta'}, \overline{v'\zeta'}\right) - \nabla \cdot \left(-\frac{f_o\overline{u'h'}}{H}, -\frac{f_o\overline{v'h'}}{H}\right) && (2.31)\\
&= -\nabla \cdot (\mathbf{M_a} + \mathbf{M_b}) && (2.32)
\end{aligned}
$$

where M_a and M_b are

$$
\begin{aligned}
\mathbf{M_a} &= \left(\overline{u'\zeta'}, \overline{v'\zeta'}\right) \quad \text{and}\\
\mathbf{M_b} &= \left(-\frac{f\overline{u'h'}}{H}, -\frac{f\overline{v'h'}}{H}\right). && (2.33)
\end{aligned}
$$

$\mathbf{M_a}$ is the eddy relative vorticity flux, which represents the divergence of eddy momentum flux along isopycnal layer ($\simeq$ horizontal). $\mathbf{M_b}$ is the form drag which represents the divergence of eddy momentum flux across isopycnal layers ($\simeq$ vertical).

$\mathbf{M_a}$ and $\mathbf{M_b}$ for Case 3 does show the M_{bx} term, the form drag term in x, as the dominant term and shows the other terms smaller than the M_{bx} term (Figure 2-16). Thus M_{bx} is the main term that is creating the negative maximum eddy PV flux. The dynamical reason of why a negative maximum eddy PV flux exists near the strait is because of this form drag that is fluxing momentum across isopycnal layers dominantly from the overflow to the upper layer. The upper layer does not have any external forcing so this result confirms that the momentum transfer across layers is the driving force for the eddy-driven topographic β-plume to form in the upper layer.

The form drag term, M_{bx}, also reflects the thickness balance in x because it has the $\overline{u'h'}$ component. The negative eddy PV flux region is also an area of positive eddy thickness transport. To balance this thickness transport in the upper layer, a negative eddy thickness transport exists in the overflow layer. This transport is advecting the overflow thickness off-shore (Figure 2-9). These eddy thickness transports occurring in the upper and overflow layers are equal and opposite and confirm that baroclinic instability is the mechanism for creating the eddies.

What effect do eddies have on the overflow layer? The overflow layer has its largest

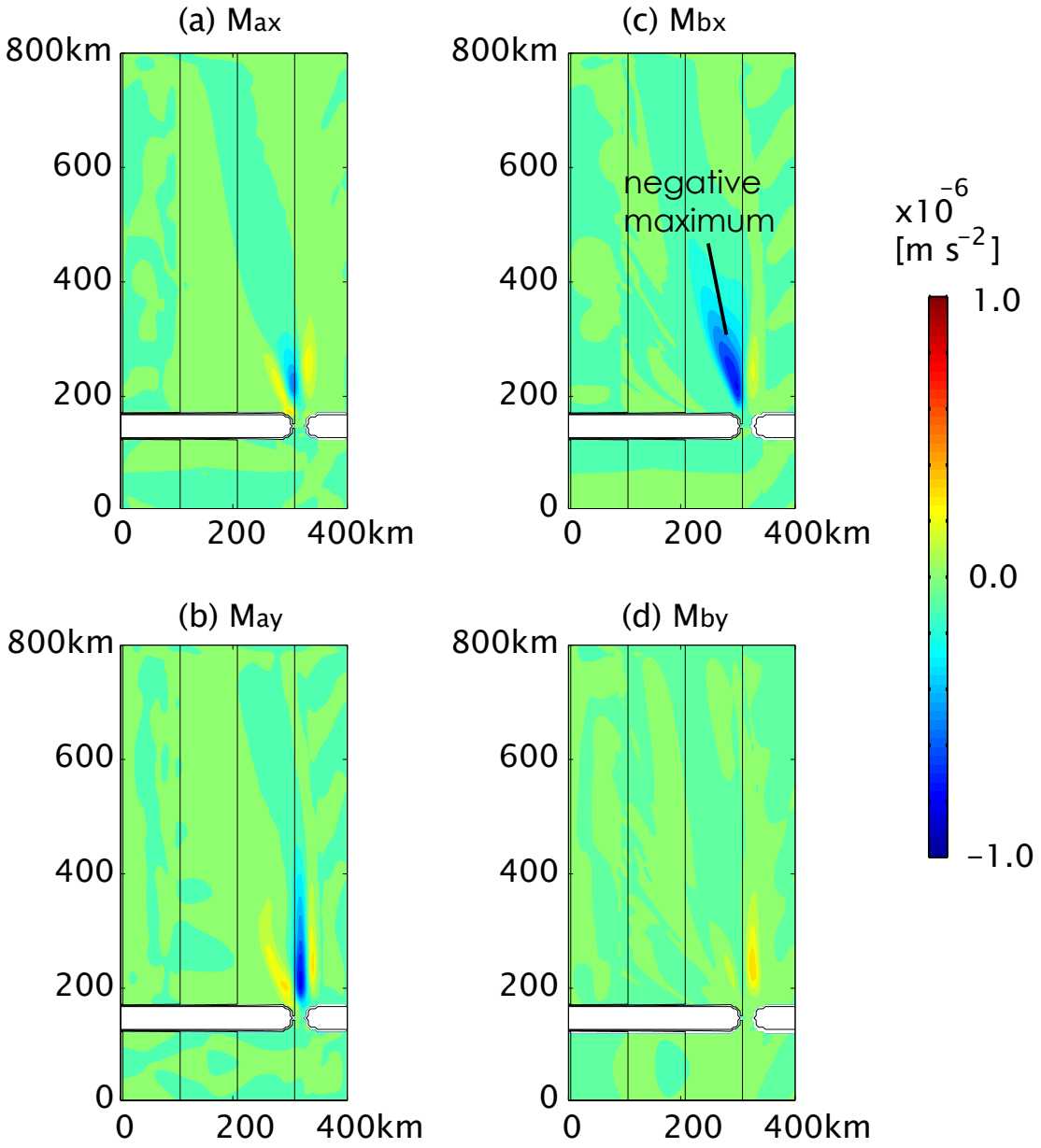

Figure 2-16: **(a)** M_{ax}: The eddy relative vorticity flux in x-direction ($\overline{u'\zeta'}$). The magnitude is smaller than M_{by} and also has two positive peaks near the strait. **(b)** M_{ay}: The eddy relative vorticity flux in y-direction ($\overline{v'\zeta'}$). The magnitude is somewhat comparable to M_{bx} but since the term has a y-direction structure, the $\partial M_{ay}/\partial y$ becomes small and thus is not a major component deciding the magnitude of the eddy PV flux divergence. **(c)** M_{bx}: Form drag in x. This is the largest term among other eddy PV flux terms, thus the dominant term deciding the structure of the eddy PV flux. The M_{bx} is dominantly positive showing that the eddies are either carrying high PV in-shore or low PV off-shore. **(d)** M_{by}: Form drag in y. This term is smallest among other terms and thus not a major component of the eddy PV flux.

rate of decent, 0.2, where a negative maximum form drag ($M_b(y)$, Figure 2-16b) is also observed (Figure 2-9). This rate is larger than the frictional Ekman number (0.1) and it is because the overflow transferred its momentum to the upper layer through eddies. Far from the strait, where there is no significant momentum transfer from the overflow to the upper layer, the overflow descends roughly at the rate of the frictional Ekman number.

In this subsection, the eddy-driven topographic β-plume in the upper layer was shown to be driven by the form drag between the overflow layer and the upper layer. Since the dominant direction of the momentum transfer was from the overflow to the upper layer, the eddy PV flux had a negative maximum (only one sign) and thus created two regions of eddy PV flux divergence with opposite signs. The two regions of eddy PV flux divergence forced bi-directional mean flows crossing the PV gradient which then led to the formation of the double gyre topographic β-plume. The consequence of the momentum transfer from the overflow to the upper layer was the descent of the overflow at a steeper angle than the frictional Ekman number. In the next subsection, the energy balance of the overflow layer will be examined.

2.3.4 The Energy Balance

In this subsection, we will examine how energy is lost from the overflow layer as it descends the continental slope. If the overflow layer does not interact with the upper layer, the energy loss occurs solely due to bottom friction but when the overflow does interact with the upper layer, the overflow can also lose energy by the pressure work to the upper layer. First, the energy balance equation for the overflow layer is derived. This equation is then used to examine the energy balance of the overflow observed in Case 3.

The energy balance equation of the overflow layer is derived from a sum of the overflow momentum equations in x multiplied by u_2 and equations in y multiplied by v_2:

$$\frac{\partial(KE+PE)}{\partial t} + \nabla\cdot\left(KE + g'h_2(h_2-D)\right)\mathbf{u_2} = -\mathbf{U_2}\cdot\nabla p_1 - 2\nu KE, \qquad (2.34)$$

where KE is the kinetic energy defined as

$$KE = \frac{h_2}{2}(u_2^2 + v_2^2) \tag{2.35}$$

and PE is the potential energy defined as

$$PE = \frac{1}{2}g' h_2(h_2 - 2D). \tag{2.36}$$

D is the bottom topography height referenced from -3000 m. Eq 2.34 is an energy balance equation at a point. To derive a spatially integrated energy balance equation, we first take a time-mean and then integrate Eq 2.34 across slope (x direction):

$$\int_{-A}^{A} dx \nabla \cdot \overline{(KE + g' h_2(h_2 - D))\,\mathbf{u_2}} = -\int_{-A}^{A} dx \overline{h_2 \mathbf{u} \cdot \nabla p_1} - 2\nu \int_{-A}^{A} \overline{KE} dx \tag{2.37}$$

where $x = A, -A$ are where the overflow thickness vanishes (Figure 2-17a). The LHS is a sum of the divergence of kinetic energy flux and the pressure work to the overflow layer due to the interface tilt. The latter term is basically the potential energy term for the overflow layer. The RHS is a sum of form drag and dissipation, which will extract energy from the overflow layer (Figure 2-17a).

Eq 2.37 shows that the overflow loses its energy to both form drag and dissipation, and both are of the same order of magnitude about 150 km downstream from the strait (Figure 2-18). This location is also where the negative maximum eddy PV flux is located (Figure 2-16) and where a steep angle of descent is observed in the time-mean (Figure 2-9b). Since the cross isopycnal energy flux plays an equivalent role in extracting the energy of the overflow as bottom friction, the overflow descends at a rate two times larger (0.2) than the Ekman number (0.1). Further downstream from the strait, the potential energy loss is mostly by dissipation and the cross isopycnal energy flux is negligible.

By integrating Eq 2.40 in the along slope direction beginning from the strait (y=0) to a downstream location $y = \xi$, we can diagnose the integrated value of energy loss

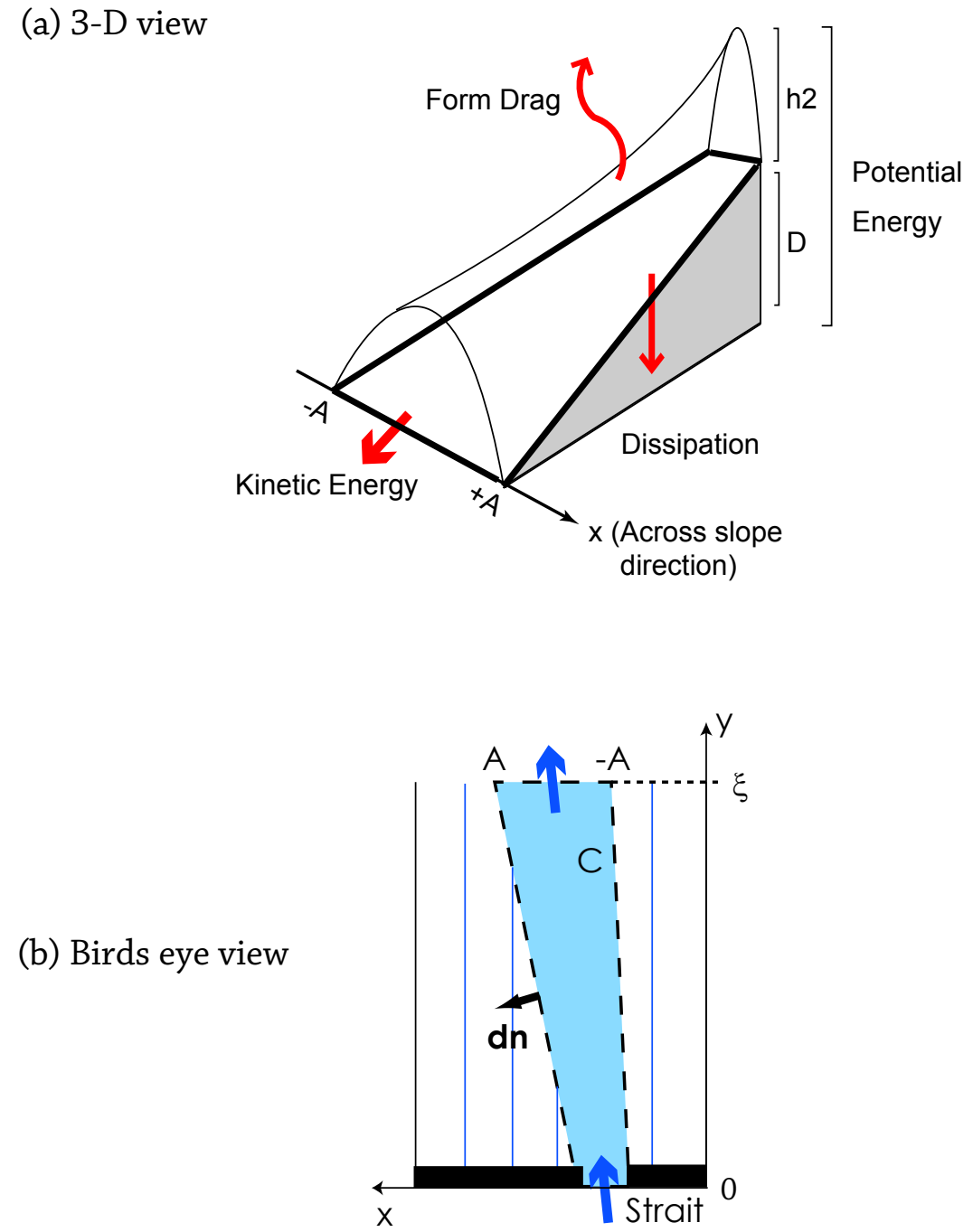

Figure 2-17: A schematic of the overflow: **(a)** 3-D: The overflow comes in the continental slope region with kinetic energy $\frac{h_2}{2}(u_2^2+v_2^2)$ and potential energy $\frac{1}{2}g'h_2(h_2-2D)$ where D is the height of the bottom topography referenced from -3000 m depth. As the overflow descends the continental slope, part of this energy is lost to form drag (to the upper layer) and dissipation. **(b)** Birds eye view: The line integral c covers the whole overflow layer. The boundary lines of the overflow layer (where its thickness goes to zero) satisfy $\mathbf{u_2} \cdot \mathbf{dn} = 0$ since there is no flow across this boundary. The only place where $\mathbf{u_2} \cdot \mathbf{dn} \neq 0$ is at the strait ($y = 0$) and at a downstream location $y = \xi$.

that the overflow experiences from the strait.

$$\int_{-A}^{A} dx \int_{strait}^{\xi} dy \nabla \cdot \overline{(KE + g' h_2(h_2 - D))\, \mathbf{u_2}} = -\int_{-A}^{A} dx \int_{sill}^{\xi} dy \left(\overline{h_2 \mathbf{u_2} \cdot \nabla p_1}\right) \quad - \quad 2\nu \int_{-A}^{A} dx \int_{sill}^{\xi} dy \overline{KE}. \quad (2.38)$$

Using Gauss's Theorem, the LHS of the equation can be rewritten as

$$\int_{c} \overline{(KE + g' h_2(h_2 - D))\, \mathbf{u_2} \cdot \mathbf{dn}} = -\int_{-A}^{A} dx \int_{sill}^{\xi} dy \left(\overline{h_2 \mathbf{u_2} \cdot \nabla p_1}\right) \quad - \quad 2\nu \int_{-A}^{A} dx \int_{sill}^{\xi} dy \overline{KE}. \quad (2.39)$$

When the line integral c is taken over the whole overflow layer (Figure 2-17b), $\mathbf{u_2} \cdot \mathbf{dn} = 0$ at $x = \pm A$ and the only place $\mathbf{u_2} \cdot \mathbf{dn} \neq 0$ is at the strait and $y = \xi$. Therefore, the line integral c term becomes the difference of the kinetic and potential energy flux between the strait and $y = \xi$:

$$\left[\int_{-A}^{A} dx \overline{(KE + g' h_2(h_2 - D))\, v_2}\right]_{strait}^{\xi} = -\int_{-A}^{A} dx \int_{sill}^{\xi} dy \left(\overline{h_2 \mathbf{u_2} \cdot \nabla p_1}\right) \quad - \quad 2\nu \int_{-A}^{A} dx \int_{sill}^{\xi} dy \overline{KE}. \quad (2.40)$$

This is the energy balance equation showing the cumulative energy loss that the overflow layer experiences while travelling distance ξ from the strait along the slope (LHS) due to form drag and dissipation (RHS).

The decrease in the total (kinetic and potential) energy of the overflow in Case 3 is mainly due to decrease in potential energy (Figure 2-19). Although the flow field is complicated, the kinetic energy does not change much. The potential energy flux decreases because of both form drag and bottom friction near the strait. But farther downstream from the strait, potential energy flux decreases roughly at a constant and the decrease is mainly due to dissipation. By 600 km downstream from the strait, the total change in potential energy flux is -7.1×10^6 kg m^{3}s^{-3}. Dissipation is responsible for the loss of -5.3×10^6 kg m^{3}s^2, which is 73% of the total energy loss and form drag

is responsible for the loss of -1.9×10^6 kg m^{3}s^2, which is the remaining 27%. The energy flux from the overflow to the upper layer is significant and plays an important role also in the total energy balance of the overflow.

The energy balance of the overflow can also be diagnosed (roughly) by examining the distance of descent just like the momentum balance. When the overflow reaches the northern wall, the maximum thickness of the overflow layer is located 100 km off-shore from the strait. If the overflow does not transfer energy to the upper layer, this descent is estimated to be about 70 km, according to the bottom friction. Thus 30% of the total descent (100 km) is because of energy transfer to the upper layer while 70% is because of bottom friction. This ratio roughly matches with the ratio of 27% estimated from the energy balance equation above. The energy loss to the upper layer is smaller but on the same order as energy loss by friction.

Thus in this section, the adiabatic interaction of the overflow and the upper layer was shown to induce a double gyre topographic β-plume in the upper layer and to increase the angle of overflow descent. The PV balance and momentum balance showed that the double gyre structure of the eddy-driven topographic β-plume occurred because the eddies fluxed momentum mostly from the overflow to the upper layer. The energy balance of the overflow layer also showed that energy loss to the upper layer by eddies resulted in a larger rate of descent of the overflow layer than by bottom friction alone. In the next section, we will revisit Case 1, the result of the overflow-upper ocean interaction when diabatic and adiabatic interaction occur at the same time.

2.4 Entrainment and Eddy-Driven Topographic β-plumes (Case 1)

The goal of this chapter is to understand the dynamics of the overflow and its overlying layer when these two layers interact through entrainment and baroclinic instability (Case 1, Table 2.1). However, the model calculation showed complicated flow fields

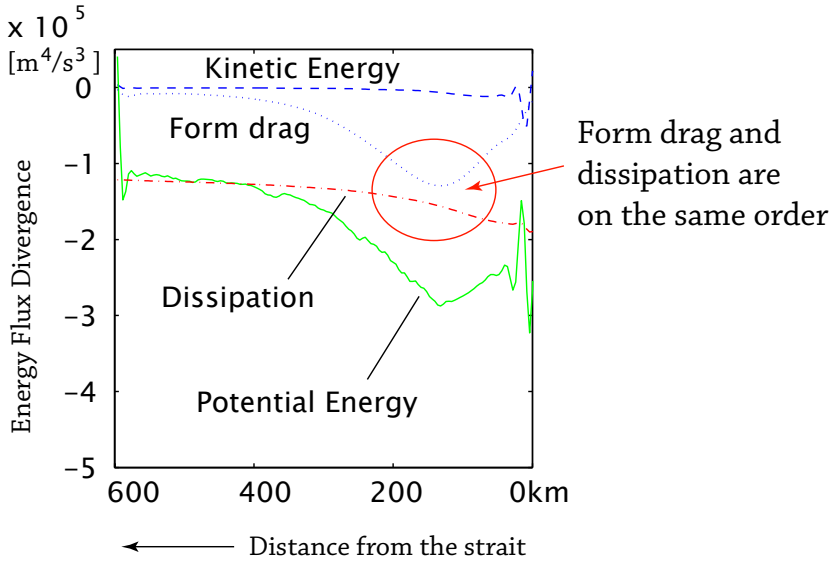

Figure 2-18: Energy balance at each cross-section (Eq 2.37): Energy loss experienced at every cross-section from the strait to the northern boundary. The energy loss is mostly due to the decrease in potential energy (solid line) not kinetic energy (dashed line). Potential Energy is lost by dissipation (dash-dotted line) and form drag (dotted line) near the strait. Form drag term shows a negative maximum about 150 km downstream from the strait but further downstream, it becomes negligible compared to bottom friction. Thus the potential energy loss is solely due to dissipation far from the strait.

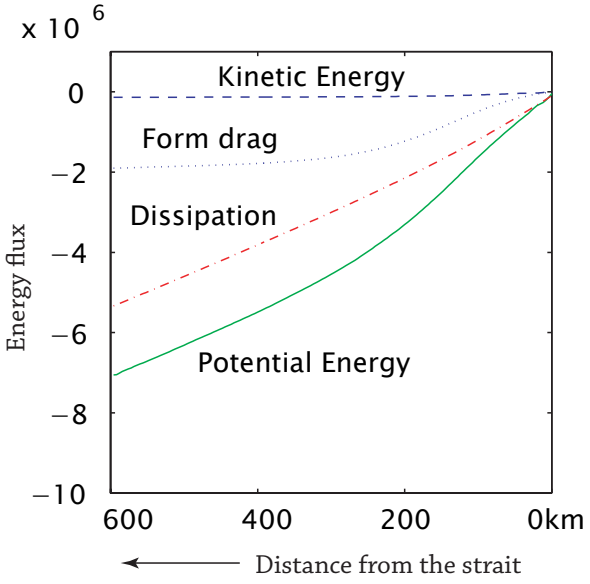

Figure 2-19: The cumulative energy loss experienced from the strait (Eq 2.40): The loss of potential energy (solid line) is balanced mainly by dissipation (dash-dotted line). The remainder is due to form drag (dotted line) which shows a sharp increase near the strait. The loss of kinetic energy (dashed line) is negligible.

in both layers when these two processes were present (Figure 2-1 and 2-20a and b). So, in order to understand the dynamics, we have examined the effect of entrainment and baroclinic instability on the two layers separately in the previous sections. In this section, we will use these previous results to revisit and try to understand the complicated flow field of Case 1.

The model used for Case 1 is a two layer model that has an overflow (1.5Sv) coming out of the strait while entraining upper ocean water (1.5Sv) near the strait. It uses all the features of the model described in Section 2.1. Compared to the model used in the previous section (Case 3, Table 2.1), this model has an addition of entrainment near the strait.

First, the final statistically steady flow field is examined. Then the role of eddies is discussed.

2.4.1 The flow field

The snapshot of the sea surface height shows eddies of both signs (Figure 2-20a). The eddies have an azimuthal velocity of 50 cm s^{-1}, radius of 50 km, and a sea surface height of $\pm$15cm. These eddies likely form because of baroclinic instability between the overflow and the upper layer as shown in Case 3 for this parameter space. The sea surface height of Case 1, qualitatively, looks similar to Case 3 where baroclinic instability occurred and the eddies created by this instability had similar characteristics (Figure 2-6a). A noticeable difference of Case 1 from Case 3 is that there are slightly more cyclonic eddies than anticyclonic eddies in Case 1. This is because on top of the eddies created by baroclinic instability (Case 3), there is also a cyclonic flow driven by entrainment.

The snapshot of the overflow layer shows the overflow layer turning into anticyclonic eddies after it exits the strait (Figure 2-20b). These anticyclonic eddies are qualitatively similar to that observed in Case 3 (Figure 2-6b), but compared to Case 3, they are thicker. This thickness increase in Case 3 is because of entrainment and the thick anticyclonic eddies are observed to flow along the continental slope over a long distance while keeping their original thickness. These anticyclonic eddies are

likely a result of vortex squeezing by entrainment. The cyclonic eddies observed in the upper layer on top of these anticyclonic eddies are likely a result of vortex stretching by entrainment. The overflow downstream from the strait is a chain of eddies rather than a stream-tube.

The time-mean of the sea surface height shows a strong cyclonic topographic β-plume of 4.1 Sv along the continental slope (Figure 2-21a) that looks similar to the entrainment-driven topographic β-plume of Case 2 (Figure 2-3a). The eddies are dominant in the snapshot but the time-mean shows that the cyclonic topographic β-plume observed in Case 2 is a more robust feature. Close to the strait, there is an anticyclonic circulation of 1.3Sv, which is not as strong as the cyclonic gyre but still as strong as the overflow transport. The mean flow field close to the strait is also a double gyre rather than a single gyre that is similar to the eddy-driven topographic β-plume of Case 3 (Figure 2-9a).

The time-mean of the overflow layer thickness shows a steep descent near the strait (Figure 2-21b). This bigger angle of descent is similar to what the overflow layer experienced in Case 3 (Figure 2-9b) where the baroclinic instability transferred overflow layer momentum and energy to the upper layer near the strait. The main thick core descends approximately with the frictional Ekman number after the steep descent near the strait but part of the layer still continues to descend with a steep angle.

2.4.2 The role of eddies

In this subsection, we will examine the role of eddies when both entrainment and baroclinic instability are present (Case 1). How has the PV balance changed from that of Case 2 or 3? Do eddies influence the transport of the topographic β-plume ?

The PV balance

The PV balance in the entrainment region of Case 1 appears to be a sum of that of Case 2 and 3 (Fig 2-22). The entrainment acts as a PV forcing ($\overline{qw^*}$) as seen in Case

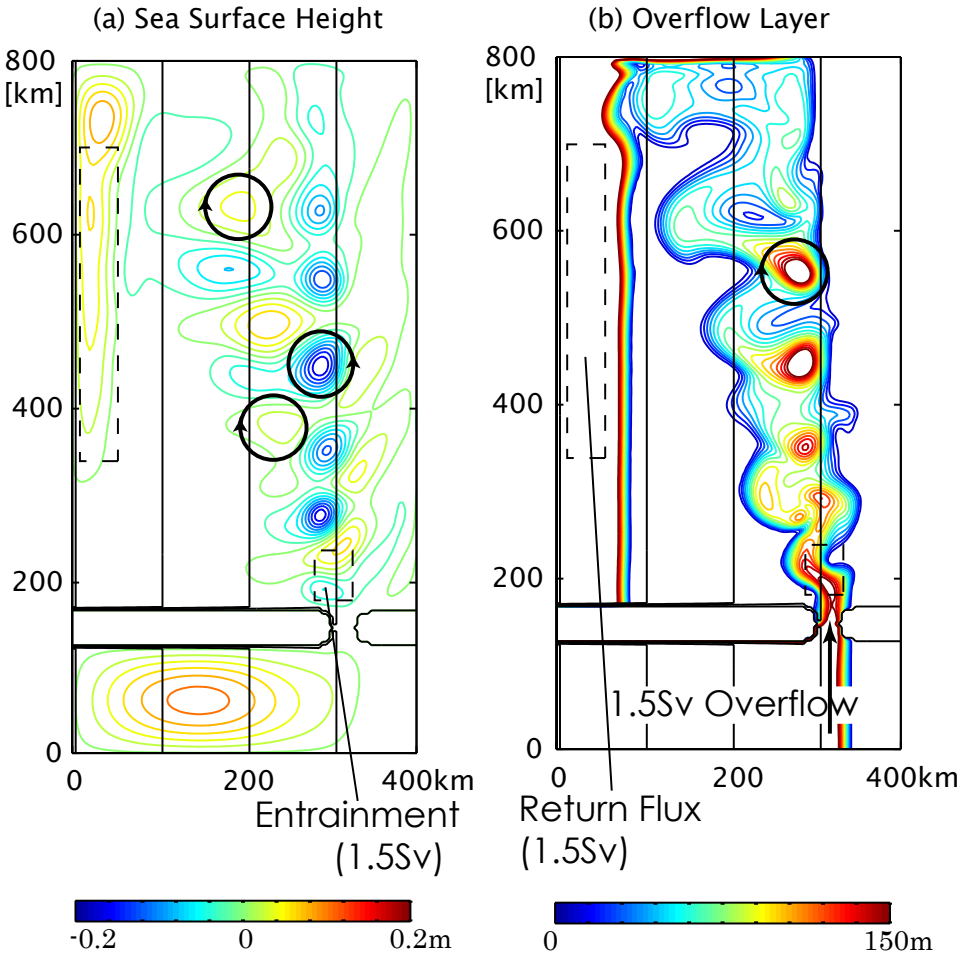

Figure 2-20: A snapshot of the two-layer model (Case 1). Same as Figure 2-1. The dotted square region is where entrainment from the upper ocean layer to the overflow layer occurs. (a) Sea Surface Height contoured between -20 and 20 cm with an interval of 2cm. Strong cyclonic and anticyclonic eddies form near the strait. It shows eddies of both signs with an azimuthal velocity as large as 50 cm s^{-1}, radius of 50 km, and a sea surface height of $\pm$15 cm (b) Overflow layer thickness contoured between 0-150 m with an interval of 10 m. The overflow splits into an eddy as soon as it exits the strait. These eddies propagate along the bathymetric contours while descending at a shallow angle.

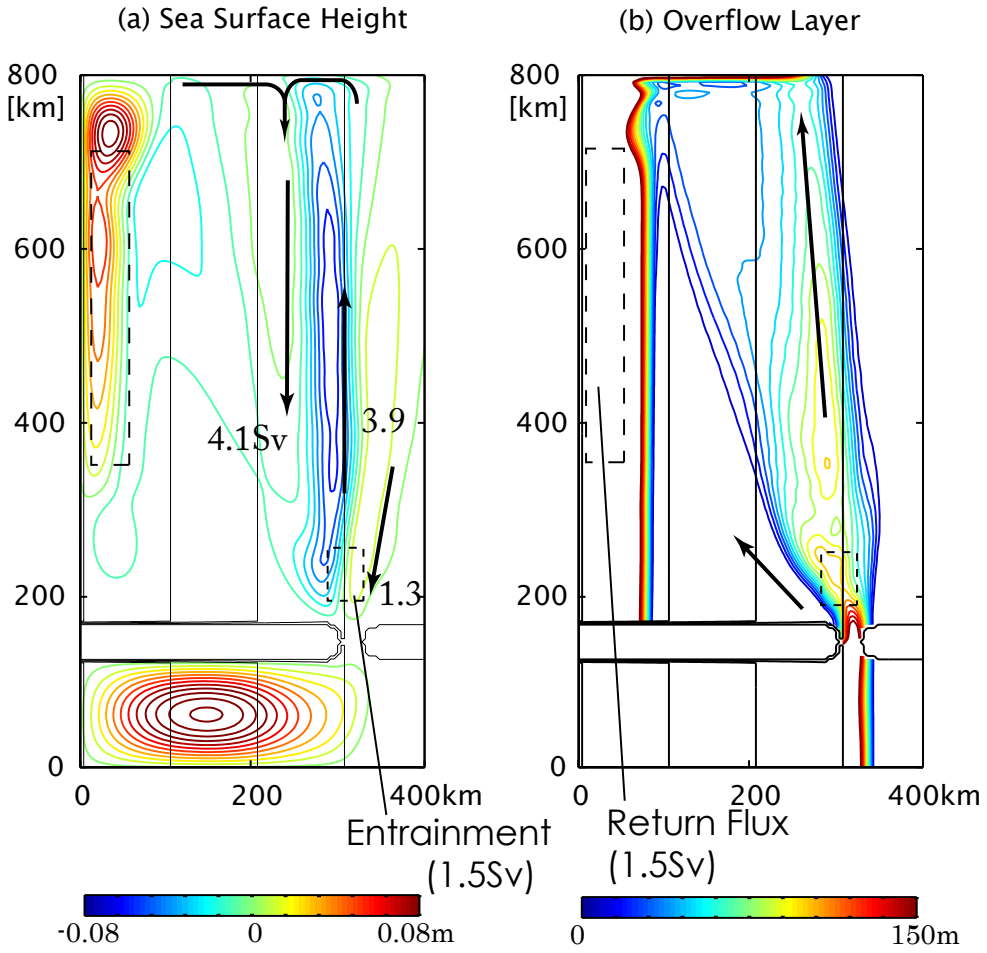

Figure 2-21: Time-mean flow field (Case 1). (a) The Sea Surface Height: A cyclonic circulation forms over much of the domain. However, there is a double gyre structure near the strait. The transport of these gyres is roughly 3.5 Sv for the off-shore jet and 1.3 Sv for the in-shore jet. Notice that the northward jet is located near the center of the entrainment region. This reflects the shift of the cyclonic topographic β-plume to the off shore side because of the eddies and the presence of an active overflow layer. (b) The overflow layer thickness: The overflow shows a steep angle of descent near the strait but weaker angle far away from the strait. However, part of the layer appears to continue to descend at a steep angle.

2. The eddies created by the baroclinic instability advect PV off-shore and create a negative and positive eddy PV flux divergence ($-\nabla \cdot \overline{\mathbf{U}'q'}$) region on the in-shore and the off-shore side of the entrainment region respectively, as seen in Case 3 (Figure 2-15). The mean PV advection term ($\mathbf{U} \cdot \nabla \overline{q}$) balances the sum of PV increase and eddy PV flux divergence so an eastward directed mean flow (a positive mean PV advection) is formed on the off-shore side of the entrainment region and a westward mean flow (a negative mean PV advection) is formed on the in-shore side (Figure 2-23).

Compared to the vorticity balance of Case 2 where the entrainment (PV forcing) is the only term forcing the mean PV advection term, the role of eddies (created by the baroclinic instability) is to move off the "effective" PV forcing region (sum of PV increase and eddy PV flux divergence) to the off-shore while leaving a negative PV forcing region to the on-shore side of the entrainment region. A double gyre topographic β-plume, which was a typical character of the eddy-driven topographic β-plume, was therefore observed in the time-mean flow field near the strait (Figure 2-21).

The transport of the cyclonic topographic β-plume

The transport of the topographic β-plume is examined while varying the diapycnal velocity strength. The location of entrainment is kept fixed. We will define the southward and off-shore branch of the topographic β-plume as the topographic β-plume transport. A similar experiment was done in Case 2 using a one-layer model but the experiment repeated here uses the two-layer model. We will test how the linear vorticity balance (Eq 1.5) compares with the topographic β-plume transport with the presence of baroclinic instability. Note that we are focusing on the parameter regime that was stable to barotropic instability (Figure 2-5) so barotropic instability is unlikely to influence the experiment.

When the diapycnal velocity is zero, the transport of the cyclonic topographic β-plume is that of Case 3 (Figure 2-24). As the diapycnal velocity increases, the transport of the cyclonic topographic β-plume also increases and approaches the

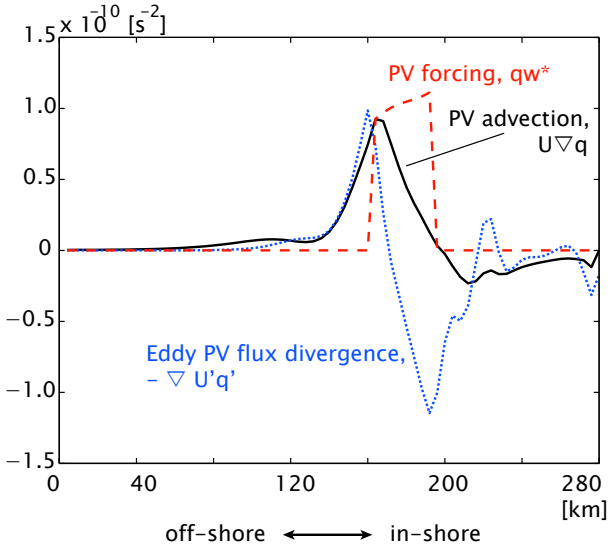

Figure 2-22: PV Balance near the entrainment region, $\overline{U} \cdot \nabla \overline{q} = \overline{qw^*} - \nabla \cdot \overline{\mathbf{U}'q'}$. The eddy PV flux divergence (blue dotted line, $\nabla \cdot \overline{\mathbf{U}'q'}$) is positive off-shore and negative on-shore. This is due to baroclinic instability (Case 3). The entrainment is a PV forcing (red dashed, $\overline{qw^*}$) and the mean PV advection (black solid line, $\overline{U} \cdot \nabla \overline{q}$) is forced by the sum of the PV increase by entrainment and the eddy PV flux divergence created by the baroclinic instability. Regions of both negative mean PV advection and positive mean PV advection exist which leads to the double gyre topographic β-plume.

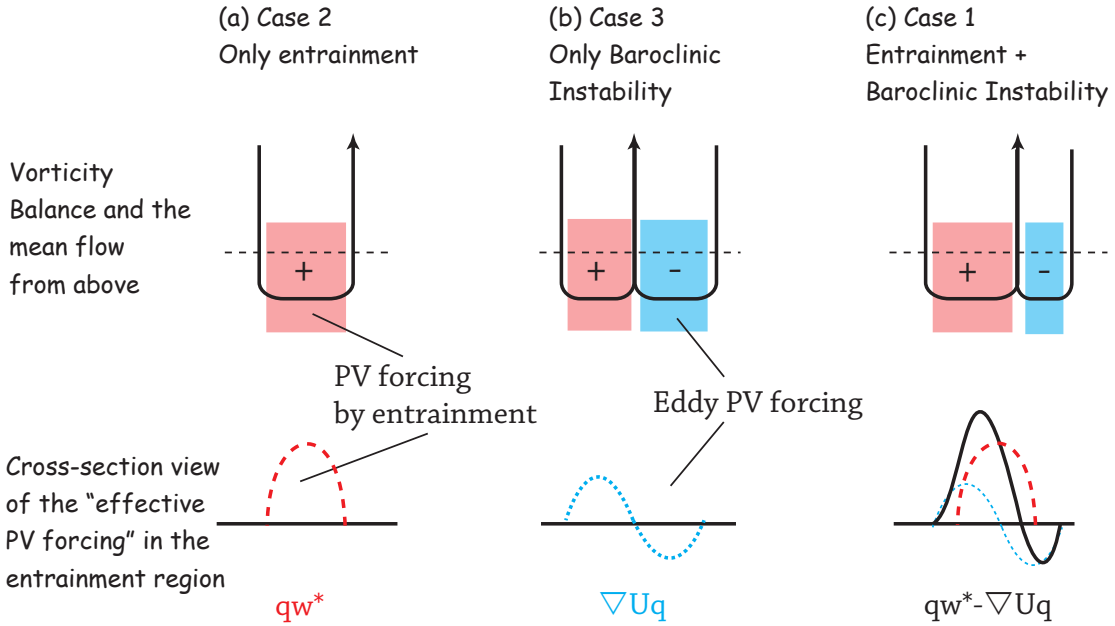

Figure 2-23: A schematic showing the difference of the PV balance near the entrainment region between Case 2, 3, and 1 as (a), (b), and (c) respectively. The top three figures show the spatial PV balance and the direction of the mean flow near the entrainment region. The bottom three figures show the cross-section view of the effective PV forcing in the entrainment region.

value estimated from the linear vorticity balance (Eq 1.5). The actual transport is 0.5-1.0Sv more than the linear estimate, but roughly speaking, the linear vorticity balance estimates the transport well. Though the eddies are strong enough to change the dominant terms of the vorticity balance and move the location of the effective PV forcing region off-shore, the transport of the topographic β-plume surprisingly remains close to the estimate derived from the linear vorticity balance. Unlike barotropic instability that decreases the transport of the topographic β-plume (Case 2, Figure 1-6), the eddies created by the baroclinic instability do not decrease the magnitude of the topographic β-plume, but rather enhance it slightly and the PV balance shows why (Figure 2-23). Though the transport of the cyclonic circulation is not a simple sum of the entrainment-driven topographic β-plume (Case 2) and the eddy-driven topographic β-plume with no entrainment (Case 3), the final transport depends on the magnitude of the total PV forcing due to eddies and entrainment. Note that the background PV gradient used in the linear vorticity balance in this two-layer model is not the same as the one-layer model of Case 2 (Figure 1-6). In the presence of the overflow layer, the upper layer PV gradient is larger so the linear vorticity balance will estimate a smaller transport than the estimate from the one layer model.

We have learned from Case 1 to 3 that the overflow is capable of driving a time-mean circulation of significant strength in the upper layer. Entrainment drives a cyclonic topographic β-plume while baroclinic instability drives a eddy-driven topographic β-plume with a double gyre. When both entrainment and baroclinic instability occur, the time-mean showed a cyclonic topographic β-plume forming over most of the continental slope region. However, the circulation near the strait was a double gyre, reflecting the dominant role of eddies in the PV balance there. The transport of the topographic β-plume was of the order of the entrainment and the linear vorticity balance (Eq 1.5) was found to give a reasonable estimate. We have also learned that the overflow-upper ocean interaction influences the overflow dynamics, by increasing the angle of descent and making the overflow layer into a chain of eddies rather than a stream-tube flow.

The experiments in this chapter were focused primarily on the parameter range

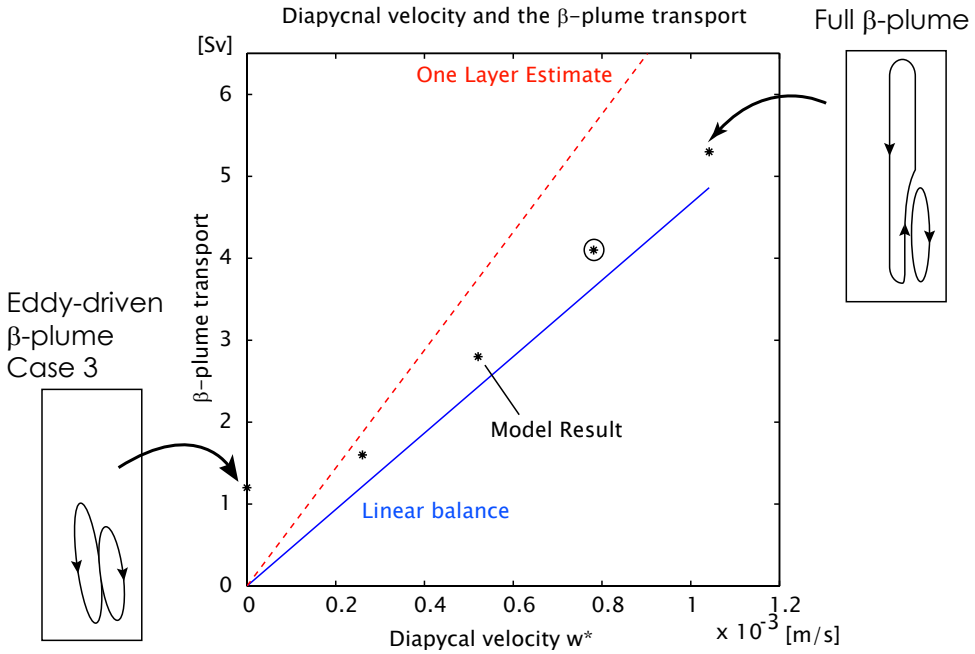

Figure 2-24: The transport of the topographic β-plume as a function of the diapycnal velocity. The topographic β-plume transport in the model (shown in asterisks) is found to increase and become closer to the estimate of Eq 1.5 (blue line). $w^* = 0$ is Case 3 and $w^* = 7.8 \times 10^{-4}$ m s^{-1} is Case 1 (shown in circle). But compared to the estimate that neglects the overflow layer (red line), the transport values show a drop in the transport as diapycnal velocity increases. The transport showed a slight increase (0.5-1.0 Sv) above the linear estimate which is likely due to eddies. However, roughly speaking, the eddies do not seem to affect the magnitude of the full topographic β-plume much.

of the Faroe Bank Channel overflow. Thus, the location and the strength of the entrainment were prescribed based on observations (Mauritzen et al., 2005). However, the two features are likely to change as the physical parameter space of the overflow change, such as overflow transport and steepness of the slope. The competition of whether entrainment driven topographic β-plume dominates or the eddy-driven topographic β-plume dominates in the continental slope region is, therefore, likely to change as the physical parameter space changes. Further investigation is needed to determine the non-dimensional parameters that predict which topographic β-plume dominates.

In the next section, we will compare the numerical results of Case 1-3 with observations.

2.5 Comparing with observations

The upper oceanic layer

The sea surface height near the Faroe Bank Channel observed from Satellite Altimetry shows the presence of eddies with fluctuation of $\pm$ 10cm and a radius of roughly 50 km (Ezer, 2006). A large standard deviation of the sea surface height was observed near the Faroe Bank Channel, about 50-100 km downstream from the strait (Figure 2-25) (Høyer et al., 2002). An area of large standard deviation of sea surface height indicates higher eddy activity than the surrounding region and this area was also limited spatially to a circular patch of about 50 km radius. A similar patch of large standard deviation of the sea surface height, was also observed downstream of the Mediterranean and Denmark Strait overflow (Høyer and Quadfasel, 2001; Høyer et al., 2002). The localized patch of high standard deviation of the sea surface height in Case 1 (Figure 2-26) is analogous to these observed results. The baroclinic instability occurring in a very localized spatial scale is the main cause for creating this feature in Case 1. Although this high standard deviation of sea surface height could be a product of other processes, similar features observed near other overflows indicate that a region of high standard deviation of sea surface height is likely a result of strong time

variability of the overflow. Baroclinic instability appears to be a plausible mechanism for creating the high standard deviation of sea surface height.

There is some evidence that a time-mean cyclonic circulation exists in the upper oceanic layer where the overflow enters the open ocean. A cyclonic circulation was shown to exist in the time-mean near the Faroe Bank Channel at 400m from sub-surface floats (Lavender et al., 2005). The cyclonic topographic β-plume seen in the upper layer in Case 1 (Figure 2-21a) is analogous to this cyclonic circulation with the magnitude of the sea surface height gradient also of the same order. However, the observed cyclonic circulation may also be a rim current of the cyclonic sub-polar gyre. The observed cyclonic circulation in the upper oceanic layer is not well known in enough resolution to compare with the numerical results in detail. Mauritzen et al. (2001) showed from tracer, hydrographic sections, and velocity measurements that a cyclonic circulation is likely to exist in the upper ocean of Gulf of Cadiz (Figure 1-8). Since this study was based on the quasi-synoptic flow field it is still premature to conclude whether the hypothesized cyclonic circulation is a robust flow field in the Gulf of Cadiz, though this study would support the existence of such a circulation. The anticyclonic topographic β-plume in Case 1 or 3 is likely to be too weak and small scale to compare with available observation data. Strong cyclonic eddies have been observed at the surface within the Gulf of Cadiz (Carton et al., 2002). They have the same magnitude of velocity and radius analogous to the cyclonic eddies observed in Case 1 but whether the cyclonic eddies outnumber the anticyclonic eddies in the Gulf of Cadiz remains unclear. The observations support, or at least do not oppose, the results of the numerical model.

The overflow layer

The temperature and velocities of the Faroe Bank Channel overflow downstream from the strait were observed to vary with a time scale of a few days. The temperature of the Mediterranean overflow fluctuated with a 7–9 day period about 200 km downstream from the Gibraltar Strait (Chérubin et al., 2003) while no such oscillations were observed at the Gibraltar Strait where the Mediterranean overflows starts its

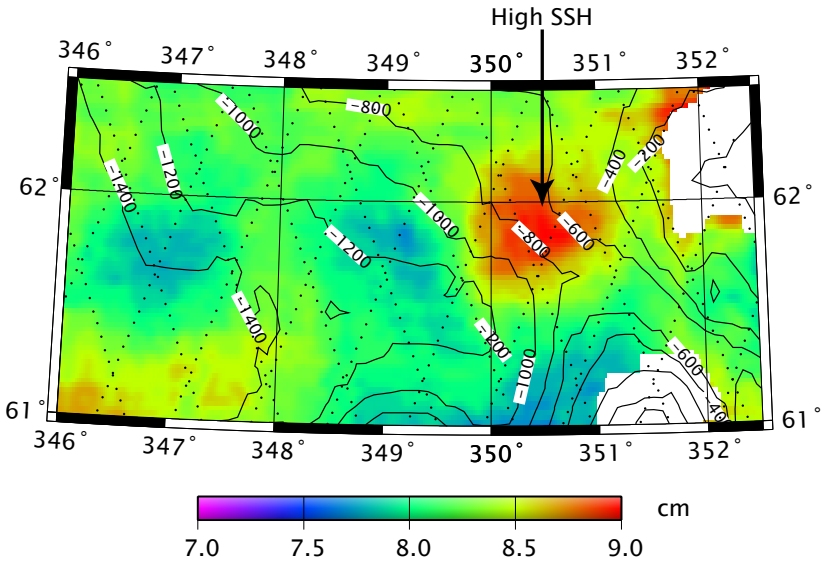

Figure 2-25: The standard deviation of Sea Surface Height (SSH) near the Faroe Bank Channel detected from Satellite Altimetry (Topex/Poseidon and ERS-1 and 2) (Høyer et al., 2002). A region of high standard deviation is noticeable where the Faroe Bank Channel overflow descends the continental slope of the North Atlantic Ocean. The patch is roughly 100 km × 100 km, exists 50 km from the strait, and is 1.0 cm higher than its surroundings. Figure reproduced by courtesy of Dr. Detlef Quadfasel.

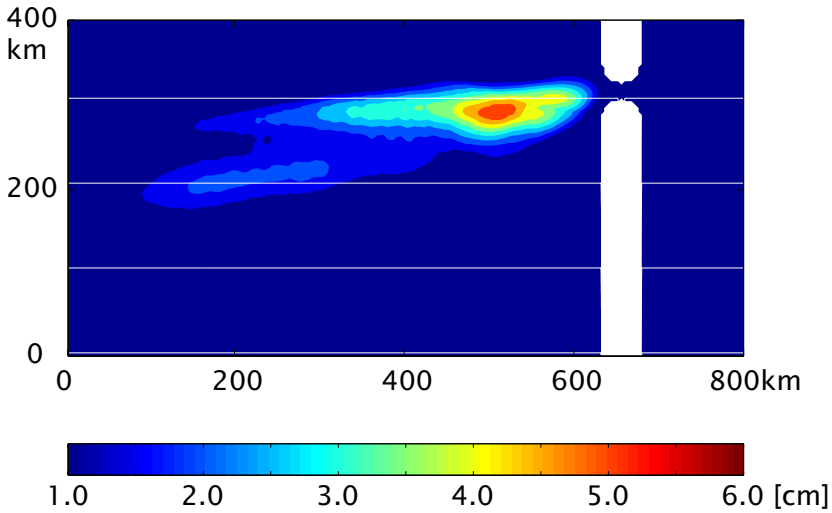

Figure 2-26: The standard deviation of Sea surface height in Case 1. A region of high standard deviation (red) is noticeable near the strait with a spatial scale of 100 km × 50 km. The standard deviation is roughly 5 cm higher in this region than its surroundings, which is larger than the magnitude observed from Satellite Altimetry (Figure 2-25).

descent (Stanton, 1983). The temperature of the Faroe Bank Channel overflow fluctuated with a 4–5 day period about 140 km downstream from the Faroe Bank Channel (Høyer et al., 2002). The transport of the Faroe Bank Channel overflow, however, was observed to change with time at the strait (Mauritzen et al., 2005) and whether this time variability at the strait is directly related to the time variability downstream is unknown. The temperature-time-series of the Faroe Bank Channel overflow 140 km downstream from the strait (Høyer and Quadfasel, 2001), showed the temperature fluctuating as large as 4 degrees which is comparable to the temperature difference of the Faroe Bank Channel source water and its ambient North Atlantic water. Their temperature-time-series across the overflow also revealed that the observed fluctuation of temperature is because the Faroe Bank Channel overflow is a chain of eddies flowing along the bathymetry rather than a stream-tube flow (Figure 2-27).

The time variability observed in the overflow and the upper ocean layer in Case 1 is analogous to the time variability observed in the Faroe Bank Channel overflow. The layer thickness-time-series across the overflow in Case 1, 140km downstream from the strait, shows a fluctuation of 4–5 day period as well as the large fluctuation ($\pm$ 50m) that is of the order of the overflow layer thickness (Figure 2-7). [1] The time series of the overflow layer thickness (Figure 2-7) is also analogous to the temperature-time-series of the Faroe Bank Channel overflow (Figure 2-27). When the numerical model is set to a parameter space close to that of the Mediterranean overflow, the time-series of the velocity about 200 km downstream from the strait showed a fluctuation of 7–8 day period, similar to what is observed (Chérubin et al., 2003). The longer period of time variability observed for the Mediterranean appears to be due to slower growth of the instability and the large spatial scale between eddies due to a decrease in f ($8.5\times\ 10^{-5*}$ s^{-1}) similar to what is observed in Figure 2-10c. Baroclinic instability, the main mechanism for creating the eddies in Case 1 or 3, is a plausible mechanism that can explain the formation of eddies and the observed time variability in the Mediterranean or Faroe Bank Channel overflow downstream from the sill.

[1] Since the parameter space used in Case 1 was closer to that of the Faroe Bank Channel overflow, the oscillation observed in the model also matches better with that of the Faroe Bank Channel overflow than the Mediterranean overflow.

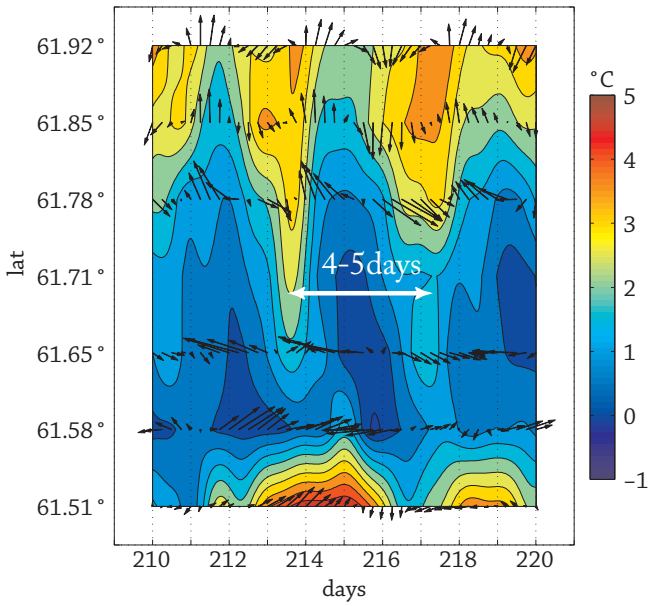

Figure 2-27: Time-latitude plot of the near bottom temperatures (contoured) and band-passed (2-8 days) currents (arrows) of the Faroe Bank Channel overflow observed about 140 km downstream from the Faroe Bank Channel (Høyer and Quadfasel, 2001). The temperature fluctuates with 4-5 day frequency and shows an eddy passing by. The maximum velocities are about -30 cm s^{-1}. Figure reproduced by courtesy of Dr. Detlef Quadfasel.

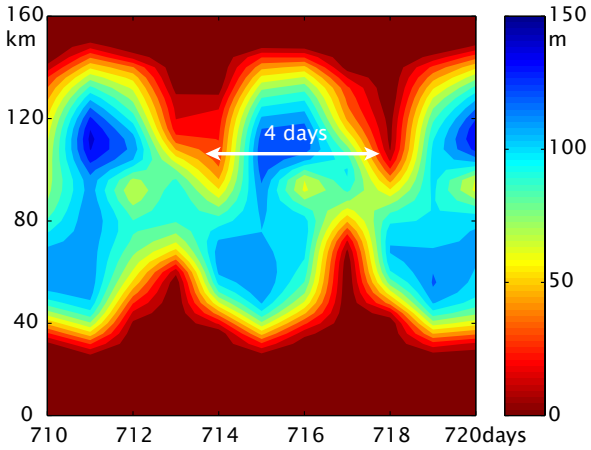

Figure 2-28: Time-latitude plot of the near bottom layer thickness of Case 1 observed 140 km downstream from the strait. The thickness fluctuates with 4-5 day frequency and shows eddy passing by. This feature is analogous to what is observed downstream of the Faroe Bank Channel (Figure 2-27). The region between the two white dotted lines corresponds to the size of the observation. Although thickness and temperature is not the same, we expect that the qualitative feature of the fluctuation between the two properties will be similar.

2.6 Summary

In this chapter, we have investigated the overflow-upper ocean interaction on the scale of the continental slope. The dynamical influence of the interaction on the overflow and upper ocean layers can be summarized as follows:

1. Entrainment drives a topographic β-plume, a strong cyclonic circulation, in the upper layer along bathymetric contours (geostrophic contours). The transport of this circulation is of the same order as entrainment and the linear vorticity balance gives a reasonable estimate of this transport.

2. Baroclinic instability develops and creates eddies in both overflow and upper ocean layers. The snapshot of the flow field in the two layers is dominated by these eddies. Although for our choice of inflow and entrainment parameters, the presence of eddies only slightly enhances the transport of the topographic β-plume, the PV balance near the entrainment changes from the linear vorticity balance to turbulent Sverdrup balance. Thus, the structure of the time-mean circulation shows the character of the eddy-driven topographic β-plume (cyclonic and anticyclonic gyres off-shore and in-shore, respectively) rather than an entrainment-driven topographic β-plume (single gyre).

3. Baroclinic instability also transfers a significant portion of overflow momentum and energy to the upper layer. The overflow layer thus loses more energy than just due to bottom friction. Thus, the overflow descends at a steeper angle than the estimate from the frictional Ekman number.

One outstanding question remaining is to determine the magnitude the eddy-driven topographic β-plume. Though the model calculations indicate sensitivity not only to the strength of the instability, but to other parameters of overflow and the upper layer, a non-dimensional number that can determine the transport of the eddy-driven topographic β-plume as well as how it can compete with the entrainment-driven topographic β-plume will become an important source of information if we are to estimate which of these processes are likely to be observed in the real ocean.

The next chapter will extend this investigation of the overflow-upper ocean interaction in the continental slope region to the open ocean. Whether the overflow-upper ocean interaction can influence the dynamics on the planetary scale is discussed.

Chapter 3

The impact of the Mediterranean overflow on the upper Atlantic Ocean

Can an overflow drive a basin scale circulation in the upper oceanic layer? The previous chapter examined the overflow-upper ocean interaction on the scale of the continental slope and the upper ocean was found to form a topographic β-plume along the continental slope. In this chapter, we will examine whether this topographic β-plume can become a basin scale flow and we will focus specifically on the topographic β-plume driven by the Mediterranean overflow. The object is to test whether the Azores Current in the Northern Atlantic Ocean is part of the topographic β-plume driven by the Mediterranean overflow, the hypothesis put forward in Chapter 1. The basin scale influence of the topographic β-plume induced by other overflows will be discussed in the next chapter.

When a two-layer numerical model, representing the Mediterranean overflow and its overlying ocean layer, is solved with a realistic bathymetry of the continental slope (Smith and Sandwell, 1997) along the eastern boundary of the Atlantic Ocean (Figure 3-1), the upper layer establishes an eastward zonal current in the middle of the Atlantic Ocean (Figure 3-2). This eastward zonal current is located between 34–36^o N and has a transport of 4.0 Sv, an analog of the Azores Current (Klein and

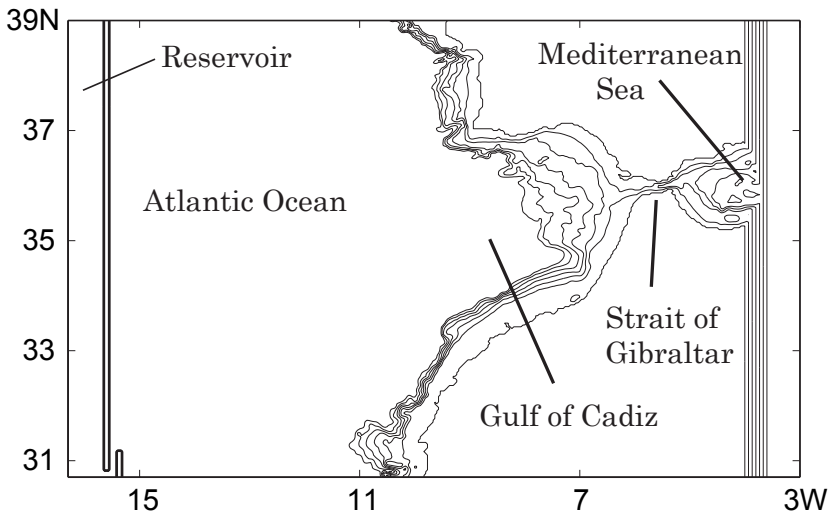

Figure 3-1: The bottom bathymetry near the Gulf of Cadiz using four-point averaged Smith and Sandwell (1997) two minute bottom bathymetry. The sea-mounts in the open ocean have been taken out to isolate the role of continental slope and the maximum depth is 2000 m. The contours are drawn from 0 to 1800m every 300 m. A reservoir exists at the western end of the model domain and is connected to the Atlantic Ocean at the southwest corner.

Siedler, 1989). A westward countercurrent also forms to the north with a transport of 2.0 Sv, an analog, perhaps, of the Azores Countercurrent (Onken, 1993). These two zonal flows in the Atlantic Ocean appear to be a planetary-scale extension of the topographic β-plume driven by the Mediterranean overflow. The model used here is basically the same as used in Case 1 (Table 2.1) other than the bottom bathymetry and the existence of the Atlantic Ocean region. Entrainment of 2.0 Sv is specified to occur on the continental slope near the Strait of Gibraltar [1] and a return flux is located in the reservoir at the western boundary that is connected to the open ocean at the south-west corner. The location of this opening does not appear to affect the two zonal jets in the open ocean. These mass fluxes are the only external forcing applied to the upper layer in the model. This experiment, hereafter Case 4, shows that the Mediterranean overflow is indeed capable of driving a circulation in the upper ocean on a basin scale. The hypothesis raised in Chapter 1 appears plausible.

The experiment of Case 4, leads to more specific questions: What is the under-

[1]The location and intensity of this entrainment is based on Baringer and Price (1997).

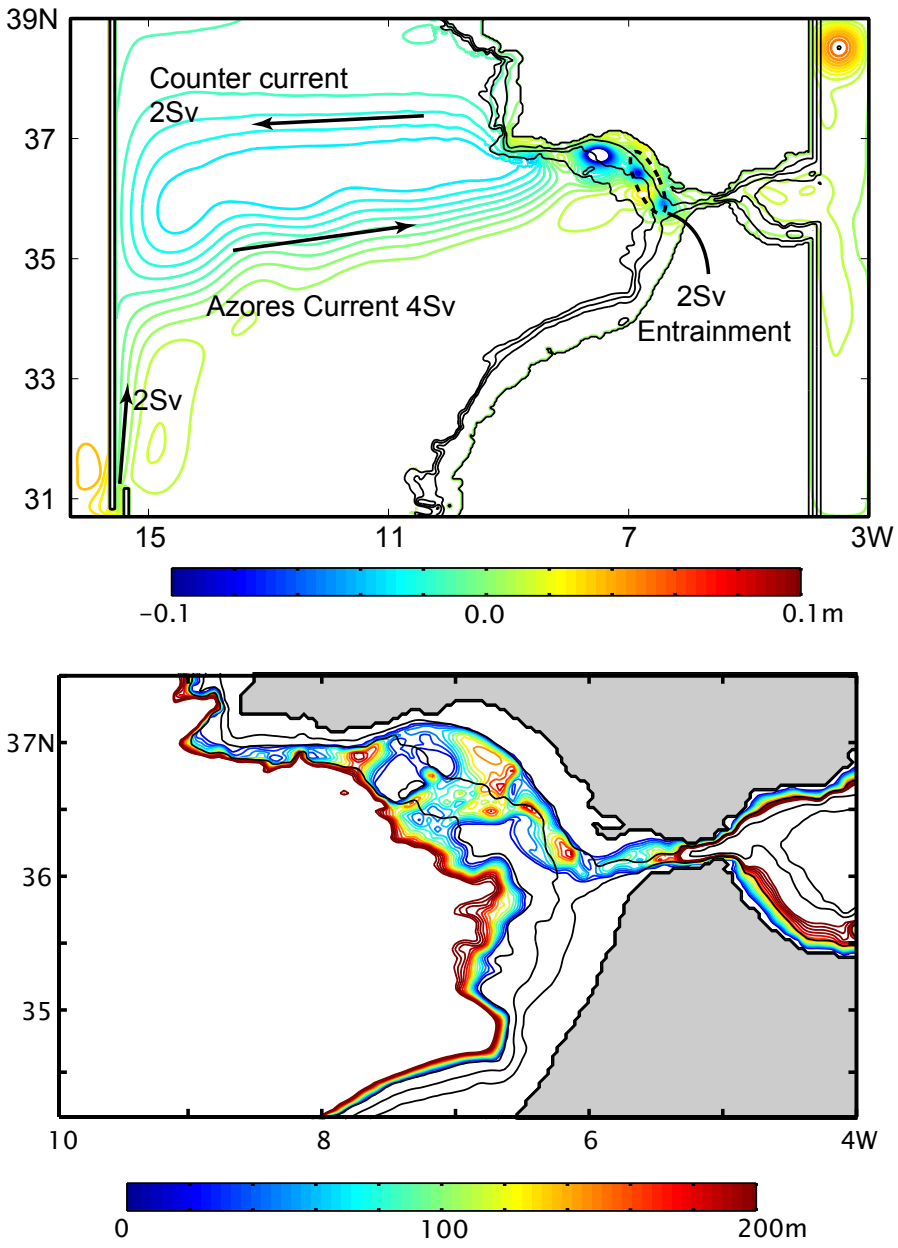

Figure 3-2: Case 4: A two-layer numerical model solved with a realistic bathymetry of the continental slope (Figure 3-1). Bottom bathymetry is contoured with black solid lines from 0 to 900 m depth every 300 m, where the upper layer is capable of directly contacting the bottom. Entrainment of 2.0 Sv is prescribed to occur within the dotted region near the Strait of Gibraltar. **(a)** A snapshot of the sea surface height contoured in color from -10 to 10 cm every 0.5 cm. An eastward zonal flow, an analog of the Azores Current, forms between 34–36^o N with a transport of 4.0 Sv. A westward zonal flow, an analog of the Azores Counter Current, also forms between 36–38^o N with a transport of 2.0 Sv. **(b)** A snapshot of the overflow layer thickness in the Gulf of Cadiz contoured in color from 0 to 200 m every 10 m. The overflow appears to broaden as it descends the slope. Anticyclonic eddies are also observed.

Case	4	5	6	7
Number of Layers	2	2	2	2
Entrainment	2.0 Sv	2.0 Sv	2.0 Sv	2.0 Sv
Overflow at the strait	1.0 Sv	1.0 Sv	1.0 Sv	1.0 Sv
Maximum slope		0.01	0.01	0.04
Topographic Character	Smith and Sandwell (1997)	Straight (α=0.01)	Curved (α=0.01)	Increases from 0.01 to 0.04
Planetary β (Open Ocean)	Yes	Yes	Yes	Yes
Region of primary focus	Mediterranean	Mediterranean	Mediterranean	Mediterranean

Table 3.1: Comparison of the model for Cases 4 to 7

lying dynamics that makes the topographic β-plume connect to the open ocean and establish the Azores Current? How are the location and width of the Azores Current determined? These are the main questions tackled in this chapter, which is organized in four sections. First, by using a model with an idealized bottom bathymetry, we will identify the feature of the continental slope bathymetry (Figure 3-1) that enables the topographic β-plume to connect to the open ocean and establish the zonal jets in the interior. A region of steep slope will be shown to play an important role. Second, we will investigate why a region of steep slope plays a crucial role. Third, by using a three-layer model, we will test whether the results of the two-layer process models are robust by testing the model in the presence of stratification. Last, the results will be compared against observations and GCM calculations.

3.1 The topographic β-plume and the open ocean

The bottom bathymetry of the Gulf of Cadiz (Figure 3-1) is complicated, but to the north of Gibraltar Strait, we recognize three major components: (1) the slope is located on the eastern boundary of the Atlantic and (2) the slope curves and (3) changes from gentle slope near the Gibraltar Strait to steep slope near the coast of Portugal. In this section, we will identify which of these three components is playing an important role in the formation of the "Azores Current" in Figure 3-2.

3.1.1 Constant slope along the eastern boundary: Case 5

The simplest bottom bathymetry that represents the continental slope of Europe and Africa along the Atlantic Ocean (Figure 3-1) is a constant slope (here we use 0.01) on the eastern boundary (Figure 3-3). We will first test whether the formation of a zonal jet is possible with this bottom bathymetry. In this experiment, hereafter Case 5, we are basically testing whether the topographic β-plume can connect to the open ocean simply because of the fact that it is located at the eastern boundary and not because of any detailed feature that exists in the real continental slope.

The model

The parameter space of this model (Figure 3-3) is close to that of the Mediterranean overflow (Bryden and Stommel, 1984; Price et al., 1993). A marginal sea is connected to the continental slope region at the south with a strait 16 km wide and 300 m deep. An overflow comes out from the marginal sea through this strait with a transport of 1.0 Sv and then slides down the continental slope while entraining 2.0 Sv from the upper layer. This entrainment is prescribed and occurs in a specified region near the strait: 20–60 km from the strait in the along slope direction and between the topographic depth of 300–600 m, with a constant diapycnal velocity (w^*) of 2.1×10^{-3} m s^{-1}. In reality, the location of this entrainment depends on the dynamics and the slope but here, we will prescribe the process based on Baringer and Price (1997). Notice that the model along the continental slope region is similar to that of the model used in the previous chapter (Figure 2-2). The major differences are

1. The domain is 600×600 km and has an open ocean region with a maximum depth of 2000 m.

2. The interface between the Mediterranean overflow layer and its overlying oceanic layer is roughly 900 m in the open ocean. Thus, the overflow will stop its descent and join the open ocean water when it reaches 900 m depth. This interface depth is roughly the depth where the Mediterranean overflow is known to become neutrally buoyant (Ambar and Howe, 1979a).

3. The model is on a β-plane. The background PV gradient in the open ocean region increases to the north, the positive y direction, with a planetary β of 2×10^{-11} m^{-1} s^{-1}. However, the background PV gradient in the continental slope region is still controlled dominantly by the topographic β.

4. A mass flux of 2.0 Sv is forced from the overflow layer to the upper oceanic layer in the reservoir. This mass flux balances the entrainment near the strait (2.0 Sv) so that each layer will conserve mass. The return flux is located outside the open ocean region so that there is no external forcing in the open ocean region.

5. Laplacian viscosity is used along with bottom friction and biharmonic viscosity for friction. The viscosity coefficient (A_H) is set to 10 m^2 s^{-1}. But within 50 km from the western wall, the viscosity coefficient increases exponentially to 1000 m^2 s^{-1}. A_H is increased near the western boundary so that the strength of the inertial overshoot is reduced at the western boundary. Without this enhanced viscosity, a large inertial gyre develops along the southern boundary from west to east (Veronis, 1966) and disrupts the interior flow field in the model. One can avoid this by increasing the meridional length of the model so that the inertial overshoot does not encounter the southern boundary. However, this was not computationally affordable so we chose to dampen the inertial gyre by enhancing A_H at the western boundary.

The rest of the model (e.g., Basic equation, bottom friction, strait width) is the same as the one used in the previous chapter (see Section 2.1).

The flow field

The snapshot of the sea surface height shows cyclonic and anticyclonic eddies trapped within the continental slope region (Figure 3-4a). Cyclonic eddies have a sea surface height of -20 cm, a radius of 50 km, and an azimuthal velocity of 10 cm s^{-1}. They outnumber the anticyclones that are weaker and form mostly on the in-shore part of the continental slope. The overflow layer gradually descends the slope while also creating anticyclonic eddies (Figure 3-4b). The dynamical behavior of the upper and overflow layers in the continental slope region appears to be similar to what we observed in Case 1 (Table 3.1) where the model does not have planetary β and the open ocean region.

The time average flow field in the continental slope is also similar to that of Case 1. The sea surface height shows a formation of a double β-plume near the strait with a cyclonic gyre of 2.1 Sv in transport and an anticyclonic gyre of 0.1 Sv (Figure 3-4c). Since this experiment (Case 5) has $\mu = 0.7$, which is smaller compared to Case 1 (μ=0.95, see Section 2.3.2 for details), the baroclinic instability between the two layers are likely to be less intensive. The decrease in μ is primarily due to a decrease

(a) Schematic of the model setup for Case 1

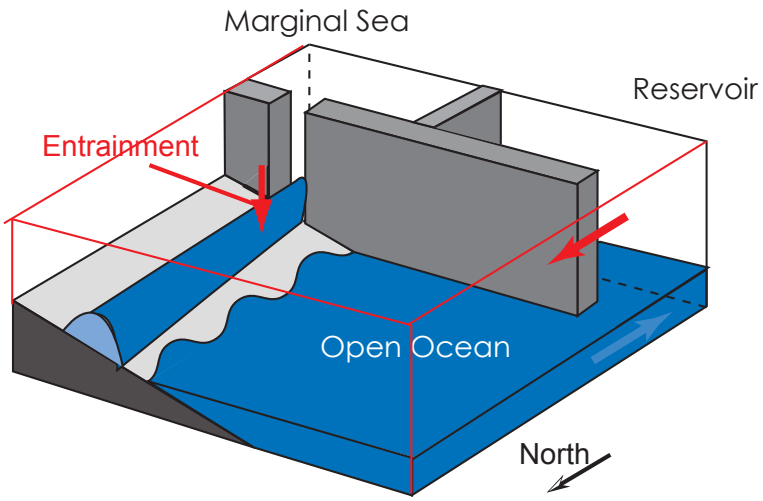

(b) Birds Eye View

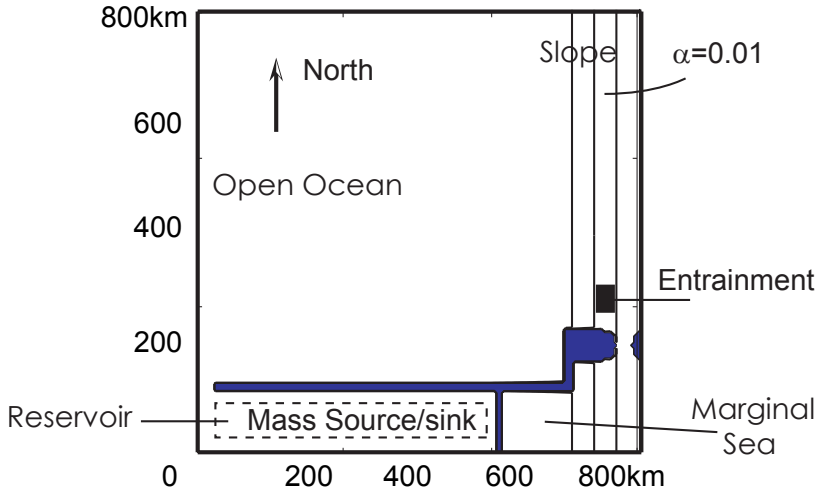

Figure 3-3: **(a)** A schematic of the model for Case 5. **(b)** The birds-eye view of the model. The continental slope region exists to the east of the open ocean with a constant slope. The bathymetric contours are drawn between 0 to 900 m every 300 m, where the upper layer can directly contact the bottom bathymetry. The maximum depth of the basin is 2000 m. The interface between the upper and overflow layer is 900 m in the open ocean. Entrainment of 2.0 Sv is located near the strait between 300–600 m depth and 20–80 km from the strait. A return flux of 2.0 Sv from the overflow layer to the upper oceanic layer exists in the reservoir to balance mass within each layer. Note that the interface intersects with the bottom at a much closer location than Case 1 (Table 2.1) because the interface moved from -3000m to -900m.

in the layer thickness (less transport) and Coriolis parameter compared to Case 1. This may be why the double gyre structure of the eddy-driven topographic β-plume near the strait is less prominent and weaker than Case 1 (Figure 2-21a).

The overflow layer descends at a steeper angle than the frictional Ekman number near the strait, but further downstream from the strait the overflow layer descends roughly with the frictional Ekman number while part of the layer also leaks and descends at a steeper angle (Figure 3-4d).

In the open ocean, the snapshot and the time average of the sea surface height both show a similar flow field (Figure 3-4a and c). The cyclonic circulation forming at the northern boundary of the open ocean is an extension of the topographic β-plume into the open ocean region due to inertial overshoot at the northern boundary. The anticyclonic circulation south of the cyclonic circulation is possibly a viscous gyre that supports the mass transport from the reservoir into the slope region. In the absence of the inertia overshoot of the topographic β-plume, this anticyclonic gyre will be along the northern boundary forming a northern boundary layer flow to the east. These two gyres that form in the northern boundary of this model will exist unless the model domain is made extremely large meridionally, say 2000km, so that the background PV contours (geostrophic contours) in the continental slope region are directly connected to the open ocean region. The meridional length scale (l) required to balance the PV difference between the entrainment region and the open ocean is $l = \frac{\beta^*}{\beta} m$, where m is the distance between the two regions, is estimated to be about 1500 km. If the northern boundary is located further than this distance, then the topographic β-plume can directly connect to the open ocean.

The strong eastward zonal jet observed in Case 4 does not form in this experiment (Case 5). The topographic β-plume is mostly trapped within the continental slope region and the transport of the eastward zonal jet in the open ocean is very weak. The experiment shows that the Azores Current will not form just because of the fact that the Mediterranean overflow is located on the continental slope at the eastern boundary of the Atlantic Ocean. Evidently, some other feature of the bottom bathymetry or something else must be connecting the topographic β-plume to the open ocean.

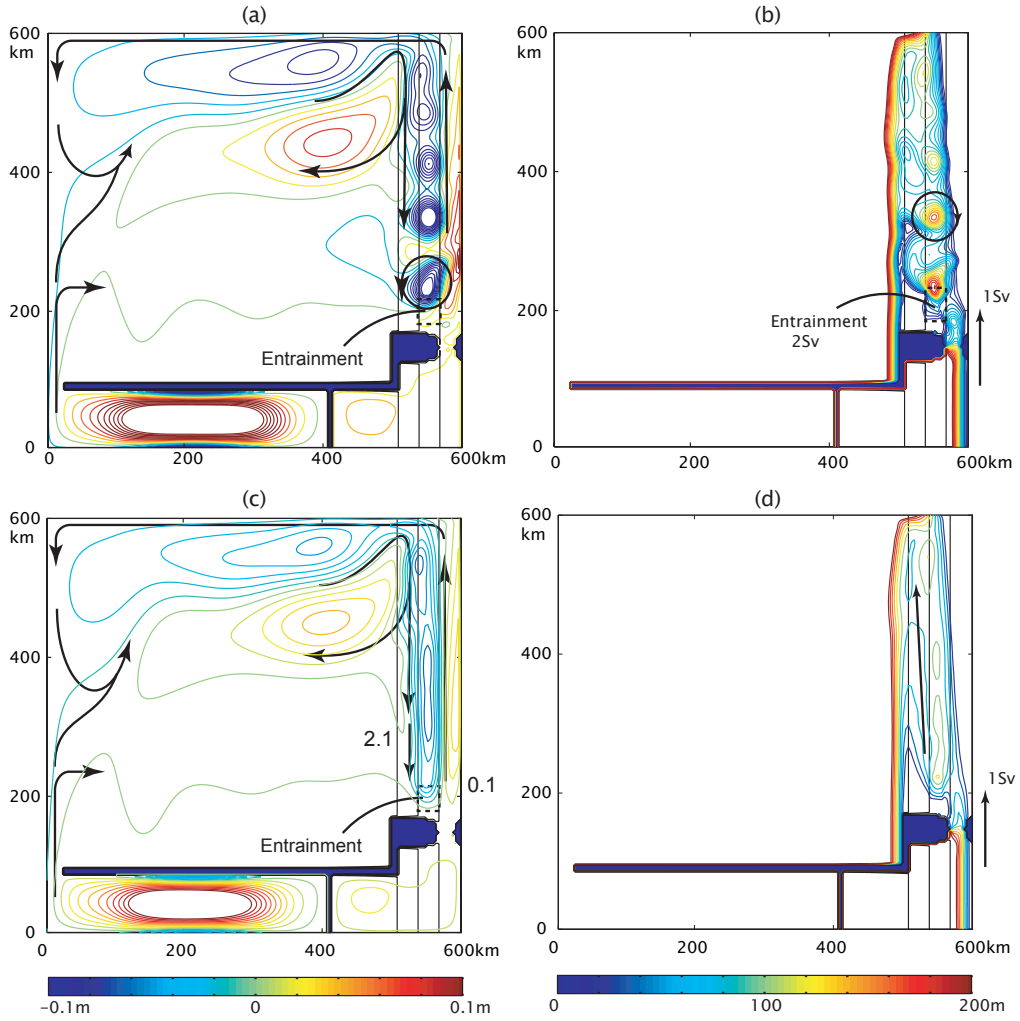

Figure 3-4: Case 5, where the overflow exists on a constant slope located to the east of the open ocean. Bathymetric contours are drawn from 0 to 900 m depths every 300 m, where the upper layer can directly contact the bottom. **(a)** A snapshot of the sea surface height contoured from -10 to 10 cm every 1 cm. Cyclonic eddies form in the continental slope region, similar to that of Figure 2-1a. **(b)** A snapshot of the overflow layer thickness contoured from 0 to 200 m every 10 m. The overflow descends the slope while also forming anticyclonic eddies. **(c)** The time average sea surface height contoured the same way as (a). The topographic β-plume forms along the continental slope with strong cyclonic (2.1 Sv) and weak anticyclonic (0.1 Sv) gyres. The cyclonic gyre extends into the open ocean because of the inertial overshoot at the northern boundary. **(d)** The time-mean overflow layer thickness contoured the same way as (c). The overflow increases its thickness near the strait because of entrainment and also gradually descends the slope.

3.1.2 Curvature of the slope: Case 6

In this subsection, we will test whether a curvature in the continental slope can make the topographic β-plume connect to the open ocean. In this experiment, hereafter Case 6, we are testing whether the inertia of the flow is strong enough for the topographic β-plume to cross the bathymetry contours while experiencing a curvature.

The model

A curvature is added to the bottom bathymetry with a spatial scale of 100 km, the scale of the Gulf of Cadiz (Figure 3-3, Case 6). The maximum slope remains 0.01, a constant, so the only difference of the bottom bathymetry between Case 5 and 6 is the curvature. The location of entrainment, as well as other parts of the model, are exactly the same as Case 5.

The flow field

The snapshot (Figure 3-6a) and the time-mean (Figure 3-6c) of the sea surface height both show qualitatively the same flow field as in Case 5 (Figure 3-4a and c). The eddies and the topographic β-plume are trapped in the continental slope region. If the inertia of the flow were strong so that $\frac{u^2/r}{fu}$ $(= R_o)$ is of order one, where R_o is the Rossby number, a curvature in the bottom slope may allow a flow across the bathymetric contours (Klinger, 1994) and make the topographic β-plume connect to the open ocean. But since the mean flow is about 0.1 m s^{-1} and the length-scale of the curvature is about 100 km, R_o is 0.01 so it is unlikely that the inertia will allow the flow to cross the bathymetric contours. (Even when using the eddy maximum velocity 0.3 m s^{-1}, R_o is still two orders smaller than one.) Unless the flow is of order 1 m s^{-1} or the length-scale of the curvature is of order few kilometers, the topographic β-plume is likely to be trapped within the continental slope region.

The snapshot (Figure 3-6b) and the time mean (Figure 3-6d) of the overflow layer thickness also show qualitatively the same flow field as in Case 5 (Figure 3-4b and d). The overflow layer descends the slope with a steep angle near the strait and then

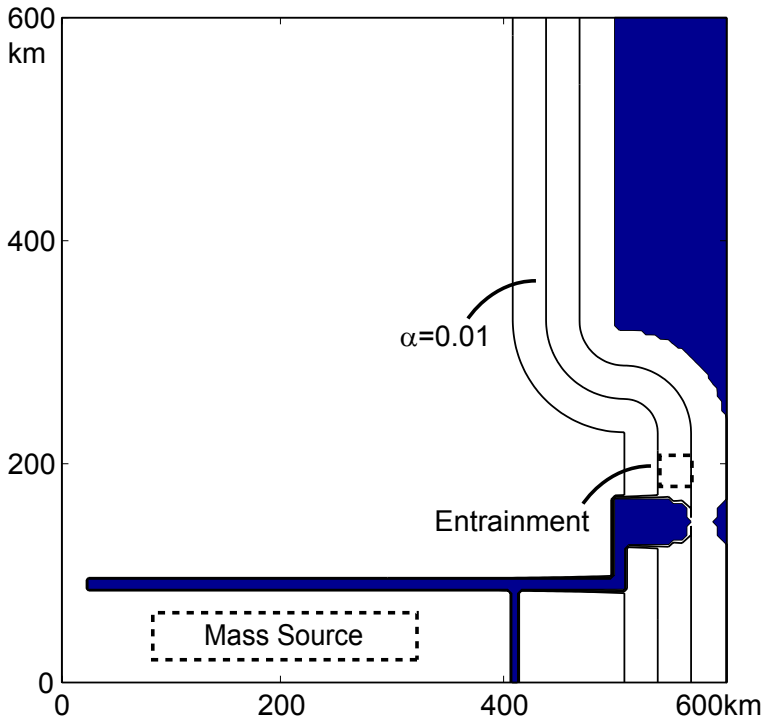

Figure 3-5: The bottom bathymetry for Case 6 where a curvature is added to the slope of Case 5 (Figure 3-3). The slope is kept to 0.01, a constant and the spatial scale of the curvature is 100 km and is close to that of the curvature between the Gibraltar Strait and the steep slope region near Cape St. Vincent. Other parts of the model are the same as Case 5.

descends gradually according to the frictional Ekman number further downstream. Part of the layer, however, appears to leak and descends at a steeper angle.

Thus, the curvature of the slope in Case 6 appears incapable of making the topographic β-plume flow across bathymetric contours and connect to the open ocean such that zonal jets establish in the open ocean.

3.1.3 Varying slope: Case 7

Next, we will test whether the change in slope, from gentle to steep, can make the topographic β-plume connect to the open ocean and establish an eastward zonal jet in the open ocean.

The model

A region of steep slope is added while keeping the coastline straight (Figure 3-7). The slope changes from 0.01 to 0.04 within 200 km from the strait, which is the length scale of the slope change from the Strait of Gibraltar to Cape St. Vincent. The slope of 0.04 is estimated from the steep slope region near Cape St. Vincent (Figure 3-1). There is a curvature in the slope, an inevitable effect when the slope changes, but since the spatial scale of this curvature is similar to that of Case 6, the topographic β-plume is expected not to be affected strongly by the curvature. The location of entrainment as well as other parts of the model are exactly the same as Case 5 and 6.

The flow field

In the open ocean region, an eastward zonal jet formed in the interior, both in the snapshot (Figure 3-8a) and the time-mean (Figure 3-8c) of the sea surface height. This eastward zonal jet has a transport of 4.0 Sv with a width of 100 km, analogous to the Azores Current and the eastward zonal jet in Case 4. A westward flow also forms along the northern boundary with a transport of 2.0 Sv with a width of 200 km, which is broader than the eastward zonal jet. The presence of the steep slope appears

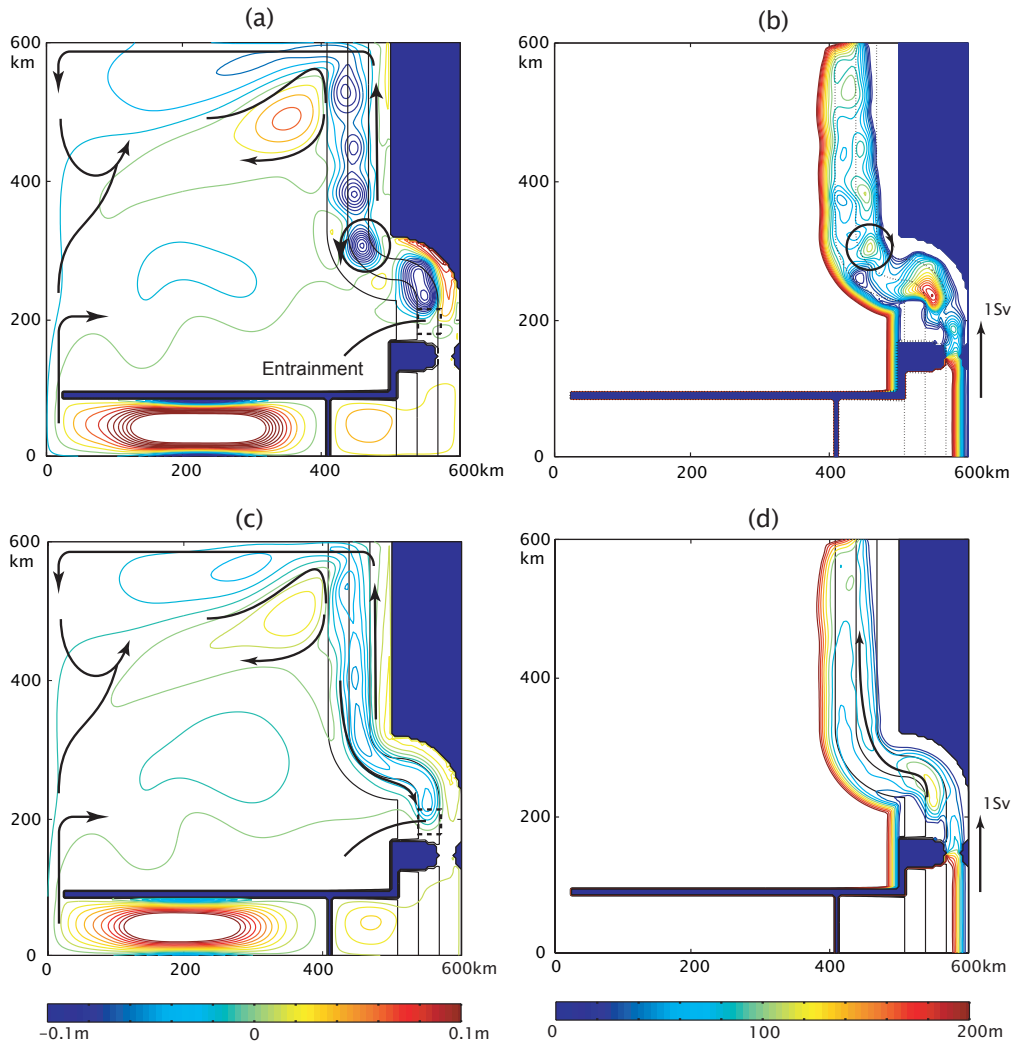

Figure 3-6: Case 6, where the continental slope is curved but constant. Bathymetric contours are drawn from 0 to 900 m every 300 m where the upper layer can directly contact the bottom. **(a)** A snapshot of the sea surface height contoured from -10 to 10 cm every 1 cm. Cyclonic eddies form within the continental slope region and the flow field is similar to Case 5. **(b)** A snapshot of the overflow layer thickness contoured from 0 to 200 m every 10 m. The overflow descends gradually while also forming anticyclonic eddies. **(c)** The time average sea surface height contoured the same way as (a). The topographic β-plume is trapped along the continental slope, with a cyclonic gyre off-shore (2.1 Sv) and a weak anticyclonic gyre in-shore (0.1 Sv). The cyclonic circulation along the northern boundary is an extension of the topographic β-plume because of the inertial overshoot at the northern boundary. **(d)** The time-mean overflow layer thickness contoured the same way as (b). The overflow descends gradually while part of the layer leaks and descends at a sharper angle.

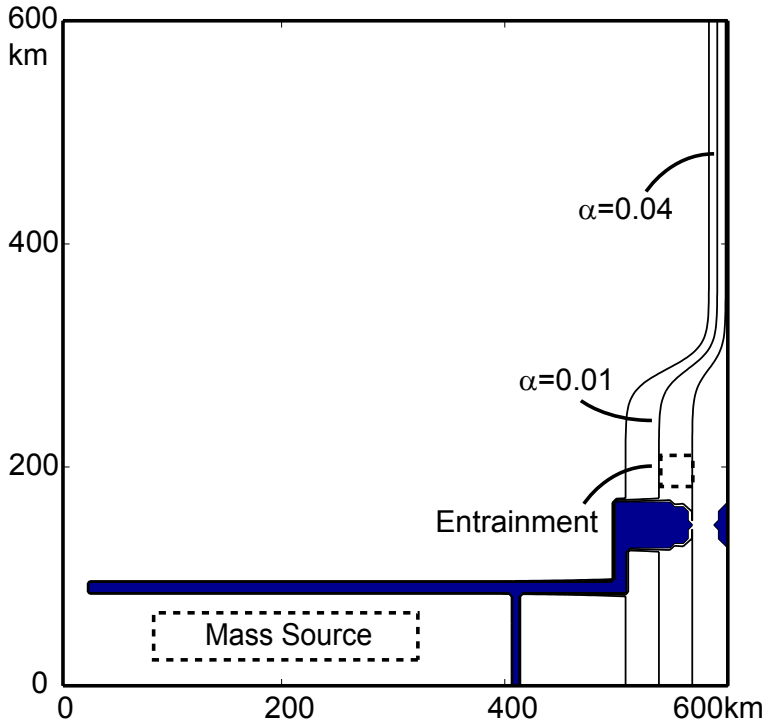

Figure 3-7: The bottom bathymetry for Case 7. The coastline is straight, just like Case 5, but the slope changes from 0.01 to 0.04 about 200 km downstream from the strait. This slope change occurs with a spatial scale close to the distance between the Gibraltar Strait and Cape St. Vincent. There is an curvature in the slope, an inevitable effect when the slope changes, but since the spatial scale is similar to that of Case 6, the flow is not expected to be strongly affected by this curvature. The location of the entrainment as well as other parts of the model are exactly the same as Case 5 and 6.

to be the crucial component of the continental slope that makes the topographic β-plume connect to the open ocean and create zonal jets.

In the continental slope region, the snapshot of the sea surface height shows cyclonic and anticyclonic eddies where the slope is 0.01 (Figure 3-8a). These eddies appear to follow the bathymetric contours (the PV contours) and decrease their length-scales as the slope increases from 0.01 to 0.04. The time mean shows the topographic β-plume along the continental slope between the entrainment region and the steep slope region (Figure 3-8c) but the topographic β-plume connects to the open ocean where the slope becomes steep, forming zonal jets in the open ocean. The snapshot of the overflow layer shows the flow descending the slope while also forming anticyclonic eddies (Figure 3-8b). The flow continues to flow along the slope even after reaching 900 m depth. Since this layer is still in contact with the continental slope, the flow is likely controlled by the topographic β (Figure 3-8d).

The cross-section of the flow field at x=200 km shows that the eastward zonal jet has a width of 100 km and a maximum velocity of 5 cm s^{-1} (Figure 3-9). The westward flow, which is the other branch of the topographic β-plume, has a weaker maximum velocity of 3 cm s^{-1}. The lower layer shows a broad westward flow near the northern boundary with a maximum velocity of 1 cm s^{-1}. In the open ocean, the velocity in the lower layer is much smaller than the upper layer.

The time-series of the velocity at the center of the eastward jet in the open ocean shows a fluctuation with a period of 180 days (Figure 3-10), which is a typical period for a linear long planetary baroclinic Rossby wave with a wavelength of about 200 km ($\omega \sim -\beta\kappa L_D^2$ where κ is the wavenumber). Note that this fluctuation is of order 0.2 cm $s^{-}1$ and much smaller signal than the standing Rossby wave meandering with a wavelength of about 150 km on top of the eastward zonal jet near the western boundary (Figure 3-8a). The velocity in the lower layer just below the eastward jet in the upper layer shows high frequency variability but not the Rossby wave observed in the upper layer.

The varying slope, gentle to steep, seen in the real bottom bathymetry was found to be an important topographic feature that connects the topographic β-plume to the

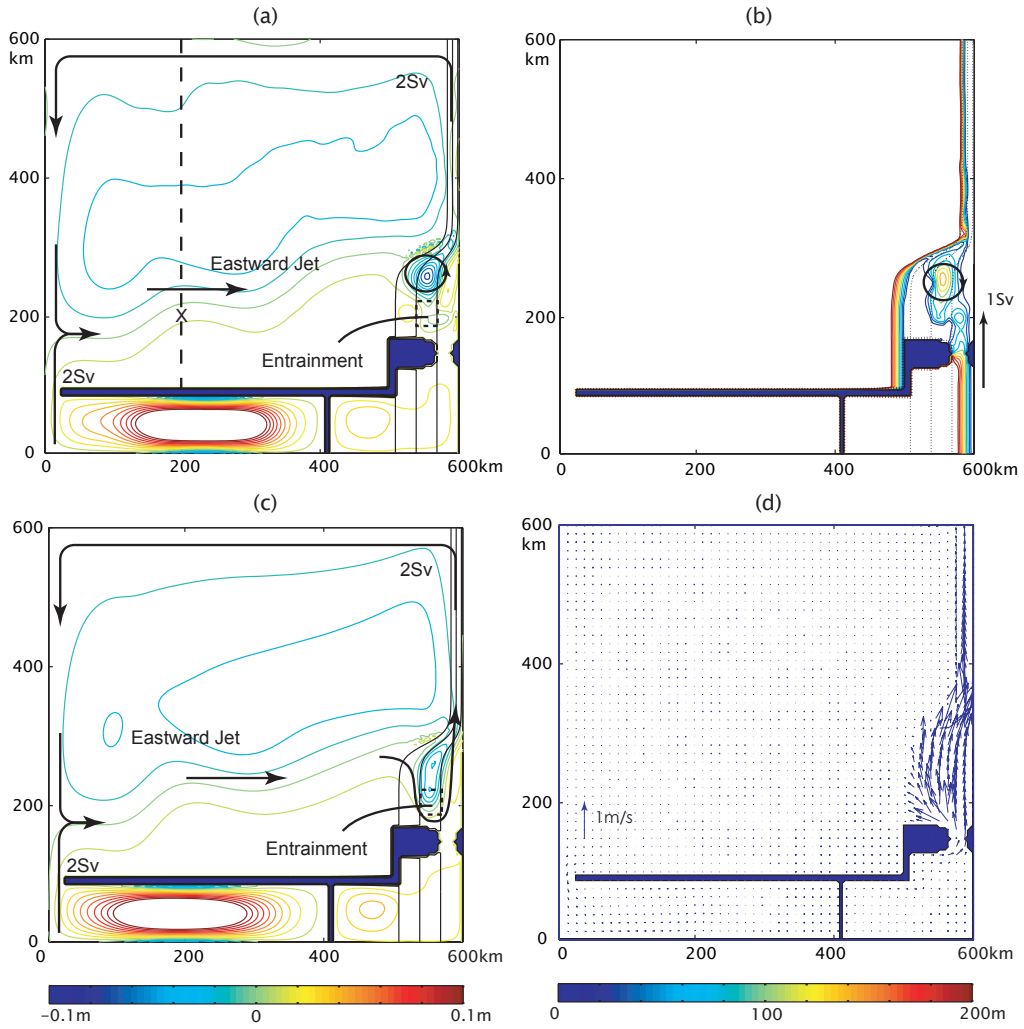

Figure 3-8: Case 7, where the slope changes from 0.01 to 0.04. Bathymetric contours are drawn from 0 to 900 m every 300m where the upper layer can directly contact the bottom. **(a)** A snapshot of the sea surface height contoured from -10 to 10 cm every 1 cm. Strong cyclonic eddies form in the continental slope region where the slope is gentle. **(b)** A snapshot of the overflow layer thickness contoured from 0 to 200 m every 10 m. Anticyclonic eddies are observed as overflow descends the slope. **(c)** The time mean of the sea surface height contoured the same way as (a). The topographic β-plume is trapped within the slope region where the slope is gentle but is directly connected to the open ocean where the slope is steep. An eastward zonal jet (4.0 Sv) forms in the open ocean and a westward flow (2.0 Sv) forms along the northern boundary. **(d)** The time mean velocity vectors of the overflow layer. The overflow flows along the continental slope even in the steep slope region.

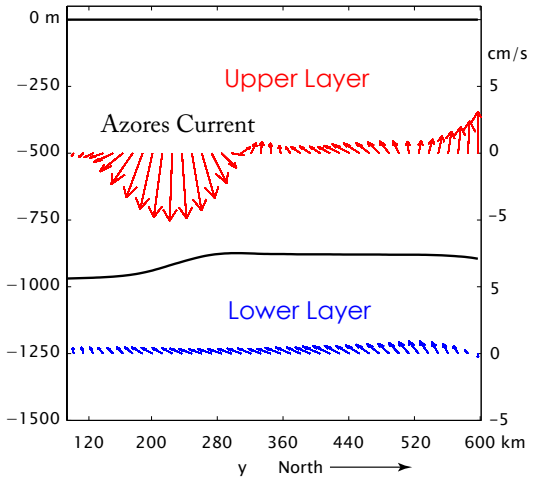

Figure 3-9: A cross-section of the velocity profile in the open ocean interior x=200km (dashed line in Figure 3-8). In the upper layer, an eastward zonal jet forms at about y=220 km with a maximum velocity of 5 cm s^{-1} and a westward flow forms along the northern boundary with a maximum velocity of 3 cm s^{-1}. The lower layer shows a weak westward flow near the northern boundary. The interface, superimposed on the figure, tilts up to the northward (+y direction) below the eastward jet.

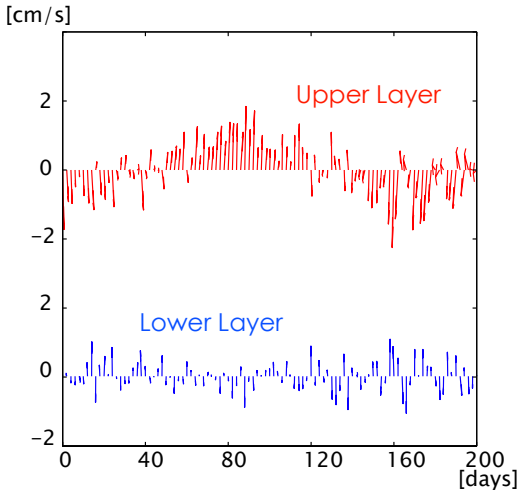

Figure 3-10: The time series of the velocity fluctuation (absolute value minus the time mean) of (upper layer) and underneath (lower layer) the eastward zonal jet (location x in Figure 3-8 or the dashed line in Figure 3-9). The upper layer shows a fluctuation with a period of about 200 days, which is likely the planetary Rossby wave. The magnitude of the fluctuation is not as strong as the mean (4–5 cm s^{-1}) but is of the same order. The lower layer shows time variability but not the Rossby wave seen in the upper layer.

open ocean and establish the Azores Current. In the next section, we will examine why the presence of a steep slope makes the formation of the Azores Current possible.

3.2 The effect of having a steep slope region

The existence of a steep slope region allows the topographic β-plume to escape from the continental slope region to the open ocean and establish an eastward zonal jet in the open ocean (Figure 3-8a). In this section, we will discuss why the presence of a steep slope region is important. But first, we will show why a topographic β-plume tends to be trapped in the continental slope region and how this tendency can be broken. Then the effect of a steep slope region on the topographic β-plume is discussed.

3.2.1 Why is the topographic β-plume trapped?

In order to understand the process that allows the topographic β-plume to connect to the open ocean, we first need to know why the topographic β-plume tends to be trapped in the continental slope region.

The exchange flow between the continental slope and open ocean regions is inhibited because the background PV is significantly different between the two regions. A water column in the open ocean is roughly 900 m thick. In order for the water column to move into the entrainment region, it needs to decrease its thickness from 900 m to 600 m (Figure 3-11). Assuming $f \gg \zeta$ (small R_o), this large thickness decrease implies that the water column must increase its PV by about 30%. In order for the water column in the entrainment region to move out of the continental slope region, the water column must increase its thickness from 600 m to 900 m thus decrease its PV by about 30%. Unless there are some processes that allow a water column to flow across slope, the significant PV difference between the continental slope and open ocean regions will prohibit a flow connecting the two regions from forming. This is the Taylor-Proudman Theorem and is the main reason why the dynamics in the continental slope is isolated from the open ocean (Brink 1998). The topographic β-

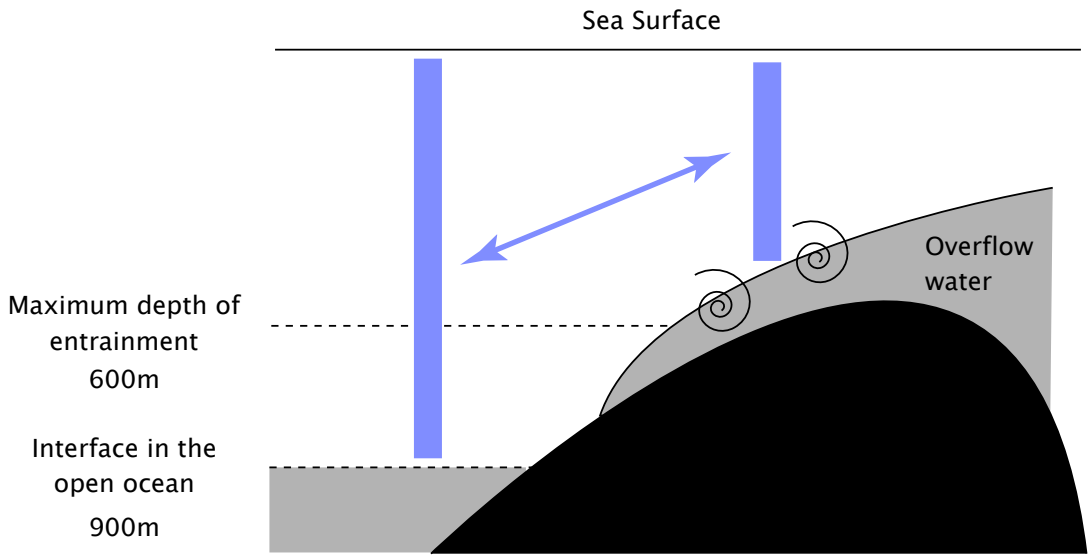

Figure 3-11: A schematic showing the thickness difference of the upper layer water between the open ocean region and the entrainment region. Entrainment occurs between 300–600 m depth whereas a water column in the open ocean is about 900 m thick. Thus, for a water column in the open ocean to enter the entrainment region, it must decrease its thickness from 900 m to at least 600 m. Conversely, for a water column near the entrainment region to move out of the continental slope region, it needs to increase its thickness about 300 m. These thickness changes correspond to about 30% of PV change assuming that the Rossby number is small.

plume in Case 5 and 6 did not connect to the open ocean in the interior because there were no processes that break this constraint (Figure 3-4 and 3-6). It is only at the northern boundary where inertial overshoot and friction likely broke this constraint and connected the topographic β-plume to the open ocean.

What are the processes that can break the constraint due to the Taylor-Proudman Theorem, create a time-mean flow in the cross-slope direction, and connect the topographic β-plume to the open ocean? The possible processes can be shown from the full vorticity equation of the upper oceanic layer:

$$\overline{\mathbf{U_1}} \cdot \nabla \overline{q_1} = \overline{q_1} w^* + \hat{k} \cdot \nabla \times \overline{\mathcal{F}_\mathbf{1}} - \nabla \cdot \overline{\mathbf{U}'_\mathbf{1} q'_1}. \tag{3.1}$$

This is the same equation as Eq 2.27, derived in Chapter 2. The LHS of this equation can be written as

$$\overline{\mathbf{U}}_{\mathbf{1}} \cdot \nabla \overline{q}_1 \;=\; -\overline{\mathbf{U}}_{\mathbf{1}} \cdot \left(\overline{\frac{q_1 \nabla h_1}{h_1}} \right) + \overline{\mathbf{U}}_{\mathbf{1}} \cdot \left(\overline{\frac{\nabla \zeta_1}{h_1}} \right) + \beta \overline{V}_1 \left(\overline{\frac{1}{h_1}} \right). \tag{3.2}$$

Using $h_1 = H_1 - h_{topo} - h_2$, where H_1 is the mean thickness of the upper layer and h_{topo} is the bathymetric height, the first term on the RHS further becomes:

$$\overline{\mathbf{U}}_{\mathbf{1}} \cdot \nabla \overline{q}_1 \;=\; \underset{(A)}{\overline{\mathbf{U}}_{\mathbf{1}} \cdot \left(\overline{\frac{q_1 \nabla h_{topo}}{h_1}} \right)} + \underset{(B)}{\overline{\mathbf{U}}_{\mathbf{1}} \cdot \left(\overline{\frac{q_1 \nabla h_2}{h_1}} \right)} + \underset{(C)}{\overline{\mathbf{U}}_{\mathbf{1}} \cdot \left(\overline{\frac{\nabla \zeta_1}{h_1}} \right)} + \underset{(D)}{\beta \overline{V}_1 \left(\overline{\frac{1}{h_1}} \right)} \tag{3.3}$$

We will now give a scale estimate for each of the terms, (A)–(D), using u, L, and H_2 for velocity, length, and lower layer thickness scales respectively. We will also take the scale of q_1 as $\frac{f}{H_1}$ since the Rossby number is small (of order 0.03), as shown in the previous section. Then the scales estimate of each of terms are (A) $\frac{f\alpha u}{H_1}$, (B) $\frac{fH_2 u}{LH_1}$, (C) $\frac{u^2}{L^2}$, and (D) βu, where α is the scale of the slope. The magnitude of each of the terms can be estimated by taking a ratio of terms (A)–(D) against (A): $\frac{A}{A}$= 1, $\frac{B}{A} = \frac{H_2}{\alpha L}$, $\frac{C}{A} = \frac{u}{fL}\frac{H_1}{\alpha L}$, and $\frac{D}{A} = \frac{\beta H}{f\alpha}$. Substituting u=0.1 m s^{-1}, L= 20 km, H_1 = 600 m, H_2 = 100 m, f=10^{-4} s^{-1}, β=2×10^{-11} m^{-1} s^{-1}, and α=0.01, the representative values for the topographic β-plume along the slope, the ratio of (A)–(D) against (A) are $\frac{A}{A}$= 1, $\frac{B}{A}$=0.2, $\frac{C}{A}$=0.06, and $\frac{D}{A}$=0.02. This shows that terms (B)–(D) are smaller than (A) and therefore, the flow across the PV gradient ($\overline{\mathbf{U}}_{\mathbf{1}} \cdot \nabla \overline{q}_1$) is roughly representing the flow across the bathymetric contours:

$$\overline{\mathbf{U}}_{\mathbf{1}} \cdot \nabla \overline{q}_1 \simeq \overline{\mathbf{U}}_{\mathbf{1}} \cdot \left(\overline{\frac{q_1 \nabla h_{topo}}{h_1}} \right). \tag{3.4}$$

So Eq 3.2 can be roughly expressed as

$$\overline{\mathbf{U}}_{\mathbf{1}} \cdot \left(\overline{\frac{q_1 \nabla h_{topo}}{h_1}} \right) \simeq \overline{q}_1 w^* + \hat{k} \cdot \nabla \times \overline{\mathcal{F}_{\mathbf{1}}} - \nabla \cdot \overline{\mathbf{U}'_{\mathbf{1}} q'_1}. \tag{3.5}$$

Eq 3.5 shows that a flow across the slope will form if one of the terms on the RHS,

PV forcing ($\overline{q}w^*$), friction ($\hat{k} \cdot \nabla \times \overline{\mathcal{F}}$) and eddy PV flux divergence ($\nabla \cdot \overline{\mathbf{U}'q'}$) terms, are of significant size. However, PV forcing does not exist outside the entrainment region so this term cannot create a flow between the entrainment region and the open ocean region (600–900 m). Thus, it is either friction or the eddy PV flux divergence term that must become significant, break the constraint due to Taylor-Proudman Theorem, establish a time-mean flow in the cross-slope direction, and connect the topographic β-plume to the interior of the open ocean.

3.2.2 The lateral Ekman number for a flow on a slope

In this section, we will examine how the steepness of the slope affects the topographic β-plume and leads to the formation of an eastward zonal jet in the open ocean. The PV balance (Eq 3.1) of Case 7 shows that the PV advection term and the eddy PV flux divergence term are the two balancing terms outside the entrainment region (Figure 3-12). Friction is mostly negligible except close to the boundary. Where the slope transitions from gentle to steep and adjacent to the open ocean, the PV balance shows that a flow up the PV gradient is supported by a positive eddy PV flux divergence. This balance tells us that the east-southward branch of the topographic β-plume flows up the slope in this region and thus establishes the eastward zonal flow in the open ocean close to this latitude. The presence of eddies near the steep slope region play an important role on connecting the topographic β-plume to the open ocean.

To examine the effect of the steepness on the topographic β-plume in the presence of eddies, we will make an approximation to the eddy PV flux divergence term based on two characteristics of the eddies near the steep slope region.

First, the eddy PV flux in the steep slope region has larger Reynolds Stress than form drag [2]. Direct estimate from the model does show the maximum Reynolds Stress (4×10^{-6} m s^2) larger than the form drag (8×10^{-7} m s^2). This can be seen also from

[2]The eddy PV flux can be separated into a Reynolds Stress term and form drag term. See Section 2.3.3 for details.

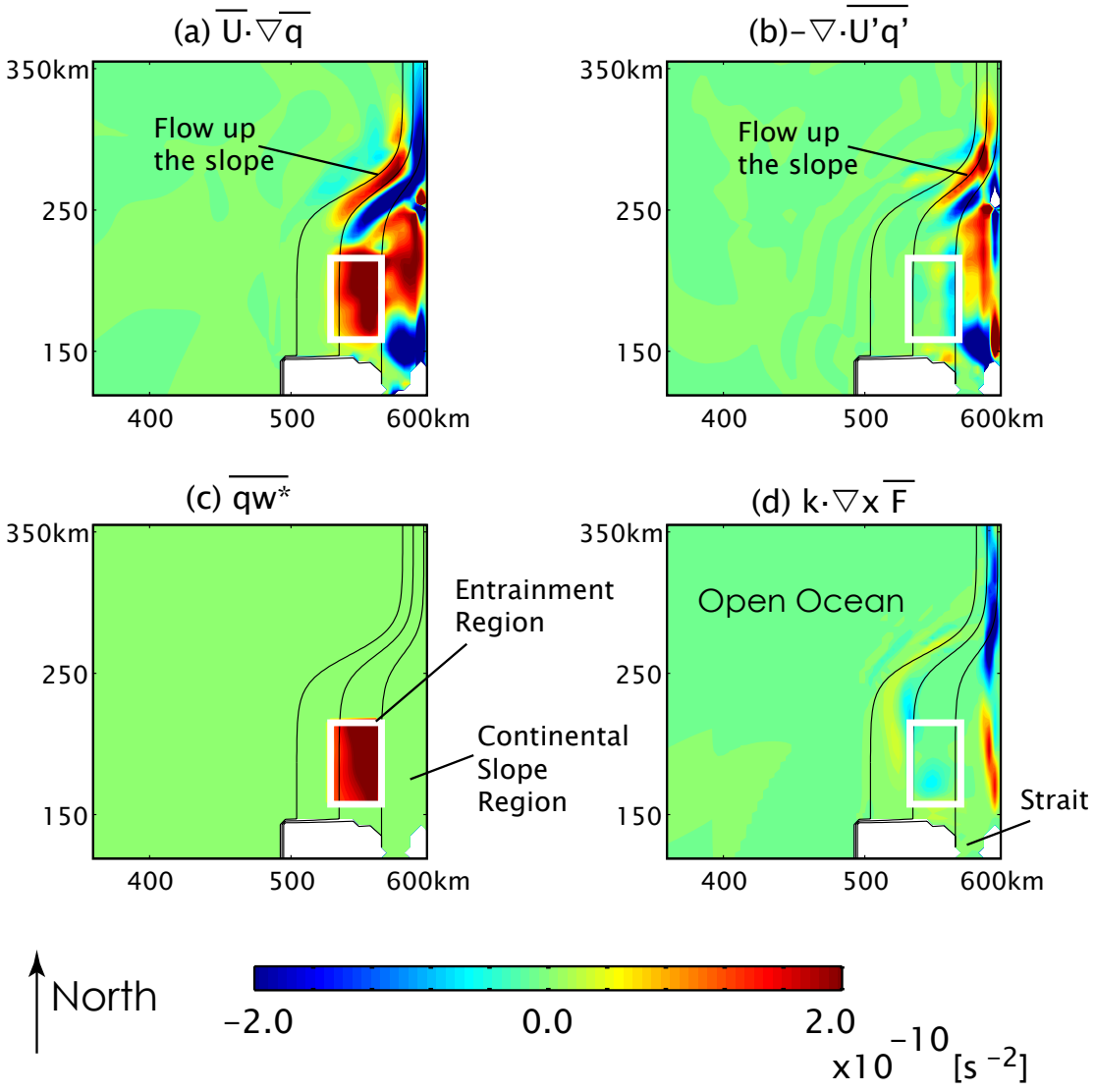

Figure 3-12: The PV balance (Eq 3.1) of Case 7 between the strait and the steep slope region. All plots use the same contour axis and interval. The black solid lines in the interior are -900, -600, -300, 0 m depths with shallower region to the east. **(a)** PV advection term: Large positive PV advection region exists in the entrainment region balancing the PV increase by entrainment (c). In the steep slope region, adjacent to the open ocean region, there is also a positive PV advection. **(b)** Negative of the Eddy PV flux divergence: Large positive region exists in the steep slope region adjacent to the open ocean. This is balancing the PV advection term (a). **(c)** PV forcing: Prescribed entrainment forces the PV to increase near the strait between the depth of 300 to 600 m. **(d)** Friction: Strong friction is observed near the eastern wall but is mostly weak in the interior.

comparing the magnitude of the two terms:

$$\frac{\text{Form Drag}}{\text{Reynolds Stress}} = \frac{fu'h'/H_1}{u'\zeta'} = \frac{fL}{u'}\frac{h'}{H_1}. \tag{3.6}$$

Substituting u'=0.2 m s^{-1}, L=20 km, $h' = 10$ m, and $H_1 = 600$ m, the representative values for the eddies in the steep slope region, Eq 3.6 estimates 0.17. So the eddy PV flux near the steep slope region can be roughly be taken as the Reynolds stress.

Second, the eddies appear to be fluxing momentum down the mean gradient of the flow where the slope transitions from gentle to steep (see next section for detail description). So to some degree, the Reynolds Stress can be represented as momentum diffusion which can be represented as something like viscosity:

$$\overline{\mathbf{U}'q'} \simeq \overline{\mathbf{u}'\zeta'} \simeq A_H^* \nabla\overline{\zeta}, \tag{3.7}$$

where A_H^* is the "effective" viscosity due to eddies. Although parameterizing the eddy PV flux divergence with a viscosity-like term is a crude way of parameterizing the Reynolds Stress (Adcock and Marshall, 2000) and cannot represent the effect of form drag, we will nonetheless try to learn the role of the steep slope region based on this approximation.

The basic PV balance of the topographic β-plume on the continental slope (outside the entrainment region), Eq 3.5, can then be roughly written as

$$\overline{\mathbf{U}}_\mathbf{1} \cdot \left(\overline{\frac{q_1 \nabla h_{topo}}{h_1}} \right) = \nabla \cdot \left(A_H^* \nabla\overline{\zeta} \right). \tag{3.8}$$

Using Eq 3.8, we will now examine how the slope affects the topographic β-plume on a continental slope. A_H^* will likely vary with space but we will treat this as a constant first so that effect of the slope can be diagnosed separately. Spatially varying A_H^* will be examined in the next section.

The lateral Ekman number

The impact of eddy viscosity on the topographic β-plume can be diagnosed from the lateral Ekman number, which we define here as the angle of the flow crossing the bathymetric contours (Figure 3-13). A flow with a large lateral Ekman number will cross the bathymetric contours with a steep angle and a flow with a small lateral Ekman number will cross the bathymetric contours with a shallow angle. The lateral Ekman number shows how the effect of eddy viscosity can change and affect the PV of a water column while traveling the same distance in the along-slope direction.

We will use the linear vorticity balance of Eq 3.8 (Pedlosky, 1974) to estimate the lateral Ekman number:

$$\frac{f\alpha}{H_1}u = A_H^* \frac{\partial^3 v}{\partial x^3}, \tag{3.9}$$

where H is the mean upper oceanic layer thickness in the slope region (Figure 3-14). This equation (Eq 3.9) is a balance between the vortex stretching by the flow in the cross slope direction (the LHS) and the convergence of the viscous flux of the relative vorticity associated the flow in the along-slope direction (the RHS).

By taking the width scale of the flow ∂x to be half the mass sink (external forcing) size $\frac{X_o}{2}$, the linear vorticity balance equation (Eq 3.9) can be scaled as

$$\frac{f_o\alpha}{H_1}u \quad = \quad A_H^* \frac{v}{(X_o/2)^3} \tag{3.10}$$

and solved for u/v:

$$\frac{u}{v} = \frac{A_H^* H_1}{f_o (X_o/2)^2 \delta h}. \tag{3.11}$$

Using the topographic depth difference across the flow δh (Figure 3-13):

$$\delta h = \alpha \frac{X_o}{2}, \tag{3.12}$$

to eliminate X_o in Eq 3.11, the Ekman number γ can be expressed using only exter-

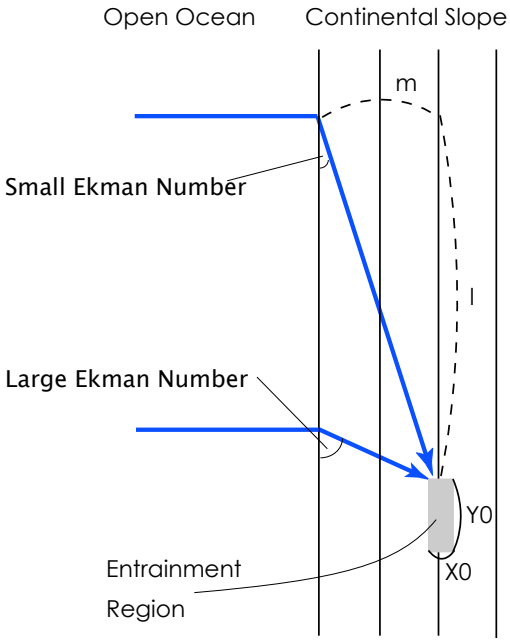

Figure 3-13: A schematic of the off shore branch of the topographic β-plume between the mass sink and the open ocean for a flow with large and small Ekman numbers. The distance between the mass sink and the open ocean is m. The mass sink has the size of X_0 and Y_0. Compared to a flow with a small Ekman number, a flow with a larger Ekman number connects from the open ocean to the entrainment region with a shorter distance, thus smaller l.

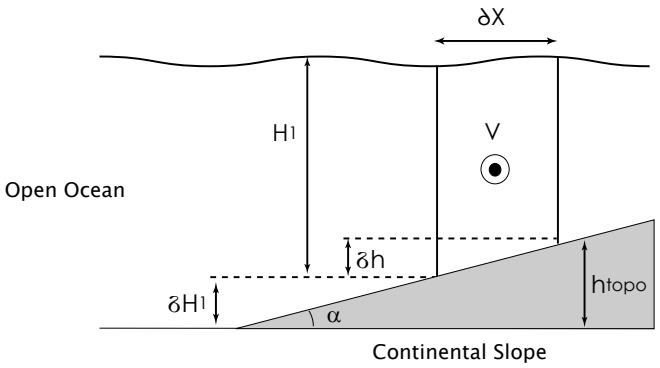

Figure 3-14: A schematic of the southward branch of the topographic β-plume on the slope. h_{topo} is the bottom bathymetric height and H_1 is the mean thickness of the upper layer in the continental slope region. ∂x is the cross-slope width of the flow. δh is the difference of the flow thickness within the flow and δH_1 is the bathymetric height difference between the flow and the open ocean region.

nally defined parameters:

$$\gamma \equiv \frac{u}{v} = \frac{A_H^* H_1 \alpha^2}{f_o \delta h^3}. \tag{3.13}$$

Eq 3.13 shows that the lateral Ekman number will increase quadratically as slope increases provided that A_H^* is a constant and not dependant on the slope. This quadratic increase of the lateral Ekman number with slope is a result of the spatial scale $\frac{X_o}{2}$ decreasing cubically with slope while the frictional length-scale $\frac{A_H^* H}{f\alpha}$ decreases only linearly with slope.

The location of the zonal jet

When the continental slope is located to the east of the open ocean region with a constant slope like that of Case 5 (Figure 3-3), we can estimate the location where the eastward current in the open ocean is likely to form based on Eq 3.13, the lateral Ekman number. We will focus on the eastward-southward branch of the topographic β-plume because this branch becomes the eastward zonal jet that is analogous to the Azores Current. When the distance between the entrainment region and the open ocean is a constant, a flow with a large Ekman number will require less meridional distance from the open ocean to the entrainment region compared to a flow with a small Ekman number (Figure 3-13) [3]. This behavior is similar to the arrested topographic wave on a f-plane shown by Csanady (1978). A flow with a larger Ekman number leads to a formation of the eastward current at a location closer to the entrainment region than a flow with a small Ekman number.

We will estimate the distance between where the eastward current forms in the open ocean and the location of the entrainment region using Eq 3.13, assuming that the Ekman number of the flow remains a constant. Taking the cross-slope distance between the entrainment region and -900 m depth where the interface intersects the

[3] Although the velocity of the eastward-southward branch of the topographic β-plume is directed eastward (from the open ocean to the continental slope region), the planetary Rossby waves that establish the flow in the open ocean travel westward (from the continental slope region to the open ocean). Thus, the open ocean flow field depends on the behavior of the flow field on the continental slope.

slope as m (Figure 3-13), a flow with an Ekman number γ will travel in the along-slope direction for

$$l = \frac{m}{\gamma} \tag{3.14}$$

until it is connected to the open ocean. Substituting Eq 3.13 and $\delta H_1 = \alpha m$ into Eq 3.14, where δH is the depth difference between the entrainment region and the open ocean, Eq 3.14 becomes

$$l = \frac{m}{\gamma} = \frac{f \delta h^3 \delta H_1}{A_H^* H_1 \alpha^3}. \tag{3.15}$$

This scale estimate shows that distance between the eastward zonal jet and the entrainment region decreases inverse cubically with slope.

A linear one-and-a-half-layer model with a large meridional domain (2000 km) is used to examine whether Eq 3.15 gives a fair scale estimate for where the eastward zonal current in the open ocean forms as slope is varied. This model will represent only the upper oceanic layer and we will use this model to examine what basic dynamic impact the steep slope region has on the topographic β-plume. The eddies are parameterized as a viscosity-like term and here, we will temporary set A_H^* to 10 $\mathrm{m^2 s^{-1}}$ the background viscosity coefficient used in the two-layer numerical model. The total mass transport by entrainment is kept constant. The depth range of the entrainment region (between 300–600 m depth) and the open ocean depth (900 m) is also kept fixed while the slope varies, so the PV difference between the entrainment and the open ocean will remain the same in all experiments. Since the transport of the topographic β-plume depends on Eq 1.5

$$\frac{V}{W} = \frac{f}{\beta^* X_o} = \frac{H_1}{\alpha X_o}, \tag{3.16}$$

keeping the depth range of entrainment fixed will make αX_o a constant, thus the transport of the topographic β-plume V is also constant in all experiments.

When the slope is 0.01, the eastward current forms about 500 km from the en-

trainment region (Figure 3-15a)[4]. But when the slope is 0.04, the eastward current forms about 50 km from the entrainment region (Figure 3-15b). The magnitude of the effect of viscosity on a topographic β-plume can increase as slope increases and make l decrease. When slope is fixed but A_H^* is varied, l decreases inverse proportionally to A_H^* (Figure 3-16) and shows that the scale estimate of Eq 3.15 is roughly capturing how the relative magnitude of viscosity on a topographic β-plume changes with slope. On a steep slope, the effect of viscosity on a topographic β-plume increases and makes the topographic β-plume connect to the open ocean close to the entrainment.

The zonal jet width

The planetary Rossby waves propagating westward establish the flow field in the interior of the open ocean by informing the open ocean of the flow structure of the topographic β-plume located to the east of the open ocean. Since there is no direct forcing in the open ocean, the meridional length scale of the off-shore branch of the topographic β-plume is going to largely determine the meridional length scale of the eastward current in the open ocean (Figure 3-17). An increase in the lateral Ekman number leads to a smaller meridional length scale for a flow on the continental slope region, which then leads to a decrease in the width of the eastward current in the open ocean. Thus the increase in lateral Ekman number not only allows the eastward current in the open ocean to form close to the entrainment but it can also decrease the width of this eastward current.

Taking the across-slope length scale of the off-shore branch of the topographic β-plume again as half of the entrainment forcing size, $X_o/2$, the along-slope length scale Y of this flow (Figure 3-17) can be estimated using the lateral Ekman number γ as

$$Y = \frac{X_o/2}{\gamma}. \tag{3.17}$$

[4]The location of the Azores Current is determined from the location of the maximum zonal velocity where the interface of the two layers intersect with the continental slope (roughly at 900 m depth).

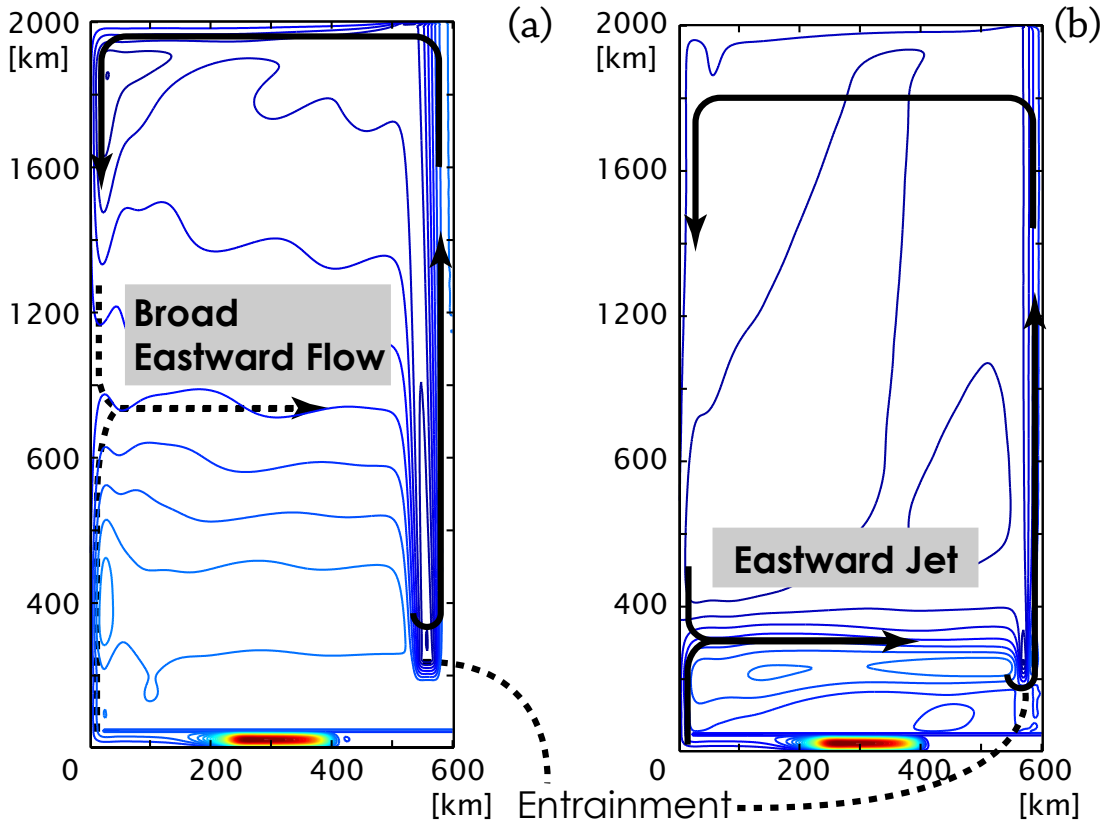

Figure 3-15: **(a)** Topographic β-plume on a gentle slope, α=0.01. The topographic β-plume is trapped in the continental slope region for over 1000 km. The off-shore branch of the topographic β-plume diffuses into the open ocean region gradually and thus results in a broad and weak eastward flow. **(b)** Topographic β-plume on a steep slope, α=0.04. The topographic β-plume is connected to the open ocean about 100–150 km from the entrainment region and thus a narrow eastward flow forms.

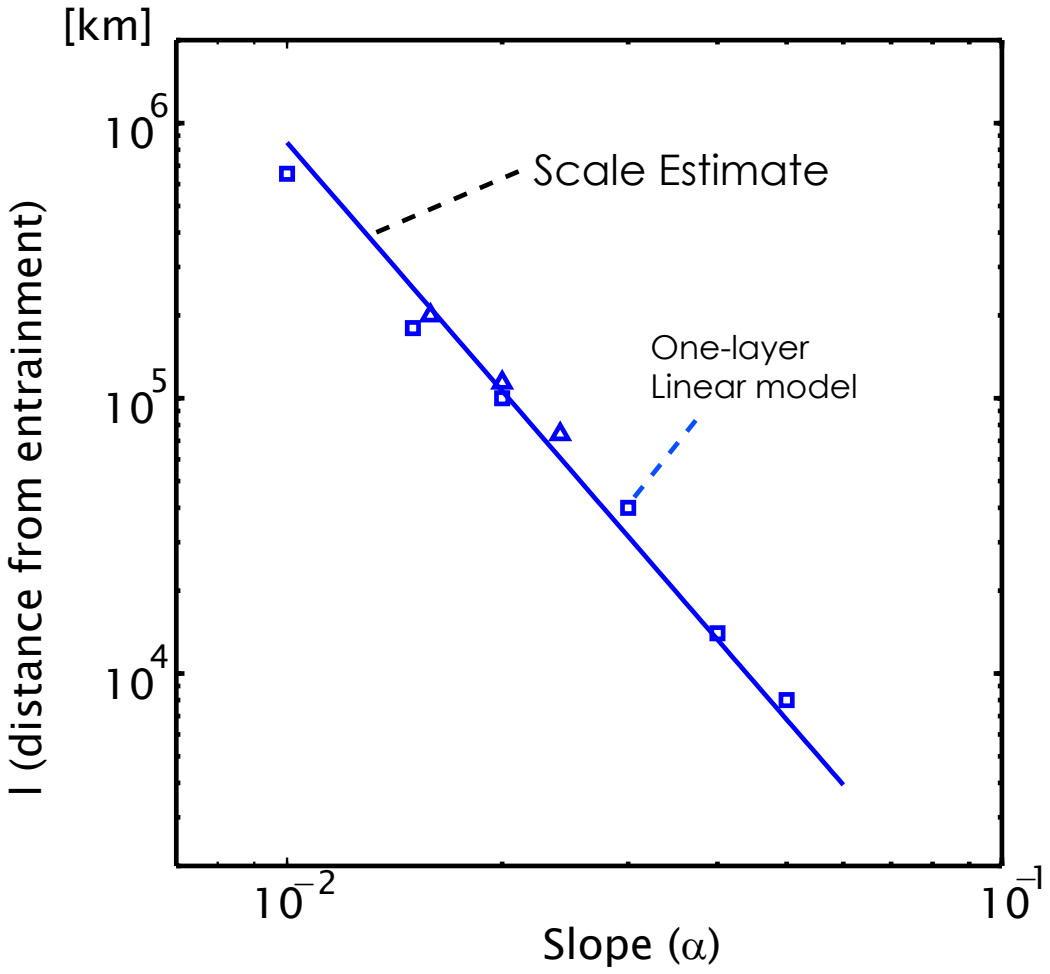

Figure 3-16: The distance between the eastward zonal flow and the entrainment region, l, as a function of α. The blue squares are the results from the one-layer linear model when the slope is varied. The black solid line is the scale estimate of l using Eq 3.15 showing the decrease of l as inverse cubic to α, which matches with the model results reasonably well. The blue triangle are the results from the one-layer linear model when A_H^* is varied from 10 $\mathrm{m^2 s^{-1}}$ while keeping the slope the same (0.01). These results are plotted where the slope is $\alpha = 0.01 * (\frac{A_H^*}{10})^{1/3}$ so that change in A_H^* would be equivalent to the change in slope according to Eq 3.15: $0.01^3 * A_H^* = \alpha^3 * 10$.

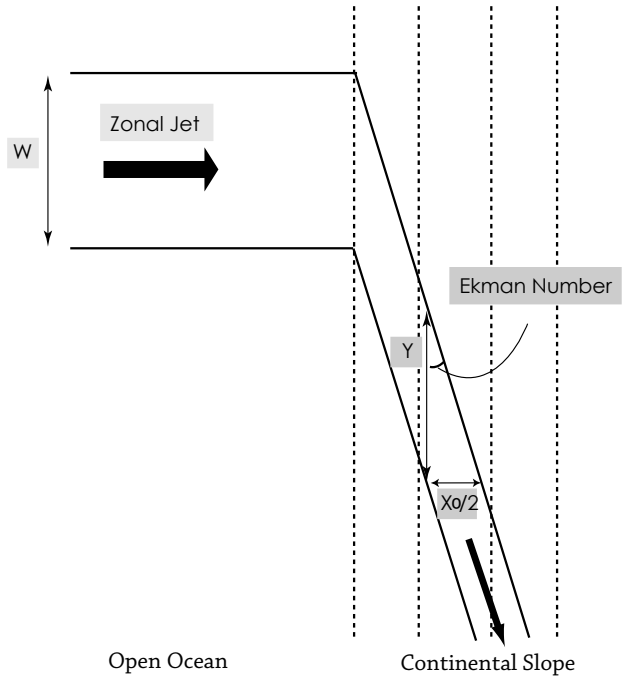

Figure 3-17: A schematic of how the width of the zonal jet changes with slope. (Only the east-southward branch of the β-plume is drawn.) Taking the cross-slope length scale of the flow as $X_o/2$, the along slope length scale Y can be estimated from the lateral Ekman number γ. Assuming that the later Ekman number is constant, this flow will connect with the open ocean with the along-slope length scale Y where it also sets the length scale of the zonal jet in the interior W to Y.

Substituting Eq 3.13 for γ and also using $\delta h = \alpha \frac{X_o}{2}$ to eliminate X_o, the equation above can be rewritten as

$$Y = \frac{X_o/2}{\gamma} = \frac{f(X_o/2)^3 \delta h}{A_H^* H_1} = \frac{f \delta h^4}{A_H^* \alpha^3 H_1}. \tag{3.18}$$

When a flow on the continental slope is connected to the open ocean with an along-slope length scale Y, this Y is what will determine the meridional width scale W for the eastward current:

$$W = Y = \frac{f \delta h^4}{A_H^* \alpha^3 H_1}. \tag{3.19}$$

Eq 3.19 shows that the width of the eastward current decreases cubically as slope increases.

A linear one-and-a-half-layer model is again used to learn how the width of the eastward current in the open ocean interior is controlled (the same experiments used in Figure 3-16). When the slope is gentle ($\alpha = 0.01$), the eastward current is broad (1400 km) (Figure 3-15). But when the slope is steep ($\alpha = 0.04$), the eastward current becomes narrow (150 km). The model experiments show the width of the eastward current decreases as slope increases (Figure 3-18) because the effect of a given viscosity increases on a steeper slope and the topographic β-plume connects to the open ocean within a short distance. When slope is fixed, but A_H^* is varied, W changes inverse proportional to A_H^* (Figure 3-18) and shows that the scale estimate of Eq 3.19 is roughly capturing how the relative magnitude of viscosity on a topographic β-plume changes with slope.

In this section, the effect of viscosity on a topographic β-plume on a constant slope was shown to increase as slope increases. Thus the topographic β-plume connects to the open ocean closer to the entrainment region and establishes a narrower eastward zonal jet in the open ocean as slope increases.

3.2.3 The varying slope and the role of eddies

The previous section examined how the topographic β-plume on a continental slope with a constant slope connects to the open ocean through viscosity and how the slope affects its effectiveness. Based on these results, we will now revisit Case 7 (Figure 3-8) and discuss how the topographic β-plume on a continental slope connects to the open ocean when a slope change, from gentle to steep, exists.

The existence of the steep slope region

The bottom bathymetry used in Case 7 is flat (h_{topo}=-900 m) over most of the model domain but has a slope along the eastern boundary:

$$h_{topo} = 0.01 * (x - 6 \times 10^5) * \left(2.5 - 1.5 * \tanh\left(\frac{y - 28 \times 10^4}{20 \times 10^3}\right)\right), \qquad (3.20)$$

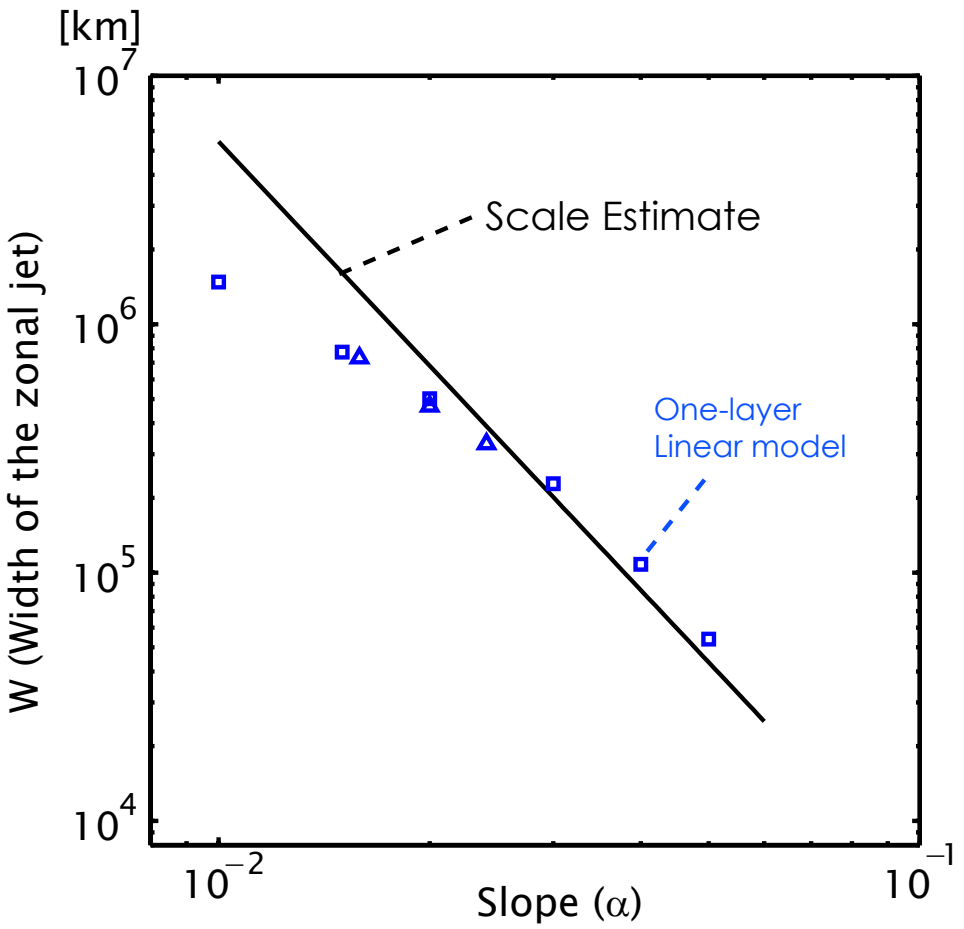

Figure 3-18: The width of the zonal jet, W, as a function of α. The blue squares are the results from the one-and-a-half linear model. The black solid line is the scale estimate using Eq 3.19, showing the decrease of W is inverse cubic to α. The scale estimate captures the model result reasonably well for steep slope but overestimates for gentle slope. The blue triangle are the results from the one-layer linear model when A_H^* is varied from 10 $\mathrm{m^2 s^{-1}}$ while keeping the slope the same (0.01). These results are plotted where the slope is $\alpha = 0.01 * (\frac{A_H^*}{10})^{1/3}$ so that change in A_H^* would be equivalent to the change in slope according to Eq 3.19: $0.01^3 * A_H^* = \alpha^3 * 10$.

where x and y are in meters (Figure 3-19). This continental slope has a slope of 0.01 (gentle) near the entrainment region but this slope will smoothly change to 0.04 (steep) about 80 km further north. The transition occurs much closer (meridionally) to the entrainment region compared to where the topographic β-plume on a constant slope of 0.01 will establish an eastward zonal flow in the open ocean interior ($\simeq$ 700 km, see Figure 3-15a).

To examine the basic effect of having a steep slope region, we will use a linear one-and-a-half layer model with a constant eddy viscosity coefficient of 10 m^2 s^{-1}, just like the one used in the previous subsection but now with a domain size of 600 km $\times$ 600 km like Case 7. Because the meridional domain of this model is smaller than the distance required for the topographic β-plume to connect to the open ocean interior directly, an eastward northern boundary current will form when the slope is a constant (Figure 3-20a). However, in the presence of steep slope region, the topographic β-plume connects to the open ocean interior at about 120 km from the entrainment region (Figure 3-20b). The steep slope is capable of increasing the effect of viscosity on the topographic β-plume considerably such that the topographic β-plume can connect to the open ocean interior within the model domain. Although the eastward zonal flow in the open ocean in this experiment is still much broader than that of Case 7 (Figure 3-8a), the experiment qualitatively shows that the existence of a steep slope can make the topographic β-plume connect to the open ocean and form an eastward zonal flow. The parameter dependence of where the eastward zonal jet forms in the open ocean and how its width is determined needs to be examined more rigorously but additional experiments do indicate that the eastward zonal jet forms at a closer location to the entrainment region and with a narrower width as the transition from gentle slope to steep slope occurs more abruptly and closer to the entrainment region. This is in agreement with the results from the previous subsection.

The role of eddies near the steep slope region

The linear one-and-a-half layer model showed that the existence of a steep slope region allows the topographic β-plume to escape from the slope region and form an eastward

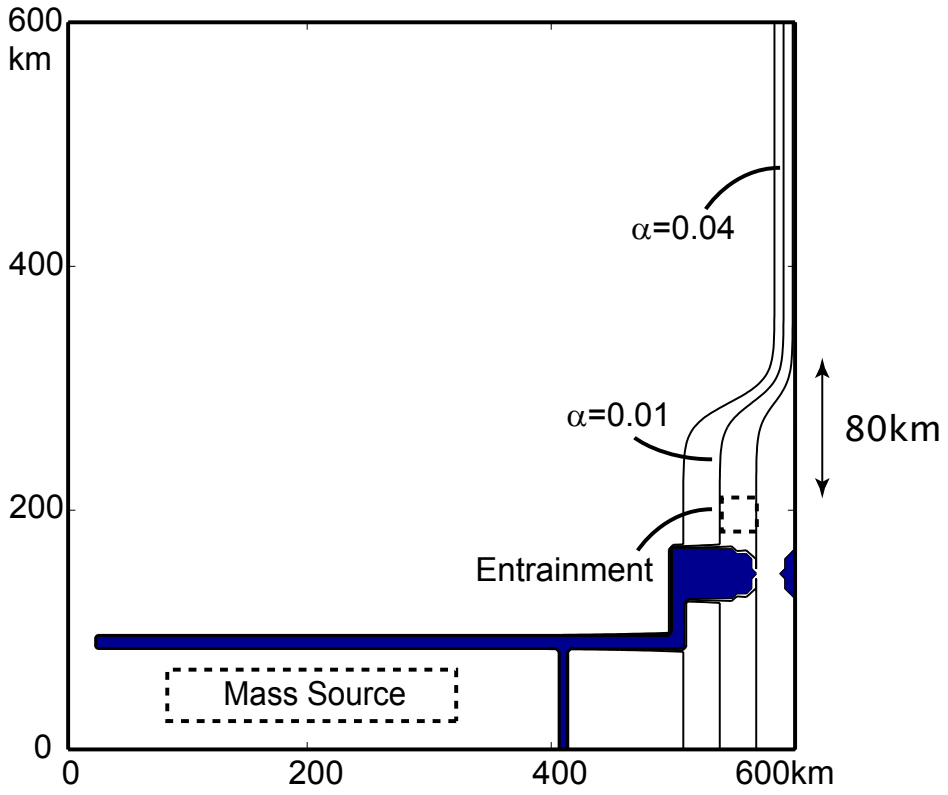

Figure 3-19: The bottom bathymetry for Case 7 (same figure as Figure 3-7). The continental slope region exists at the eastern boundary of the open ocean with a slope of 0.01 near the entrainment region and 0.04 further north. This transition is smooth and takes about 80 km, about the length scale of the slope change in the Gulf of Cadiz. The entrainment region exists between -600–300 m depth and is 20–60 km downstream from the strait.

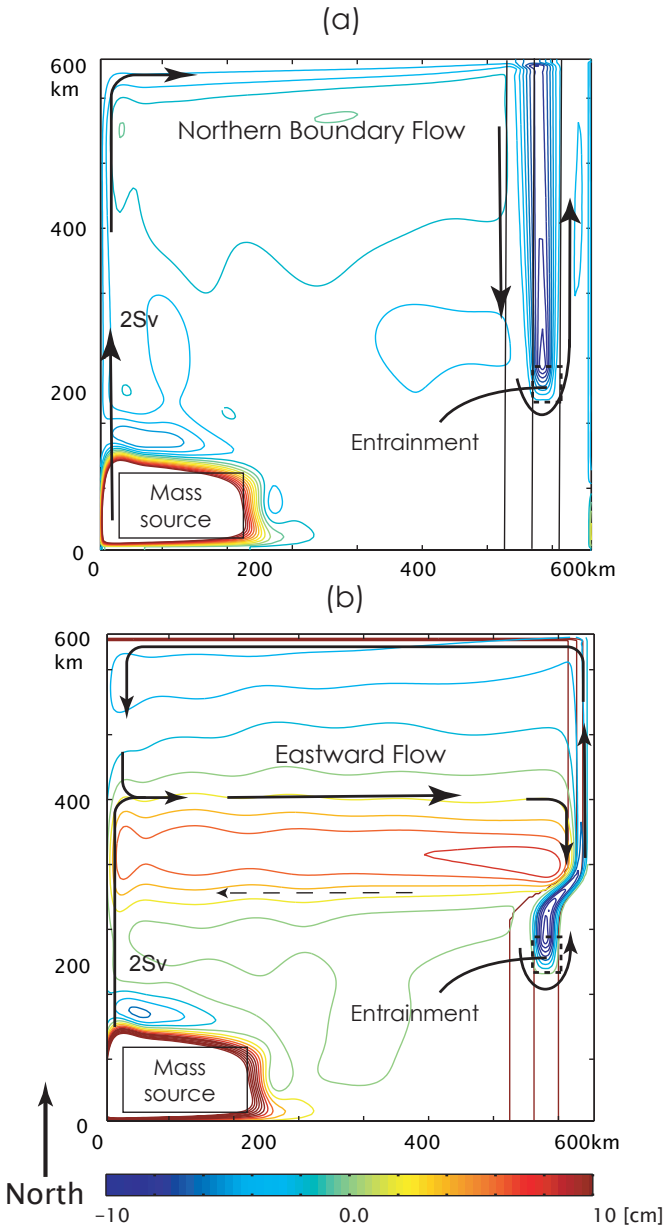

Figure 3-20: **(a)** The sea surface height from the one-layer linear model with a constant slope of 0.01 on the eastern boundary and with a viscosity coefficient of A_H^*=10 $m^2\ s^{-1}$ (the background viscosity coefficient used in the two-layer primitive equation model). The topographic β-plume does not connect to the open ocean within the model domain and an eastward northern boundary layer flow that supports the mass transport from the mass source to the mass sink will form. **(b)** The sea surface height from the one-layer linear model using a viscosity coefficient of A_H^*=10 $m^2\ s^{-1}$ but with a bottom bathymetry similar to Case 7. The eastward zonal flow forms in the open ocean interior about 120km from the entrainment region and with a width of about 200 km.

zonal jet close to the entrainment region by increasing the effect of viscosity on the topographic β-plume compared to a gentle slope. However, compared to the eastward zonal jet in Case 7, where a two-layer primitive equation model is used (Figure 3-8a), the eastward zonal flow in the one-and-a-half layer model has a width that is still too large and the location of the eastward zonal jet is also still considerably too far north. What is the main reason for this difference? The main reason is that the one-and-a-half layer linear model is based on a given A_H^*, which is 10 m^2 s^{-1} and is uniform across the basin, where as the two layer model of Case 7 has large eddy viscosity coefficient near the near the steep slope region. The one-and-a-half layer linear model with a uniform viscosity coefficient is convenient for learning the effect of the slope but has its limitation of not including the effect of spatially varying A_H^* nor capable of determining A_H^* internally. We will show next that the combination of large A_H^* and the steep slope is what will lead to the formation of a narrow eastward zonal flow in the open ocean.

When the eddies are transporting momentum dominantly to the direction down gradient of the mean flow, a diffusion approximation $\overline{\mathbf{u}'\zeta'} \simeq -A_H^* \nabla\overline{\zeta}$ can be made and by taking the ratio of $\overline{\mathbf{u}'\zeta'}$ over $\nabla\overline{\zeta}$, A_H^* can be estimated. In Case 7, $\overline{u'\zeta'}$ and $\nabla\overline{\zeta}$ are found to strongly correlate in the transition region from gentle to steep with the eddy viscosity coefficient A_H^* estimated to be about 460 m^2 s^{-1} (Figure 3-22a). While the eddies are in the gentle slope region, they do not appear to be transporting momentum dominantly in the direction down the gradient of the mean flow (Figure 3-22b). The topographic β-plume does not strongly diffuse off-shore in this region, which is in agreement with the topographic β-plume on a gentle slope not connecting to the open ocean even in presence of eddies (e.g. Case 5). The reason why the eddies start to have strong down gradient vorticity transfer as the eddies flow from a gentle slope to steep slope may be due to geometric changes in the eddy size or additional instability where the slope changes abruptly (Bracco and Pedlosky, 2003) but will need to be investigated in the future. Here we will remain focused on understanding how the strong eddy viscosity in the steep slope region affects the topographic β-plume.

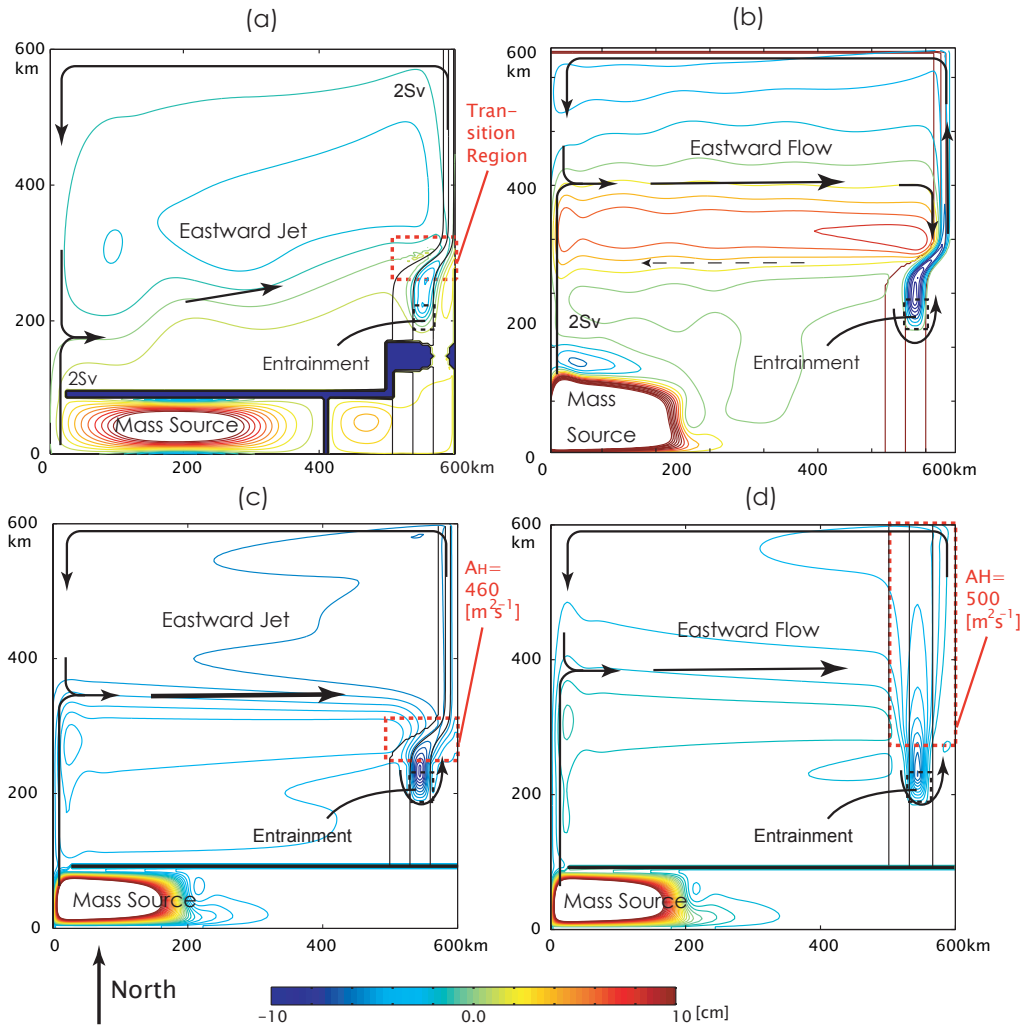

Figure 3-21: Black solid lines represent the -900, -600, -300, and 0 m depth contours with shallower region to the east. **(a)** The time-mean sea surface height from the two-layer primitive equation model (Case 7). The eastward zonal jet forms in the open ocean about 60km from the entrainment region, where slope changes abruptly. The dotted region is where the effective viscosity is estimated for Figure 3-22. **(b)** The sea surface height from the one-layer linear model using a constant viscosity coefficient of A_H^*=10 m^2 s^{-1} (the background viscosity coefficient used in the two-layer primitive equation model). The eastward zonal jet forms in the open ocean region about 120km from the entrainment region. This is the same figure as Figure 3-20b. **(c)** The sea surface height from the one-layer linear model using a viscosity coefficient of A_H^*=10 m^2 s^{-1} uniformly across the basin except where the slope change from gentle to steep. There, the viscosity coefficient of A_H^*=460 m^2 s^{-1} is used. The eastward zonal jet forms in the open ocean region about 60km from the entrainment region similar to where it forms in the primitive equation model (a). **(d)** The sea surface height from the one-layer linear model with a constant gentle slope and a viscosity coefficient of A_H^*=500 m^2 s^{-1} north of the entrainment region. The eastward flow occurs about 120 km to the north and not as narrow as (c).

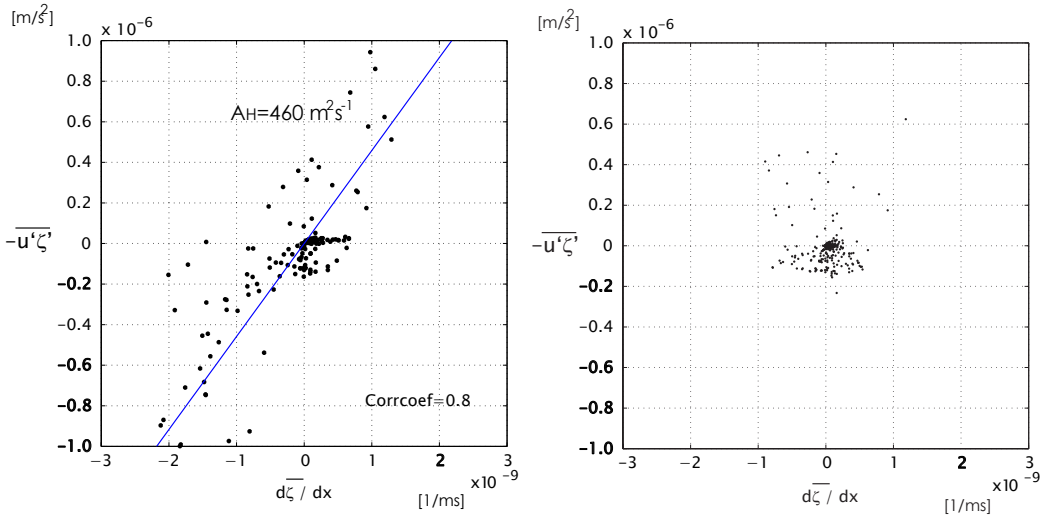

Figure 3-22: The Reynolds Stress in the across-slope direction($-\overline{u'\zeta'}$) plotted against the mean vorticity gradient across-slope ($\overline{\zeta}_x$) in the steep slope region. The ratio of the two terms ($\frac{-\overline{u'\zeta'}}{\overline{\zeta}_x}$) is the estimate for the viscosity coefficient (A_H^*) for each point thus the slope of the best fit line will give the rough estimate for the viscosity coefficient in the region. **(a)** The region where slope varies from 0.01 to 0.04 (Figure 3-21a) Though the orientation of the slope changes with location, $-\overline{u'\zeta'}$ and $\overline{\zeta}_x$ are estimated so that the eddy momentum flux are the values in the cross-slope direction and the vorticity gradient in the cross-slope region respectively. There is reasonable correlation between the two terms, with a correlation coefficient of 0.8, and the viscosity coefficient estimates to be about 460 m^2 s^{-1}. **(b)** The region where slope is constant ($\alpha = 0.01$). The Reynolds Stress is still of significant size but there is no significant correlation with the mean vorticity gradient. The eddies do not appear to be strongly fluxing momentum down-gradient of the mean in this region.

The large eddy viscosity in the slope transition region appears to play a crucial role on establishing the eastward zonal jet in the open ocean. Based on Eq 3.13, the increase in slope and the viscosity coefficient will increase the lateral Ekman number about 640 times. The significant increase in this lateral number can diffuse the topographic β-plume to the open ocean within a few kilometers such that an eastward zonal jet may form. A narrow zonal jet is observed to form at the latitude of the slope transition region (Figure 3-21b) when an one-and-a-half layer linear model is solved with enhanced viscosity coefficient of A_H^*=460 m^2 s^{-1} only in the slope transition region and A_H^*=10 m^2 s^{-1} rest of the basin that roughly mimic the role of eddies in Case 7 (Figure 3-21a). This experiment demonstrates the significance of the eddies on connecting the topographic β-plume to the open ocean and establishing a narrow zonal jet [5]. An additional off-shore diffusion of the topographic β-plume may also occur from the spatial variance in A_H^*. This is because the eddy viscosity term is a sum of two terms when A_H^* varies spatially:

$$\nabla \cdot \left(A_H \nabla \overline{\zeta} \right) = A_H \nabla^2 \overline{\zeta} + \nabla A_H^* \cdot \nabla \overline{\zeta}. \tag{3.21}$$

The second term is zero when A_H^* is uniform and in that case Eq 3.13 gives a reasonable estimate of the lateral Ekman number as described in the previous section. The magnitude of the second term on the RHS of Eq 3.21 compared to the first term can be diagnosed by taking the ratio of across-slope length scale of A_H^* variance (l_{AH}) against the width of the topographic β-plume in the continental slope region ($X_o/2$):

$$\frac{A_H^* \nabla}{\nabla \cdot A_H^*} = \frac{(X_o/2)^{-1}}{l_{AH}^{-1}} = \frac{l_{AH}}{X_o/2}. \tag{3.22}$$

Since both length scales, l_{AH} and $X_o/2$, are similar in the slope transition region of Case 7 ($\simeq$ 10 km), the ratio shows that the spatial variance in A_H^* can significantly enhance the off-shore diffusion of the topographic β-plume. Further experiments are

[5] The inertial overshoot occurs at the western boundary for the primitive equation model such that the eastward zonal jet tilts in southwest-northeast direction but the location of where the eastward jet connects to the continental slope region are similar in both cases (Figure 3-21a and c.)

necessary to understand more exact impact of varying A_H^* on the lateral Ekman number but the scaling estimate above shows that it can significantly enhance the Ekman number and that the topographic β-plume can connect to the open ocean at an even shorter distance than what Eq 3.13 estimates.

The large eddy viscosity plays a significant role in connecting the topographic β-plume to the open ocean but a strong viscosity coefficient of order A_H^*=460 m^2 s^{-1} alone cannot create a narrow zonal jet in the open ocean. The steep slope has an equally important effect as the large eddy viscosity coefficient. An experiment with A_H^* that abruptly increases from 10 to 500 m^2 s^{-1} in about 40 km on a gentle slope (0.01) shows the eastward zonal flow in the open ocean interior that is still north and broad compared to Case 7 (Figure 3-21d). (This increase in A_H^* occurs exactly on the same spatial scale as the slope change of Case 7.) The combination of large A_H^* and the steep slope, increasing the effect of eddy viscosity on the topographic β-plume , is necessary for the topographic β-plume connect to the open ocean and establish the narrow eastward zonal jet in Case 7 (Figure 3-21b).

In this subsection, the eddies were shown to play a significant role on connecting the topographic β-plume to the open ocean near the steep slope region and establishing the zonal jets. The eddies were fluxing momentum down the mean gradient of the flow considerably near the steep slope region thus increasing the effective viscosity in the region compared to that on a gentle slope. This role of eddies in the steep slope region along isopycnal and is quite different from the cross-isopycnal momentum transfer that results from baroclinic instability near the strait. The steep slope further increased the effect of this eddy viscosity in the steep slope region compared to that on a gentle slope. The combination of the two made the topographic β-plume quickly connect to the open ocean near the steep slope region and establish the eastward zonal jet in the open ocean.

In the next section, we will investigate whether the results from the one- and two-layer models are robust in the presence of stratification in the upper oceanic layer.

3.3 The effect of stratification

All the model results in the previous sections are based on either one- or two-layer models in order to highlight the basic dynamics of the overflow-upper ocean interaction. The real ocean is stratified, however, so in this section, we will examine whether the eastward zonal jet observed in the two-layer model is a robust feature in the presence of stratification.

The effect of stratification will be tested by using a three layer model, which splits the upper layer of the two-layer model into two layers at 600m depth (Figure 3-23). The middle layer (600–900 m) represents the density levels that are lighter than the overflow but are heavier than the density levels that are entrained to the overflow layer. The 'new' upper layer represents the density levels that are entrained to the overflow and lighter. Since the interface is at 600 m, the same depth as the maximum depth of entrainment, a water column is not required to change its PV significantly, in order to get into the entrainment region from the open ocean. Thus the eastward jet might connect to the entrainment region directly rather than following the continental slope as observed in Case 4. Note that this multiple layer model does not test the effect of resolving stratification in the overflow layer. This is because the focus of this section is primarily on understanding the upper-layer response to overflows. This setup will also not test the effect of stratification in the density level of the upper oceanic layer that is lighter than what is entrained to the overflow. This effect will be discussed in the next Chapter.

The sea surface height of the three-layer model shows an eastward zonal jet between 35–36^o N (Figure 3-24) with transport of 4.5 Sv, a maximum zonal velocity of 5.0 cm s^{-1}, and a sea surface height difference of 7–9 cm across the current, analogous to the Azores Current. The eastward current has a transport that is roughly the same as the two-layer model but the maximum velocity increases to 3.5 cm s^{-1} and the sea surface height difference across the current also increases to 5-6 cm. These increases are simply from continuity, having less thickness in the upper layer than the two-layer model, but shows the surface intensified character of the eastward current that was

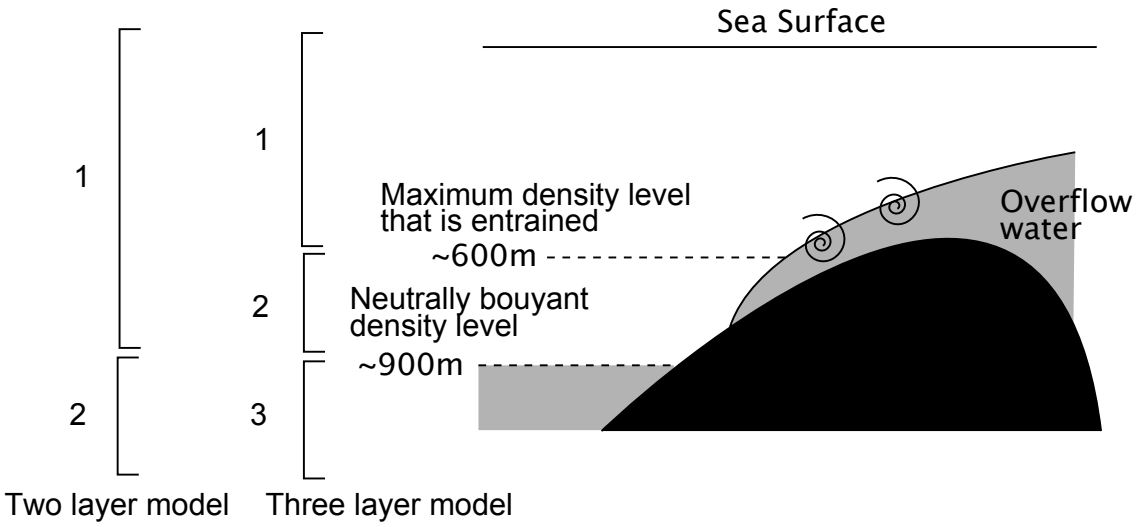

Figure 3-23: A schematic of how the layer interfaces are configured in the two and three layer model. The two-layer model splits the overflow and the upper layer by setting the density of the overflow water to that of the product water. The interface between the overflow water and the upper ocean water is about 900 m in the open ocean. The three-layer model further splits the upper layer of the two-layer model into two at the maximum density level that is entrained to the overflow. This isopycnal is about 600 m in the open ocean. The new middle layer is not forced diabatically but interacts with other layers through pressure.

not resolved in the two-layer model. The eastward current is connected to the continental slope region more directly than the two-layer model because the upper-most layer is less constrained by the topographic slope than the upper layer in the two layer model. However, it is still following the continental slope. To support a geostrophic flow in the upper layer from the open ocean to the entrainment region, the interface must tilt down southward due to the velocity shear between the upper layer and the lower layer. In the presence of slope, this interface tilt results in changing where the interface intersects with the bottom bathymetry, thus making the upper layer contact the bottom bathymetry. Therefore, a direct inflow from the open ocean region to the entrainment region in the upper layer cannot form and so the inflow is still likely to follow the bathymetric contours. An westward zonal jet that is analogous to the Azores Countercurrent forms near 38^o N with a transport of 2 Sv. This location is 1 degree further north compared to the two-layer model (Figure 3-2) but the transport is roughly the same.

The two- and three-layer models both show similar dynamical features of the topographic β-plume along the continental slope region and the Azores Current and the Azores Counter Current in the open ocean. This result shows that the upper layer response observed in the two-layer model is robust in the presence of stratification and not solely a product of poor vertical resolution.

3.4 Realistic continental slope: Revisiting Case 4

In this section, the flow field in Case 4 will be examined in detail and also compared against observations and other GCM calculations.

The Azores Current

The eastward zonal jet in Case 4 forms between 34–36^o N with a width of about 150 km, transport of about 4 Sv, and a maximum zonal velocity of 5 cm s^{-1}. The location of this eastward zonal jet is analogous to what is observed for the Azores Current (Klein and Siedler, 1989; Lozier et al., 1995; Fratantoni, 2001). The Azores

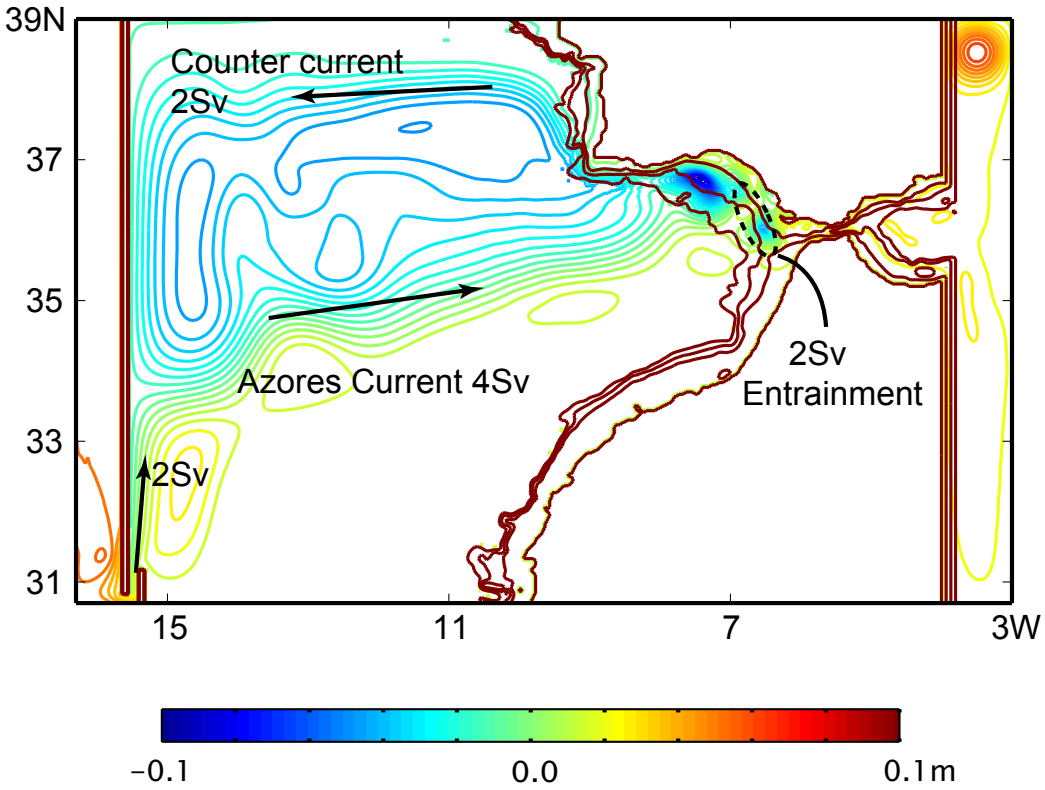

Figure 3-24: Time average of the sea surface height from the three layer model using realistic bathymetry in Figure 3-1. The contours are drawn from -10 to 10 cm with contour interval of 0.5 cm (same as Figure 3-2). The Azores Current in the interior formed with a Countercurrent to the north just like the two-layer model. The location of the Azores Current and the Counter Current appears to have shifted slightly to the south and north respectively but the transport remains the same for both the Azores Current (4.0 Sv) and the Azores Counter Current (2.0 Sv).

Current is also observed to exist between 32-35^o N in the middle of the subtropical gyre in the North Atlantic, with a width of 150 km, depth of 1000 m, transport of 7–8 Sv, and a maximum zonal velocity of 10 m s^{-1}. It is associated with a sharp frontal structure in the middle of the subtropical gyre which has a meridional length scale much larger than the Azores Current (Figure 1-3).

One difference between the eastward zonal jet in Case 4 and the Azores Current is the magnitude of the transport. The eastward zonal jet in Case 4 has a smaller transport (4 Sv) compared to what is observed for the Azores Current (7–13 Sv) (e.g. Klein and Siedler 1989; Alves et al. 2002). However, the observed value is in the middle of the basin (near 20-35^o W) and is an estimate far from the Gulf of Cadiz. The transport of the Azores Current that enters the Gulf of Cadiz is estimated to be about 4 Sv (Paillet and Mercier, 1997) and the remaining 3–9 Sv is thought to feed the Canary current, which is a southward flow along the coast of Africa (Klein and Siedler, 1989). The wind-driven gyre shows flow mostly in the meridional direction in the eastern North Atlantic (Figure 1-3) so a superposition of the wind-driven gyre and the topographic β-plume will not result in an enhancement of the eastward zonal transport. The hypothesis of the Azores Current as a branch of the topographic β-plume may explain the 4 Sv that is entering the Gulf of Cadiz, but appears to be unsuccessful on explaining why the transport is much more enhanced in the open ocean.

Another difference is the time variability. The eastward zonal jet in Case 4 is quite steady and only weak perturbations are observed. The time series of the velocity does reflect the planetary Rossby waves propagating to the west but its amplitude is very weak (Figure 3-10). However, the Azores Current is observed to be baroclinically unstable (Kielmann and Käse, 1987) with a meander of 100 km and a phase speed of 3 cm s^{-1} (Pingree et al., 1999), occasionally producing large eddies known as 'STORMS' (Pingree, 1997). What could be creating this difference? The primary reason is likely the poor vertical resolution of the model in the open ocean. The interface tilts upward to the north of where the eastward jet exists and makes the PV gradient of the overflow layer negative there, so with the PV gradient of the upper

layer remaining positive through the layer, the two layers do satisfy the necessary condition for baroclinic instability. However, the growth-rate of this instability in this two layer model is estimated to be about 800 days based on Phillips' model (Pedlosky, 1987), which is very slow. The actual growth-rate for the Azores Current, which is estimated to be about 2 days, is much smaller. Unless friction in the model is very small such that it would not damp the perturbation growth and that the model domain is very large such that the perturbation can fully grow within the domain, it is unlikely that instability of the eastward current is observed in the two-layer model. Additional calculation with more layers added into the model of Case 4, appears to show fluctuations of the Azores Current with smaller spatial scales and shows that steadiness of the eastward zonal jet in Case 4 is likely a result of poor vertical resolution.

The Azores Countercurrent

The westward zonal jet in Case 4 forms near 38^oN with a width of about 100 km, transport of about 2 Sv, and a maximum zonal velocity of 3 cm s^{-1} (Figure 3-25). The basic location and strength of this westward flow is analogous to the Azores Countercurrent, which is observed near 38^o N (see Section 1.4.3 for details). Although the origin and the transport of this current is still unclear, the study suggests the formation of such current as a branch of the topographic β-plume driven by the Mediterranean overflow. However, some have proposed that the countercurrent is an eddy-driven mean flow due to the eddies created by the Azores Current (Alves et al., 2002). This mechanism will result in forming two countercurrents north and south of the Azores Current whereas the topographic β-plume will only create a countercurrent to the north. The eddy-driven mechanism will also likely to be valid where the Azores Current is most unstable whereas the countercurrent created by the topographic β-plume will establish a westward flow that originates from the eastern boundary. These mechanisms may very well coexist, but the basic features of the Azores Countercurrent are not known in sufficient detail to discuss this further.

In Case 4, the topographic β-plume closed its circulation by creating a southward

flow at the western boundary located at about 800 km from the eastern boundary. However, the real western boundary in the Atlantic is located much further west. So if the ocean interior were quiescent, the topographic β-plume and the two zonal jets may extend to the coast of North America. The real ocean is unlikely to be quiescent, however, so the topographic β-plume is likely to close its circulation before reaching the western boundary. Sea surface height of the North Atlantic (Figure 1-3) also shows the signal of the Azores Current overwhelmed by the Gulf Stream in the western half of the North Atlantic. The mechanism that closes the topographic β-plume in the real ocean is not clear, but one might include the effect of wind stress at the sea surface. The topographic β-plume exists where the Ekman pumping velocity forced by the wind stress is negative and thus represents a negative PV forcing. This can force a southward flow that can close the cyclonic topographic β-plume in the open ocean. Though Ekman pumping is weak, it appears to have the correct sign and when integrated over a long zonal distance, it may be significant enough to close the topographic β-plume.

Circulation in the Gulf of Cadiz

The circulation in this region was compared to the observations in the previous chapter. Thus we will only briefly note the main points.

High time variability is observed in the northern half of the Gulf of Cadiz in Case 4 with cyclonic eddies outnumbering the anticyclonic eddies (Figure 3-2). The size and magnitude of these cyclonic eddies are similar to those observed at the surface adjacent to Meddies (Carton et al., 2002). However, whether these cyclonic eddies outnumber the anticyclonic eddies remains unclear. Time variability also observed in the overflow layer with a frequency of 7–8 days in the model is also similar to the 7–9 day frequency observed at the Portimão Canyon (Cherubin, 2003).

The time-mean cyclonic circulation within the Gulf of Cadiz matches with the result of (Mauritzen et al., 2001) where a cyclonic circulation is proposed from tracers and hydrographic sections. The circulation also matches with the recent result of the high-resolution model of Gulf of Cadiz of Peliz et al. (2006) (Figure 3-26) that shows

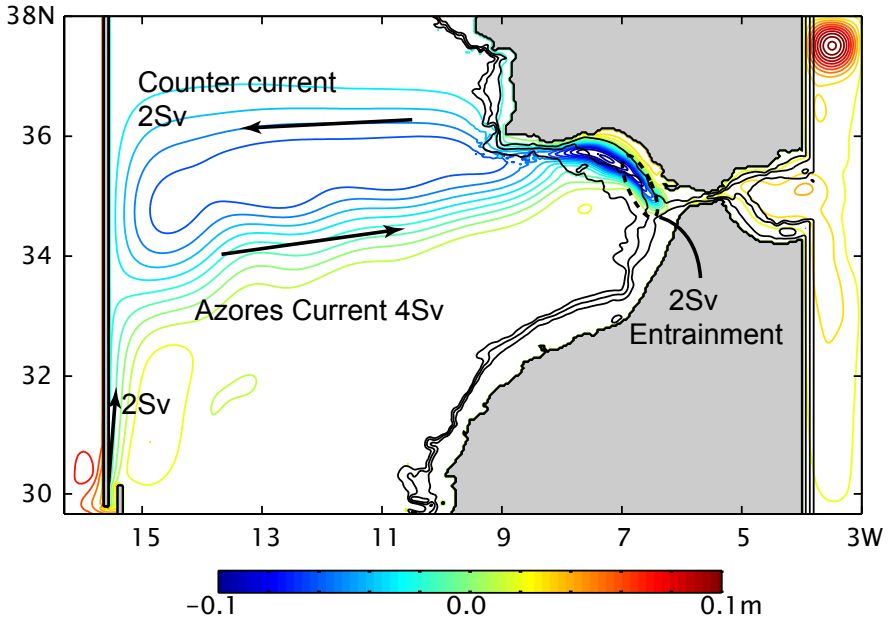

Figure 3-25: Time mean sea surface height of Case 4, where a two-layer model with a realistic bathymetry of the continental slope is used (Figure 3-1). Bottom bathymetry is contoured with black solid lines for 0, 300, 600, and 900 m depths where the upper layer directly contacts the sloping bottom. Entrainment of 2.0 Sv is specified to occur within the dotted region near the Strait of Gibraltar. The sea surface height is contoured in color from -10 to 10 cm every 0.5 cm just like the snapshot (Figure 3-2). A cyclonic topographic β-plume forms in the continental slope region and is connected to the open ocean, establishing an eastward zonal flow that is an analog of the Azores Current. The flow is between 34–36^o N with a transport of 4.0 Sv and 3.5 cm s^{-1} flowing into the Gulf of Cadiz from the Atlantic Ocean. The westward zonal flow, an analog of the Azores Counter Current, also forms between 36–38^o N with a transport of 2.0 Sv.

a cyclonic circulation in the Gulf of Cadiz with the Azores Current of 4.7 Sv and a westward flow of 2.1 Sv north of the gulf. The Azores Current is more directly connected to the continental slope region where entrainment presumably occurs, an effect of having stratification in the upper layer as shown in the previous section (Figure 3-24).

3.5 Summary

In this chapter, we have investigated whether the topographic β-plume, created by the overflow-upper ocean interaction, can become a basin scale flow. We tested this question specifically on the Mediterranean overflow in order to test whether the Mediterranean overflow is capable of driving the Azores Current. The results are summarized as follows:

1. The hypothesis of the Azores Current as a branch of the topographic β-plume driven by the Mediterranean overflow is plausible. The location and the transport of the eastward zonal jet that formed in the model experiment is similar to that of observations. The hypothesis explains why the location of the Azores Current is steady despite large seasonal fluctuations in the wind stress.

2. The topographic β-plume on the continental slope cannot connect to the open ocean unless friction, inertia, or eddies are strong enough to break the constraint as a result of the Taylor-Proudman theorem and establish a flow in the cross-slope direction. In the absence of stratification, the large difference of PV between the continental slope and open ocean regions prohibits a flow in the across-slope direction from forming.

3. The topographic β-plume driven by the Mediterranean overflow connects to the open ocean and establishes an eastward zonal jet because a region of steep slope exists near Cape St. Vincent. The eddies drive a mean flow across the slope in the steep slope region through eddy momentum flux, analogous to the effect of viscosity, and is allowing the topographic β-plume to connect into the open

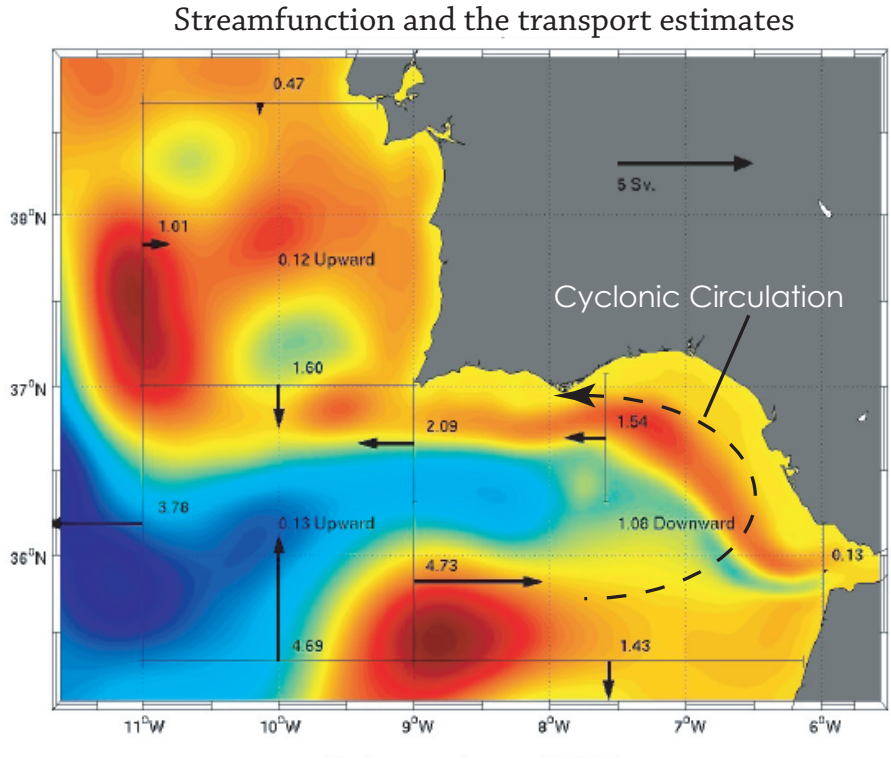

Figure 3-26: The stream function and the transport estimates between 20–600 m derived from high resolution (about 3 km) model calculation by Peliz et al. (2006) (personal communication) using ROMS (Haidvogel and Beckmann, 1999). The depth range is roughly above the Mediterranean overflow layer in most region of the Gulf so it will roughly show the behavior of the upper oceanic layer close to that of Case 4 (Figure 3-2). A cyclonic circulation is observed in the northern half of the Gulf of Cadiz. The eastward flow in the middle of the Gulf is the Azores Current, although the presence of large eddies in the open ocean distorts the zonal structure of the Azores Current. The Azores Current is about 4.7 Sv and the return flow is about 2.1 Sv. This return flow may include part of the Mediterranean overflow, however it shows that this on-shore region of the Gulf of Cadiz is flowing westward.

ocean there. This role of eddies in the slope transition region differs qualitatively from the cross-isopycnal momentum transfer occurring near the strait through baroclinic instability.

The next chapter contains the summary of the thesis and discussions.

Chapter 4

Summary and Discussion

Overflows are one of the major sources of the dense water of the global deep ocean and thus play a crucial role in the deep ocean circulation. To understand the basic dynamics of these overflows, past works simplified their dynamics by treating the overlying ocean as inactive. This simplification may be a first approximation for the overflow but certainly not for the overlying upper oceanic layer. Since entrainment is a PV forcing for the upper ocean, the upper ocean may respond to overflows with a circulation on a basin scale.

The goal of this thesis is to understand how the dynamics of the overflow and its overlying ocean are coupled. The outstanding questions are: How does the upper oceanic layer balance the mass loss caused by entrainment? How do the eddies created by baroclinic instability or other adiabatic layer interactions affect the overflow and upper ocean? Does the overflow have any basin scale impact to the upper ocean and is the Mediterranean overflow a plausible driving agent for the Azores Current? We examined these questions by first investigating the overflow-upper ocean interaction on the scale of the continental slope. We then examined the interaction on the scale of the ocean basin. The main approach was to examine the PV dynamics based on the concept of β-plumes.

4.1 What have we learned?

4.1.1 Continental Slope Scale

The overflow-upper ocean interaction on a continental slope was investigated using a two-layer isopycnal model with a constant slope and a parameter space close to that of the Faroe Bank Channel overflow. The diabatic and adiabatic effects were examined separately so that the dynamical effect of entrainment (diabatic) and baroclinic instability (adiabatic) can be examined separately. The results can be summarized as follows.

Upper Oceanic Layer

A local entrainment in the open ocean is known to drive a circulation known as β-plumes (Stommel, 1982). We have found that entrainment by overflows can also drive a β-plume in the upper oceanic layer in the continental slope region. This circulation was cyclonic and was aligned with the bathymetric contours since the background PV gradient in the continental slope region is the topographic β^* not the planetary β. The local stretching effect by entrainment drove a flow up the slope (up the PV gradient) in the upper layer and established this cyclonic circulation. The transport of this topographic β-plume, V, matched reasonably well with the estimate from the mean linear vorticity balance in the entrainment region, $\frac{V}{W} = \frac{f}{\beta^* L}$, where W is the entrainment transport and L is the cross-slope length of the entrainment region. Unlike the planetary β-plume (Spall, 2000), V was only two-three times larger than W because the topographic β was about two orders of magnitude larger than the planetary β.

In the absence of entrainment, the upper layer flow was dominated by eddies, similar to the laboratory experiment of Etling et al. (2000). The formation of these eddies was likely due to baroclinic instability. The location of where instability occurred depended on μ, the ratio of the overflow thickness gradient compared to the slope, consistent with the solution of Swaters (1991). The eddies were found to create an eddy thickness flux such that the potential energy of the flow is reduced. The role

of these eddies, formed through baroclinic instability, was also to transfer momentum from the overflow layer to the upper oceanic layer through form drag. As a result of this momentum transfer, these eddies are capable of generating an eddy-driven topographic β-plume above the overflow in the time-mean with a transport comparable to the overflow. We have found that this circulation was a double gyre since the eddies created two regions of eddy PV flux divergence having opposite signs.

When both entrainment and baroclinic instability were present, the transient flow field was dominated by the eddies. But in the time-mean, a cyclonic topographic β-plume established along the continental slope with a transport that roughly matched the estimate from the linear vorticity balance in the entrainment region. The entrainment-driven topographic β-plume appeared to be dominant over much of the continental slope region. However, the eddy-driven topographic β-plume was also observed near the strait. Because of the intense baroclinic instability occurring near the strait, the eddies were significant enough to affect the PV balance and establish a double-gyre circulation there. The experiment showed that that the upper layer is significantly affected by the overflow through both entrainment and baroclinic instability.

Overflow Layer

The overflow layer spreads and descends the continental slope because of bottom friction (Smith, 1975) and baroclinic instability (Jiang and Garwood, 1996). Unlike a single-layer (stream-tube) model, having an active upper layer changed the transient behavior of the overflow layer considerably. The overflow layer was found to form into a chain of anticyclonic eddies rather than a stream-tube-like flow when baroclinic instability developed. The temperature, velocity and transport of the overflow thus fluctuated with a frequency of about five days, analogous to the time variability that was observed for the Faroe Bank Channel and Mediterranean overflow (Stanton, 1983; Høyer and Quadfasel, 2001). The mean pathway of the overflow layer was found to increase its angle of descent from the frictional Ekman number when baroclinic instability occurred. This was because the instability transferred momentum and

energy from the overflow to the upper layer. Having an active upper layer introduced an additional momentum and energy sink for the overflow layer compared to a single-layer model where momentum loss is by bottom friction alone.

The outstanding question remaining is what sets the strength of the topographic β-plume. The experiments done in this chapter focused on the physical parameter space close to that of the Faroe Bank Channel but the competition of whether entrainment-driven topographic β-plume dominates or the eddy-driven topographic β-plume dominates in the continental slope region is likely to change as the physical parameter space changes.

4.1.2 Basin Scale

The overflow-upper ocean interaction was investigated on a basin scale using, again, a two-layer isopycnal model but now with a continental slope region and an open ocean region. The continental slope region was located on the eastern boundary of the open ocean region. This setup was used to test whether the topographic β-plume can become a basin scale flow in the presence of the open ocean and whether the Mediterranean overflow, located on the eastern boundary of the Atlantic, is a plausible driving agent for the Azores Current.

The Upper Oceanic Layer

The numerical model using realistic bathymetry of the continental slope near Gulf of Cadiz showed that the hypothesis of the Mediterranean overflow as the primary driving agent for the Azores Current is plausible. The topographic β-plume driven by the Mediterranean overflow connected to the Atlantic Ocean and established a steady eastward zonal jet between 34–36^o N with a transport of 4.0 Sv, analogous to the Azores Current (Klein and Siedler, 1989; Paillet and Mercier, 1997). A westward zonal jet also established to the north with a transport of 2.0 Sv, analogous to the Azores Countercurrent (Onken, 1993).

To illustrate the dynamics responsible for connecting the topographic β-plume

to the open ocean, we showed three model experiments using an idealized bottom bathymetry. When the continental slope was a constant gentle slope (0.01), the topographic β-plume was trapped along the continental slope region, similar to that of the numerical model result where no open ocean region existed. The large difference of PV between the continental slope and open ocean regions prohibited a flow in the across-slope direction from forming (Taylor-Proudman Theorem) (Brink, 1998). When the continental slope was a constant gentle slope (0.01) but with an addition of a curvature on the scale of the Gulf of Cadiz, the topographic β-plume was still unable to connect to the open ocean. The Rossby number of the flow was small for the flow to overshoot at the curvature and connect the topographic β-plume to the open ocean (Klinger, 1994) . When the continental slope varied its slope from gentle to steep, the topographic β-plume connected to the open ocean and established a eastward zonal jet in the open ocean. From these three experiments, we found that the existence of the steep slope region is a crucial factor on connecting the topographic β-plume to the open ocean.

In the transition region from gentle to steep slope, the eddies were found to flux momentum down the gradient of the mean flow. This momentum flux is within the isopycnal layer and its effect on the mean flow was roughly parameterizable by a viscosity-like term. The role of eddies in the slope transition region thus differs qualitatively from the cross-isopycnal momentum transfer occurring near the strait through baroclinic instability. The reason why the steep slope region was a crucial factor on connecting the topographic β-plume to the open ocean was that the effect of this eddy viscosity ($\frac{A_H}{\beta^*}$) increased considerably as the slope increased (Csanady, 1978). Thus the topographic β-plume crossed the bathymetric contours at a steeper angle as the slope increased and made the topographic β-plume capable of connecting to the open ocean within a short length scale. The abrupt transition from gentle to steep slope also confined this off-shore diffusion to work within a short meridional length scale such that the topographic β-plume connects to the open ocean as a narrow zonal jet. For the topographic β-plume driven by the Mediterranean overflow, the abrupt increase in the continental slope from Gibraltar strait to Cape St. Vincent was

what made the topographic β-plume connect to the open ocean. Thus the eastward zonal jet formed in the open ocean close to the latitude of the Gibraltar Strait and with a narrow width, approximately 150 km, similar to that of the Azores Current.

The Overflow Layer

When the Mediterranean overflow descended the continental slope of the Gulf of Cadiz, baroclinic instability developed and anticyclonic eddies formed. After reaching the depth of 900m, it flowed basically along the continental slope of Portugal. Inertia was not strong enough to make this flow create Meddies and enter the open ocean region near Cape St. Vincent. The thick lower layer in the open ocean decreased the velocity and inertia of the flow significantly such that Meddies could not form. Since the numerical model had a wall at the northern boundary instead of an open boundary, the overflow flowing northward along the continental slope turned west and entered the open ocean region there.

There are two outstanding questions remaining. The first question is on the strength of the Reynolds Stress that fluxes momentum down the mean where the slope transition occurs. What process is responsible for creating such a large effective viscosity? The second question is on the transition of the slope from gentle to steep. How would the width of the zonal flow be affected when the rate of slope transition and the location of this slope transition change independently? Answering these two problems will lead to more complete understanding on the role of the varying slope on connecting the topographic β-plume to the open ocean interior.

4.2 Future Works

The numerical model used in this thesis was simplified for the purpose of trying to understand the basic process of overflow-upper ocean interaction. It, therefore, lacked many features that exist in the real ocean, which may affect the results of this thesis work. One obvious feature is that the amount of entrainment is prescribed in the numerical model. Entrainment, of course, depends on the dynamics and is a area

of intensive research. Here, we raise three other possible areas for extension: the effect of stratification on the topographic β-plume, flow into the marginal sea, and the wind-stress at the sea surface. We will be examine these effects specifically on the topographic β-plume driven by the Mediterranean overflow.

Stratification

The upper oceanic layer was represented as one-layer in this thesis but obviously, stratification exists in the real ocean. Depending on the stratification of the water above the overflow layer, the topographic β-plume may not extend up to the sea surface. The transport of the topographic β-plume may reduce from what is estimated by Eq 1.5, since this estimate assumes that the upper ocean is one layer. To examine the detailed effect of stratification on the topographic β-plume, the entrainment needs to be parameterized so that it can occur in various density spaces. But here, we will use scaling arguments instead to discuss whether the topographic β-plume may influenced by the stratification.

The Burger number, $\left(\frac{L_D}{L}\right)^2$, can tell us the importance of stratification in the presence of earth's rotation, where L_D is the deformation radius and L is the length-scale of entrainment (Tritton, 1988). A Taylor Column is likely to be vertically trapped by stratification when this Burger number is larger than one but a Taylor Column will likely persist throughout the layer when the Burger number is less than one. For the Mediterranean overflow, the deformation radius is about 20 km in the upper oceanic layer and the entrainment region size is about 30 km. So the Burger number is about 0.4, less than one, but not negligibly small implying that the Taylor Column may extend to the sea surface with its signal somewhat reduced. Thus the effect of stratification may not be entirely negligible on the topographic β-plume driven by the Mediterranean overflow. Thus the transport of the topographic β-plume may be less than the transport observed in Chapter 3.

The flow into the Mediterranean Sea

Next, we will examine the effect of having an upper layer flow into the marginal sea (sill-exchange flow). This sill-exchange flow was not reproduced in the model experiments in Chapter 2 or 3 for the purpose of highlighting the downstream effect of overflows on the upper ocean dynamics.

A transport of about 1.0 Sv enters the Mediterranean Sea from the Atlantic in the upper layer to balance the Mediterranean overflow exiting the Mediterranean Sea into the Atlantic below (Bryden and Stommel, 1984). This sill-exchange flow is likely to affect the north-westward branch of the topographic β-plume but not the east-southward branch. When a sill-exchange flow is included into the two-layer model with a realistic topography [1], an eastward zonal jet of 4.0 Sv and a westward flow of 1.0 Sv forms in the open ocean (Figure 4-1). The transport of the eastward jet is similar to that observed in Case 4 (Figure 3-2), but the transport of the westward zonal jet decreases 1.0 Sv.

The decrease in the transport of the westward zonal jet can be explained by the change in the PV balance of the entrainment region. Without the sill-exchange flow, the PV forcing (entrainment) is balanced only by the two jets along the PV contours (Figure 1-5). But in the presence of the sill-exchange flow, the sill-exchange flow can serve as the second branch of the PV outflow (Figure 4-2a) and therefore, the transport of the in-shore (north-eastward) jet will decrease (Figure 4-1). However, this decrease in transport may be just a consequence of the two-layer model not resolving enough stratification in the upper layer. Because sill-exchange flow occurs over shallower and lighter density layers than the water masses that are entrained into the Mediterranean overflow, the sill-exchange flow may drive a flow along the shallower region of the continental slope and the topographic β-plume located off-shore may be left unaffected (Figure 4-2b). Although this effect of the sill-exchange flow on the topographic β-plume will need to be tested in a model with stratification

[1] The stratification is also too weak to reproduce the realistic interface tilt at the sill. When using $\Delta\rho = 0.05\text{kg m}^{-3}$, the value used in Case 4, for the density difference between the overflow and the upper layer, the interface between the overflow and the upper layer outcrops at the surface in order to support the large shear between the two layers, which is unrealistic.

in the upper layer, the transport of the off-shore (east-southward) jet is unlikely to be affected by the sill-exchange flow because these two flows are located on PV contours with significant PV difference.

The Wind-driven Gyre and the Azores Current

Perhaps the biggest feature that is missing in our numerical model, when testing the basin scale influence of the topographic β-plume driven by the Mediterranean overflow, is the subtropical gyre in the Atlantic. This circulation may affect and interact with the topographic β-plume on a very large scale in the open ocean.

The transport of the Azores Current that enters the Gulf of Cadiz is estimated to be about 4.0 Sv (Paillet and Mercier, 1997), a value close to the model results shown in Chapter 3 (4.0 Sv). However, the transport is observed to be 7.0–13.0 Sv in the open ocean (Klein and Siedler, 1989; Gould, 1985) between 22-30^o W, which is more than what enters the Gulf of Cadiz. Although time variability and the difference in the definition of the Azores Current may possibly change these transport values, it appears that the Azores Current has a larger transport than 4.0 Sv in the open ocean. We know from observations that the 3.0–9.0 Sv is likely feeding the Canary Current, a coastal current along the coast of North Africa. But how could this difference of 3.0–8.0 Sv be a result of the interaction between the topographic β-plume and the wind-driven gyre? The sea surface height, from observations (Jayne, 2006) and data assimilation (Gebbie, 2004) shows fairly straight meridional contour lines in the eastern Atlantic outside the Azores Current, indicating that the Sverdrup interior is meridional. So a superposition of the topographic β-plume shown in this thesis (Figure 3-2) and the wind-driven subtropical gyre will not increase the zonal transport of the eastward jet in the open ocean. The effect of the topographic β-plume is only to create a sharp zonal kink to the sea surface height and not to enhance the zonal transport. The question of why the Azores Current has a transport of about 8.0–13.0 Sv in the open ocean appears to be still an open question. Further investigation on whether this transport can be explained by the interaction between the topographic β-plume and the subtropical gyre may lead to a more complete understanding of the

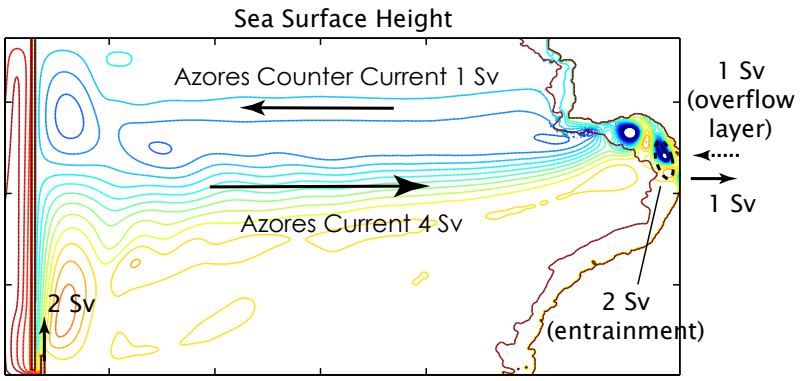

Figure 4-1: The sea surface height of the two-layer model when there is 1 Sv of upper layer flow from the Atlantic to the Mediterranean Sea at the Gibraltar Strait. This sill-exchange flow is prescribed as a lateral mass flux. However, the Mediterranean Sea is excluded and the open ocean region is extended west so that the flow field in the open ocean is better observed. All other forcing is exactly the same as Case 4. A topographic β-plume forms along the continental slope and is connected to the open ocean, forming an eastward zonal jet of 4.0 Sv that is analogous to the Azores Current. A westward zonal jet exists to the north with a transport of 1.0 Sv is analogous to the Azores Counter Current. The transport of this branch decreased from 2.0 Sv compared to Case 4.

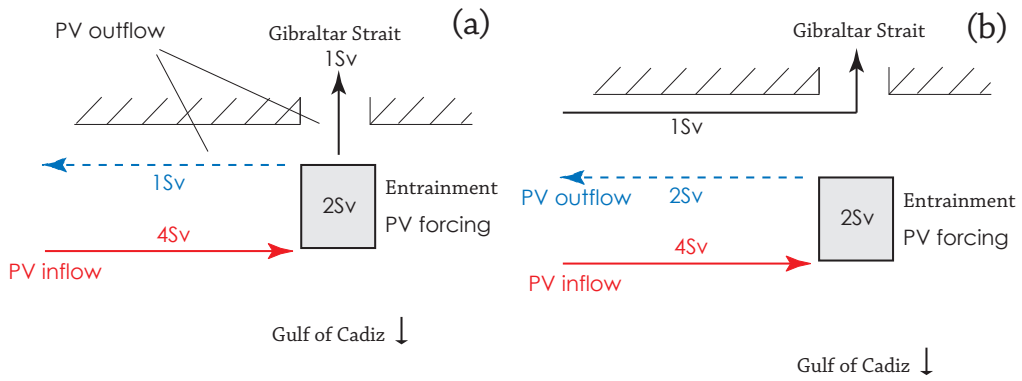

Figure 4-2: A schematic of the PV balance in the continental slope region. The Gibraltar Strait is the opening at the top and the Gulf of Cadiz is located at the bottom. **(a)** One scenario of the PV balance when a sill-exchange flow exists. The PV source is balanced by the PV influx by the off-shore (east-southward) jet and the PV out-flux by the on-shore (north-westward) jet and the sill-exchange flow. Compared to the PV balance where sill-exchange flow does not exist, the westward zonal jet is required to flux less PV out of the PV source region thus, the mass transport of the westward zonal jet decreases. **(b)** Second scenario of the PV balance. The sill-exchange flow is located on a shallower region far from the shallowest point of the entrainment region. Thus, the sill-exchange flow and the topographic β-plume do not affect each other strongly. Thus the in-shore jet is kept to 2 Sv.

upper ocean circulation in the North Atlantic Ocean.

4.3 Discussion

4.3.1 The topographic β-plumes driven by major overflows

We have found that the Mediterranean overflow is capable of influencing the upper ocean on a basin scale through the mechanism of topographic β-plume. But can we expect similar results for other major overflows, such as Faroe Bank Channel, Denmark Strait, Filchner Bank and Red Sea overflows? The transport of the topographic β-plume likely to be driven by each of these overflows can be roughly estimated from Eq 1.5 but whether these topographic β-plumes can extend to the open ocean will depend on the planetary location of each overflows. This is because the way the PV contours in the slope region connect with those in the open ocean region is a crucial factor in determining whether the topographic β-plume can extend to the open ocean or not. In this subsection, we will examine how the planetary location influences the topographic β-plume by focusing on each of the major overflows. We will also examine the effect of stratification as we estimate the transport of the topographic β-plume.

The Faroe Bank Channel overflow is estimated to drive a topographic β-plume with a transport of about 5.8 Sv (Case 1, Figure 2-1 and Table 4.1). The deformation radius is about 13 km in the upper layer of this region and the entrainment region size is about 30 km. So the Burger Number is 0.2, less than one. The topographic β-plume driven by the Faroe Bank Channel overflow is likely to persist throughout the overlying oceanic layer with some modification by the stratification. So the transport of 5.8 Sv is likely within a reasonable estimate. Since this topographic β-plume forms on the northeast corner of the open ocean, it is possible for this topographic β-plume to become a basin scale circulation. However, the continental slope of this region remains roughly zonal until it encounters the steep continental slope of Iceland and Reykjanes Ridge about 600km west of the Faroe Bank Channel (Figure 1-7). So the

continental slope of where the Faroe bank Channel overflow is located is similar to a slope on a northern boundary rather than an eastern boundary. Therefore, the PV contours of the slope region coincide with that of the planetary PV contours (zonal) and the topographic β-plume is likely to be trapped within the Faroe Islands and the Reykjanes Ridge. This cyclonic topographic β-plume between the Faroe Islands and the Reykjanes Ridge is analogous to the cyclonic circulation observed in the region (Lavender et al., 2005). However, the background sub-polar gyre may also induce a similar cyclonic gyre in the region. Further detailed observations will be necessary for more detailed comparison.

The Denmark Strait, Filchner Bank overflows are estimated to drive topographic β-plumes with a transport of about 7.6 and 9.6 Sv respectively (Table 4.1). The stratification of the upper ocean in both regions are weak with the deformation radius of about 6 km for the Denmark Strait and 7 km for the Filchner Bank. The entrainment region is about 30 km for both overflows so the Burger number is 0.04, much less than one. Both topographic β-plumes are likely to persist throughout the overlying oceanic water with a transport as shown above. However, these overflows exist on the western boundary of the open ocean. Therefore, although the transport estimates of the topographic β-plumes are of significant size, the turbulent western boundary currents may still overwhelm these flows and make the circulation hard to observe in the ocean. Moreover, for the Filchner Bank overflow, because there is no open ocean region west for the topographic β-plumes to escape to, the induced topographic β-plume is likely to be trapped within the continental slope region even if they do exist. However, for the Denmark Strait overflow, if the topographic β-plume manages to exist and flow along the continental slope of Greenland, there is a possibility that it will extend into the Labrador Sea and become a basin scale flow there. This remains an open question and needs to be tested with a model that is close to the Denmark Strait and the continental slope of Greenland.

The Red Sea overflow is estimated to drive a topographic β-plume with a transport of about 0.5 Sv. This transport is of order one smaller than other topographic β-plumes because the transport of the entrainment is also an order one smaller compared

Location	Entrainment (Sv)	Coriolis parameter (s^{-1})	Slope	Depth of Entrainment (m)	β-plume transport (Sv)
Mediterranean Sea	2.0	8.4×10^{-5}	0.012	300-600	4.0
Faroe Bank Channel	1.5	1.3×10^{-4}	0.015	700-1000	5.8
Denmark Strait	2.3	1.2×10^{-4}	0.028	600-1000	7.5
Red Sea	0.25	3.1×10^{-5}	0.006	300-600	0.5
Filchner Bank	4.0	1.4×10^{-4}	0.032	700-1200	9.6

Table 4.1: The parameter space for the five major overflows in the Atlantic. The transport of the topographic β-plume driven in the upper layer is estimated from the linear vorticity balance (Eq 2.12). L_x, the across slope length scale of the entrainment region, is determined from the slope (α) and the depth of entrainment δh by $L_x = \frac{\delta h}{\alpha}$ and H is determined by the maximum depth of entrainment. This table is generated from Observationalists' Table of Plumes from Climate Process Team (http://cpt-gce.org/index.htm)

to other overflows. However, since the entrainment occurs within a channel of about 5 km this is much smaller than the deformation radius of the area, which is about 50 km (Özgökmen et al., 2003). The dynamics of the upper layer is thus unlikely to be governed by the rotation of the earth (f). The topographic β-plume is unlikely to form at all.

Among the five major overflows in the Atlantic, the Mediterranean overflow appears to be the only overflow than can drive an upper ocean circulation on a basin scale.

4.3.2 A remark on parameterizing overflow dynamics in GCMs

The eastward zonal jet shown in the GCM calculation of Jia (2000) served as one of the motivations for investigating the overflow-upper ocean interaction in this thesis. But now, with our understandings of the basic overflow-upper ocean interaction, we can try to answer why an eastward zonal jet formed in her model when the detailed dynamics of the overflow-upper ocean interaction were not explicitly resolved. The dynamics of the Mediterranean overflow were parameterized in the model by relaxing the hydrography in the Gulf of Cadiz to Levitus (1982) climatology (sponge layer). This resulted in a mass transformation from the upper oceanic layer to the deep

layer within the Gulf of Cadiz. The upper layer likely balanced this entrainment by creating a β-plume (Özgökmen et al., 2001) that has eastward and westward zonal jets at locations analogous to the Azores Current and the Azores Countercurrents respectively. The transport of the eastward jet in the model was also close to what is observed near 30^o W. However, the transport of the two zonal jets were as much as 20.0 Sv near the Gulf of Cadiz, which is significantly larger than what is observed to enter the Gulf of Cadiz (4.0 Sv) (Paillet and Mercier, 1997). We suspect the large transport values to be a result of the low resolution used in the GCM. The resolution of 1/3 of a degree is inefficient to resolve the detailed feature of the bottom slope and the small spatial scale of where entrainment occurs. Provided that the amount of entrainment is correctly resolved, a model is required to have a resolution of at least 10 km or about $\frac{1}{10}$ of a degree to resolve the entrainment region that is about 30 km $\times$ 60 km. Since the transport of the topographic β-plume is sensitive to the length-scale and the background PV gradient of the entrainment region (Eq 1.5), when these two features are poorly represented in the model, the β-plume induced in the upper ocean is also likely to be poorly reproduced. Unless these features are resolved, the model may only capture the mass balance but not the PV balance.

The current state-of-the-art climate models have difficulties reproducing the observed density, temperature, and salinity structure in the region where overflows water are thought to be advected (Gnanadesikan et al., 2006) and parameterization of overflows has been a topic of intensive research (Hallberg, 2000; Legg et al., 2006). This thesis shows that overflows can induce a significant circulation in the upper oceanic layer and so the parameterization of overflows must be associated with parameterization of its affect on the dynamics in the upper layer, at least in terms of the mass and PV balance. This is especially true for the Mediterranean overflow where the effect of the overflow on the upper layer could be on the basin scale. For other major overflows, the upper layer influence may be either regional or negligible as described in the previous subsection. Since GCMs are likely to have low resolution such that the dynamics of the Mediterranean overflow are poorly resolved, it is unlikely that the effect of the overflow layer on the upper ocean is correctly represented. This

study suggests that the strength of the vortex stretching on the upper layer needs be associated with the parameterization of overflows in GCMs. Therefore, the effect of the overflow on the upper layer, to the first order, may be parameterizable by either specifying the horizontal transports of the two jets of topographic β-plume determined from Eq 1.5 or by specifying the magnitude of stretching (the RHS of Eq 1.5) where entrainment occurs.

In this thesis, the overflows were shown to have a large scale impact on the upper ocean through the formation of the topographic β-plume. The Mediterranean overflow was also shown to be capable of driving the Azores Current, through this mechanism of β-plumes. The existence of the Azores Current plays an important role on the subduction process of the subtropical gyre in the North Atlantic (New et al., 2001), which influences climate on a shorter time scale than the deep ocean circulation. So the hypothesis of the Mediterranean overflow driving the Azores Current also indicate the relevance of the Mediterranean overflow to climate on a shorter time scale. With proper representation of the Mediterranean overflow in GCMs, we may then be able to address the role of overflows in the climate system on various time scales.

Bibliography

Adcock, S. and D. Marshall, 2000: Interactions between geostrophic eddies and the mean circulation overf large-scale bottom topography. *J. Phys. Oceanogr.*, **30**, 3223–3238.

Aiki, H. and T. Yamagata, 2004: A numerical study on the successive formation of meddy-like lenses. *J. Geophys. Res.*, **109**, doi:10.1029/2003JC001952.

Alves, M. and A. Colin De Verdiere, 1999: Instability dynamics of a subtropical jet and application to the azores front current system: Eddy-driven mean flow. *J. Phys. Oceanogr.*, **29**, 837–864.

Alves, M., F. Gaillard, M. Sparrow, M. Knoll, and S. Giraud, 2002: Circulation patterns and transport of the azores front-current system. *Deep-Sea Res. II*, **49**, 3983–4002.

Ambar, I. and M. Howe, 1979a: Observations of the mediterranean outflow. i. mixing in the mediterranean outflow. *Deep-Sea Res.*, **26**, 535–554.

— 1979b: Observations of the mediterranean outflow. ii. the deep circulation in the vicinity of the gulf of cadiz. *Deep-Sea Res.*, **26**, 555–568.

Baringer, M. and J. Price, 1997: Mixing and spreading of the mediterranean outflow. *J. Phys. Oceanogr.*, **27**, 1654–1677.

Borenäs, K. and P. Lundberg, 2004: The faroe-bank channel deep-water overflow. *Deep-Sea Research II*, **51**, 335–350.

Bower, A. S., L. Armi, and I. Ambar, 1997: Lagrangian observations of meddy formation during a medditerranean undercurrent seeding experiment. *J. Phys. Oceanogr.*, **27**, 2545 – 2575.

Bracco, A. and J. Pedlosky, 2003: Vortex generation by topography in locally unstable baroclinic flows. *J. Phys. Oceanogr.*, **33**, 207–219.

Brink, K., 1998: Wind-driven currents over the continental shelf. *The Sea,*, **10**, Chapter1.

Bryden, H., J. Candela, and T. Kinder, 1994: Limiting processes that determine basic features of the circulation in the mediterranean sea. *Prog. Oceanog.*, **33**, 201–248.

Bryden, H. and T. Kinder, 1991: Steady two-layer exchanve through the strait of gibraltar. *Deep Sea Res.*, **38**, S445.

Bryden, H. and H. Stommel, 1984: Limiting processes that determine basic features of the circulation in the mediterranean sea. *Oceanologica Acta*, **7**, 289–296.

Candela, J., 2001: Mediterranean water and global circulation. *Ocean Circulation and Climate*, pp. 419429.

Carton, X., L. Chérubin, J. Paillet, Y. Morel, A. Serpette, and B. L. Cann, 2002: Meddy coupling with a deep cyclonie in the gulf of cadiz. *J. Marine System*, **32**, 13–42.

Chérubin, L., X. Carton, J. Paillet, Y. Morel, and A. Serpette, 2000: Instability of the mediterranean water undercurrents southwest of portugal: effects of baroclinicity and of topography. *Oceanologica Acta*, **23**, 551–573.

Chérubin, L., N. Serra, and I. Ambar, 2003: Low-frequency variability of the mediterranean undercurrent downstream of portimão canyon. *J. Geophys. Res.*, **108**, 3058, doi:10.1029/2001JC001229.

Csanady, G., 1978: The arrested topographic wave. *J. Phys. Oceanogr.*, **8**, 47–62.

Etling, D., F. Gelhardt, U. Schrader, F. Brennecke, G. Kuhn, G. C. d'Hieres, and H. Didelle, 2000: Experiments with density currents on a sloping bottom in a rotating fluid. *Dyn of Atmos. and Oceans*, **31**, 139–164(26).

Ezer, T., 2006: Topographic influence on overflow dynamics: Idealized numerical simulations and the faroe bank channel overflow. *J. Geophys. Res.*, **111**, C02002, 10.1029/2005JC003195.

Fratantoni, D. M., 2001: North atlantic surface circulation during the 1990's observed with satellite-tracked drifters. *Journal of Geophysical Research,*, **106**, 22067–22093.

Gebbie, G., 2004: *Subduction in an Eddy-Resolving State Estimate of the Northeast Atlantic Ocean*. Ph.D. thesis, MIT/WHOI Joint Program.

Gnanadesikan, A., S. Griffies, K. Dixon, V. Balaji, M. Barreiro, J. Beesley, W. Cooke, T. Delworth, J. Dunne, R. Gerdes, M. Harrison, I. Held, W. Hurlin, H. Lee, Z. Liang, G. Nong, R. Pacanowski, A. Rosati, J. Russell, B. Samuels, M. Spelman, C.Sweeney, R. Stouffer, G. Vecchi, M. Winton, A. Wittenberg, F. Zeng, and R. Zhang, 2006: Gfdl's cm2 global coupled climate models-part 2: The baseline ocean simulation. *J. Climate*, **19**, 675–697.

Gould, W., 1985: Physical oceanography of the azores front. *Prog. Oceanog.*, **14**, 167–190.

Haidvogel, D. and P. Rhines, 1983: Waves and circulation driven by oscillatory winds in an idealized ocean basin. *Geophys. Astrophys.Fluid Dynamics*, **25**, 1–63.

Haidvogel, D. B. and A. Beckmann, 1999: Numerical ocean circulation modeling. *Imperial College Press*.

Hallberg, R., 1997: Stable split time steeping schemes for large-scale ocean modeling. *J. Comp. Phys*, **135**, 54–65.

— 2000: Time integration of diapycnal diffusion and richardson number dependent mixing in isopycnal coordinate ocean models. *Mon. Wea. Rev.*, **128**, 1402–1419.

Helfrich, K., 2006: Nonlinear adjustment of a localized layer of buoyant, uniform, potential vorticity fluid against a vertical wall. *Dyn of Atmos. and Oceans*, accepted.

Høyer, J. L. and D. Quadfasel, 2001: Detection of deep overflows by satellite altimetry. *Geophys Res. Letter*, **28**, 1611–1614.

Høyer, J. L., D. Quadfasel, and O. Anderson, 2002: Deep ocean currents detected with satellite altimetry. *Canadian Journal of Remote Sensing*, **28**, 556–566.

Jayne, S. R., 2006: Circulation of the north atlantic ocean from altimetry and the gravity recovery and climate experiment geoid. *Journal of Geophysical Research*, **111**, C03005, doi:10.1029/2005JC003128, Reproduced/modified by permission of the author and American Geophysical Union.

Jia, Y., 2000: The formation of an azores current due to mediterranean overflow in a modeling study of the north atlantic. *J. Phys. Oceanogr.*, **30**, 2342–2358.

Jiang, L. and R. Garwood, 1996: Three-dimensional simulations of overflows on continental slopes. *J. Phys. Oceanogr.*, **26**, 1214–1233.

Käse, R. and G. Siedler, 1996: *The Warmwater Sphere of the North Atlantic Ocean, W. Krauss Ed.*, Gebrüder Borntraeger, chapter The Gulf Stream, the North Atlantic Current, and the origin of the Azores Current. 291–331.

Kielmann, J. and R. Käse, 1987: Numerical modeling of meander and eddy formation in the azores current frontal zone. *J. Phys. Oceanogr.*, **17**, 529–541.

Klein, B. and G. Siedler, 1989: On the origin of the azores current. *Journal of Geophysical Research*, **94**, 6159–6168.

Klinger, B., 1994: Inviscid current separation from rounded capes. *J. Phys. Oceanogr.*, **24**, 1805–1811.

Lavender, K., W. Owens, and R. Davis, 2005: The mid-depth circulation of the subpolar north atlantic ocean as measured by subsurface floats. *Deep-Sea Research I*, **52**, 767–785.

Legg, S., R. Hallberg, and J. Girton, 2006: Comparison of entrainment in overflows simulated by z-coordinate, isopycnal and non-hydrostatic models. *Ocean Modeling*, **10**, 69–97.

Levitus, S., 1982: Climatological atlas of the world ocean. noaa prof. paper no. 13. *U.S. Government Printing Office*, 173pp.

Lozier, M., W. B. Owens, and R. Curry, 1995: The climatology of the noarth atlantic. *Prog. Oceanog.*, **36**, 1–441.

Mauritzen, C., Y. Morel, and J. Paillet, 2001: On the influence of mediterranean water on the central waters of the north atlnatic ocean. *Deep Sea Res. I*, **48**, 347–381.

Mauritzen, C., J. Price., T. Sanford, and D. Torres, 2005: Circulation and mixing in the faroese channels. *Deep-Sea Res. I*, **52**, 883–913.

New, A., Y. Jia, M. Coulibaly, and J. Dengg, 2001: On the role of the azores current in the ventilation of the north atlantic ocean. *Prog. Oceanog.*, **48**, 163–194.

Nof, D., 1983: The translation of isolated cold eddies along a sloping bottom. *Deep-Sea Res.*, **30**, 171182.

Ochoa, J. and N. Bray, 1991: Water mass exchange in the gulf of cadiz. *Deep-Sea Res.*, **38 Suppl 1**, 5465–5503.

Onken, R., 1993: The azores countercurrent. *J. Phys. Oceanogr.*, **23**, 1638–1646.

Orsi, A. H., G. C. Johnson, and J. L. Bullister, 2000: Circulation, mixing, and production of antarctic bottom water. *Prog. Oceanog.*, **43**, 55–109.

Orvik, K. and P. Niiler, 2002: Major pathways of atlantic water in the northern north atlantic and nordic seas toward arctic. *Geophys. Res. Let.*, **29(19)**, 1896, doi:10.1029/2002GL015002.

Özgökmen, T., E.P.Chassignet, and C. Rooth, 2001: On the connection between the mediterranean outflow and the azores current. *J. Phys. Oceanogr.*, **31**, 461–480.

Özgökmen, T., W. E. Johns, H. Peters, and S. Matt, 2003: Turbulent mixing in the red sea outflow plume from a high-resolution nonhydrostatic model. *J. Phys. Oceanogr.*, **33**, 1846–1869.

Paillet, J. and H. Mercier, 1997: An inverse model of the eastern north atlantic general circulation and thermocline ventilation. *Deep Sea Res. I*, **44**, 1293–1328.

Pedlosky, J., 1974: Longshore currents, upwelling and bottom topography. *J. Phys. Oceanogr.*, **4**, 214–226.

— 1987: *Geophysical Fluid Dynamics*, volume 710pp. Springer-Verlag, Berlin.

Peliz, A., J. Teles-Machado Dubert, and P. Marchesiello, 2006: Surface circulation in the gulf of cadiz and southwest of iberia. part i: Model and mean flow structure. *In preparation*.

Pingree, R., 1997: The eastern subtropical gyre (north atlantic): Flow rings recirculations structure and subduction. *Journal of the Marine Biological Associateion of the United Kingdom*, **77**, 573–624.

Pingree, R., C. Garcia-Soto, and B. Sinha, 1999: Position and structure of the subtropical/azores front region from combined lagrangian and remote sensing (ir/altimeter/seawifs) measurements. *Journal of the Marine Biological Association of the United Kingdom*, **79**, 769–792.

Price, J. and M. Baringer, 1994: Outflows and deep water production by marginal seas. *Prog. Oceanog.*, **33**, 161–200.

Price, J., M. Baringer, R. Lueck, G. Johnson, I. Ambar, G. Parrilla, A. Cantos, M. Kennelly, and T. Sanford, 1993: Mediterranean outflow mixing dynamics. *Science*, **259**, 1277–1282.

Richardson, P. L., A. S. Bower, and W. Zenk, 2000: A census of meddies tracked by floats. *Prog. Oceanog.*, **45**, 209–250.

Rudnick, D. and J. Luyten, 1996: Intensive surveys of the azores front 1. tracers and dynamics. *J. Geophys. Res.*, **101(C1)**, 923–939.

Schlitzer, R., 2006: Ocean data view.
URL `http://odv.awi.de`

Schmitz, W. J., 1996: On the world ocean circulation. Technical report, Woods Hole Oceanographic Institution Technical Report, Woods Hole, MA.

Serra, N. and I. Ambar, 2002: Eddy generation in the mediterranean undercurrent. *Deep-Sea Res. II*, **49**, 42254243.

Smith, P., 1975: A streamtube model for bottom boundary currents in the ocean. *Deep-Sea Res.*, **22**, 853–873.

Smith, W. and D. T. Sandwell, 1997: Global seafloor topography from satellite altimetry and ship depth soundings. *Science*, **277**, 1957–1962.

Spall, M., 2000: Buoyancy-forced circulations around islands and ridges. *J. Mar. Res.*, **58(6)**, 957–982.

Spall, M. and J. Price, 1998: Mesoscale variability in denmark strait: The pv outflow hypothesis. *J. Phys. Oceanogr.*, **28**, 1598–1623.

Stanton, B., 1983: Low frequency variability in the mediterranean undercurrent. *Deep-Sea Res. II*, **30**, 743–761.

Stommel, H., 1982: Is the south pacific helium-3 plume dynamically active? *Earth Planet. Sci. Lett.*, **61**, 63–67.

Stramma, L., 1984: Geostrophic transport in the warm water sphere of the eastern subtropical north atlantic. *J. Mar. Res.*, **42**, 537–558.

Swaters, G., 1991: On the baroclinic instability of cold-core coupled density fronts on a sloping continental shelf. *J. Fluid Mech*, **224**, 361–382.

Traon, P. L. and P. D. Mey, 1994: The eddy field associated with the azores front east of the mid-atlantic ridge as observed by the geosat altimeter. *J. Geophys. Res.*, **99**, 9907–9923.

Tritton, D., 1988: *Physical Fluid Dynamics*. Oxford University Press.

Veronis, G., 1966: Wind-drive ocean circulation part ii. *Deep-Sea Res.*, **13**, 30–55.

Warren, B., 1981: *Evolution of Physical Oceanography, Scientific Surveys in Honor of Henry Stommel*. The MIT Press.

Whitehead, J., 1974: Rotating hydraulics of strait and sill flows. *Geophysical Fluid Dynamics*, **6**, 101–125.

Whitehead, J., M. Stern, G. Flierl, and B. Klinger, 1990: Experimental observations of baroclinic eddies on a sloping bottom. *J. Geophys. Res.*, **95**, 9585–9610.